Mechanically milled bulk nanocrystalline Nb(_3)Sn with improved superconducting properties in high magnetic fields

King, Matthew Benjamin

Mechanically milled bulk nanocrystalline Nb_3Sn with improved superconducting properties in high magnetic fields

Matthew Benjamin King

A thesis submitted in partial fulfilment of the requirements

for the degree of Master of Science

Department of Physics, University of Durham

2006

Mechanically milled bulk nanocrystalline Nb_3Sn with improved superconducting properties in high magnetic fields

Matthew Benjamin King

Abstract: The upper critical field of binary Nb_3Sn has been increased by mechanical milling and Hot Isostatic Pressing (HIP'ing) pre-alloyed powder to form bulk nanocrystalline samples. Extensive investigation of milling parameters allowed optimization of sample yield, purity and microstructure. X-Ray Diffraction (XRD) and Inductively Coupled Plasma Mass Spectroscopy (ICP-MS) data show that milling can produce amorphous Nb_3Sn whilst maintaining low contamination levels (< 0.4 wt. %). Nb_3Sn powder milled under an argon atmosphere using specially-manufactured niobium milling tools has been consolidated in a HIP at high pressure (2000 Bar) and a range of temperatures (450 – 850 °C). ICP-MS analysis allowed restoration of the milled Nb_3Sn stoichiometry prior to powder consolidation. In-field variable-temperature resistivity and magnetic susceptibility measurements of these disordered high-purity bulk Nb_3Sn samples are presented. The critical temperature, T_c, of Nb_3Sn is depressed by milling, but the recovery in T_c with HIP temperature coincides with a systematic reduction in microstructural disorder. The relationship between upper critical field, $B_{C2}{}^{0.5}\rho_N(0)$, and HIP temperature reaches a peak of 31.7 ± 0.4 T at 700 °C, ~6 T higher than typical values for binary Nb_3Sn. The very high normal-state resistivity (200 ± 27 μΩ cm at 20 K) and low Scherrer grain size (70 nm) imply that this increase is due to a disordered nanocrystalline microstructure. To facilitate the investigation of the properties of technological Nb_3Sn over a large range of applied strain (−1 to +0.3 %), a procedure for attaching superconducting wires to Ti-6Al-4V helical strain springs is also presented.

Declaration

I hereby declare that the work contained within this thesis is my own original work and nothing that is the result of collaboration unless otherwise stated. No part of this thesis has been submitted for a degree or other qualification at this or any other university.

M. B. King

April 2006

Table of Contents

Acknowledgements

Firstly, I would like to thank people connected with my research. My supervisor, Damian Hampshire, for setting me going on the project and for guidance and generous financial support along the way. John Evans and everyone from his group for kind access to their XRD machines as well as helpful advice. Chris Ottley and Graham Pearson for ICP measurements, Jian-Yong Xiang for resistivity measurements, as well as Ian Terry, Doug Astill and David Cardwell for access to their SQUID magnetometers. David Taylor, for patience in the face of many varied questions, in particular those computer-related. Hong-Jun Niu and Maisoon Al-Jawad for support and advice, as well as Mike Menary, Helen Armstrong and David Richards for making the group a more enjoyable place to be. There are also support staff who deserve particular mention: the lab technicians, in particular Wayne Dobby, Ian Manfren and John Summerill for good humoured willingness to help out and loan kit. Everyone in the workshop, especially Stephen Lishman, Phil Armstrong and Malcolm Robertshaw for dealing with the unusual materials I kept bringing in, and for friendly banter. Angela Healer and Claire Davies in the finance office, as well as Pauline Russell, Norma Twomey, and all the office staff. Thanks also to Mike Pennington and Pete Edwards for help and support, as well as everyone at Gilesgate school for reminding me that science can be fun. Although I was not able to give them as much attention as I would have liked, people outside physics reminded me of the important things in life: friends from hill walking, Harry Gibson, Rob Poole, Helen Vaughan, Alex Pym, Patrick Tierney, Malcolm Parks and everyone at the Waddington Street centre. Finally, the unstinting love and support of Margaret, my parents, sister and grandparents. I am also grateful for financial support from the EPSRC, County Durham Economic Partnership and the Ogden Trust.

Chapter 1

Introduction

Superconductivity was discovered in 1911 [1], but despite the exciting development of superconductivity at liquid nitrogen temperatures in the 1980s [2], the major commercial use for this amazing phenomenon remains the production of superconducting electromagnets. In this industry, superconductors offer huge technological advantages over conventional resistive magnets: no need for continual electrical power input (which would be prohibitive for large magnets), extremely stable fields (critical for MRI hospital scanners) and smaller size (important in transport applications). The requirement for cryogenic temperatures may make long-distance power transmission too expensive, but this is manageable for a localised magnet.

To be used in magnets, wires must continue to be superconducting when subject to high magnetic fields, making Type-II superconductors in the mixed state the only viable option. As will be outlined in more detail in this report, the maximum field in which a superconductor can carry a transport current depends on the coherence length, and the maximum transport current depends on how well crystalline defects can 'pin' fluxons in place. Low level doping can improve these properties slightly, but higher levels of doping depress superconductivity. Nanocrystalline superconductors offer improvements in both critical field and critical current by reducing the superconducting coherence length and by providing a high density of strong fluxon 'pinning' sites at grain boundaries. Work on the chevrel-phase superconductor $PbMo_6S_8$ [3] showed that ball milling [4] followed by HIP'ing can be used to produce a nanocrystalline material with

the expected increases in the critical properties. Nb_3Sn is a technologically important superconductor in widespread use, and the main aim of the work in this thesis was the adaptation to Nb_3Sn of the techniques used to improve $PbMo_6S_8$. An important aspect of this objective was the optimisation of the ball milling process for Nb_3Sn, as very little data on this existed previously. Work will also be presented on the effect of HIP parameters on the superconducting properties of the resulting bulk nanocrystalline samples.

As well as the microstructure of Nb_3Sn already mentioned, strain can also have a significant effect on the superconducting properties. In particular, wires used for superconducting magnets are subject to considerable strains, but historically little research has been done to accurately characterise this effect. In recent years, the need to understand the exact relationship between strain and critical current has been brought into sharp focus by the multi billon dollar international fusion project, ITER, which will use a superconducting tokomak to confine the very-high-temperature plasma needed for fusion. Much work has been done in Durham on characterising strain effects by electroplating a superconducting wire to the outside of a titanium spring so that strain can be applied evenly along the wire's length. In addition to the fabrication work mentioned, this thesis also describes the development from a patented process of a safe electroplating method using potentially hazardous hydrofluoric acid, with the aim of bringing this important technique in-house.

The thesis is structured as follows: elementary superconductivity will be reviewed in Chapter 2, followed by a discussion of experimental techniques in Chapter 3. The next four chapters contain the main experimental results, analysis and discussion. The work on electroplating is included in Chapter 4, with optimisation of the ball milling process in Chapter 5. Chapter 6 describes the ball milled samples which were subsequently consolidated by HIP'ing, and magnetic measurements of the superconducting properties

of these bulk nanocrystalline samples will be included in Chapter 7. Conclusions from the four experimental chapters are then presented together in Chapter 8, with future work discussed in Chapter 9.

Chapter 2

Elementary superconductivity

2.1 Introduction

A review of important aspects of superconductivity is given in this chapter. The phenomenological approach of Ginzburg-Landau (G-L) theory gives useful insights, particularly into the significance of the superconducting length scales, and so is reviewed in Section 2.2. Section 2.3 includes the Bean model description of how magnetic hysteresis arises in the mixed state of real superconductors, and how this relates to the technologically important critical current density, J_c. The chapter concludes in Section 2.4 with a brief summary of the microscopic BCS theory from which relationships useful for analysis can be derived.

2.2 Ginzburg-Landau

In 1950, Ginzburg and Landau proposed a phenomenological theory [5] that does not try to explain the underlying microscopic origin of superconductivity, but instead describes the superconducting state using thermodynamics. The summary of this well-established theory given below has drawn on a number of sources [6-13].

G-L theory assumes that the superconducting state can be described by a complex order parameter, Ψ, where $\Psi = 0$ for $T > T_c$ As $|\Psi|^2$ can be set equal to the density of

superelectrons (electrons in the condensed superconducting state), Ψ can also be thought of as a macroscopic wavefunction of the electron "superfluid".

2.2.1 Bulk normal to superconducting (Meissner state) transition

When Ψ does not vary spatially (e.g. deep within a homogenous material under steady state conditions), a simple G-L description can be used to describe the normal to superconducting (Meissner state) phase transition. G-L theory assumes that for $T \approx T_c$, Ψ is small and so, as the superconducting to normal phase change is second order with no external applied field, the Helmholtz free energy density can be expanded as a polynomial function (Taylor expansion) of Ψ. The Helmholtz free energy density, f_s, is a real function, so only powers of $|\Psi|^2$ appear. The superconducting order is therefore assumed to be a small correction to the normal state Helmholtz free energy density, f_n.:

$$f_s = f_n + \alpha(T)|\Psi|^2 + \frac{1}{2}\beta(T)|\Psi|^4 + \ldots \tag{2.2.1}$$

where α and β are temperature dependent G-L parameters. G-L then assumes that another Taylor expansion can be used for $\alpha(T)$ and $\beta(T)$. Given that $\alpha(T)$ has to change sign at T_c (to ensure a transition), and that the simplest solution would have $\beta(T)$ remaining positive (to ensure minima), G-L also assumes that only the first terms are important:

$$\begin{aligned} \alpha(T) &= C(T - T_C) \\ \beta(T) &= \beta \end{aligned} \tag{2.2.2}$$

where C is a constant. Hereafter, the temperature dependence of $\alpha(T)$ will not be stated explicitly, and α will be used instead. Substituting Eq. (2.2.2) into Eq. (2.2.1) and

differentiating with respect to Ψ leads to a minimum in f for $T > T_c$ at $\Psi = 0$, and minima for $T < T_c$ of energy:

$$f_s(T,0) - f_n(T,0) = -\frac{C^2(T-T_C)^2}{2\beta} = -\frac{\alpha^2}{2\beta} \tag{2.2.3}$$

It can be shown that the Gibbs free energy, G, for a material in a magnetic field is given by:

$$G(T,\underline{\mathbf{H}}) = U - TS - \mu_0 V \underline{\mathbf{H}}.\underline{\mathbf{M}} \tag{2.2.4}$$

where U is the internal energy, T is the temperature, S is the entropy, μ_0 is the permeability of free space, V is the sample volume, $\underline{\mathbf{H}}$ is the applied magnetic field and $\underline{\mathbf{M}}$ is the magnetisation. On applying a magnetic field of magnitude H_c, the change in free energy for a normal material and a Type I superconductor (when the Meissner effect ensures that $\underline{\mathbf{M}} = -\underline{\mathbf{H}}$) can be found by integrating the differential form of Eq. (2.2.4):

$$G_s(T,H_c) - G_s(T,0) = -\mu_0 V \int_0^{H_c} \underline{\mathbf{M}}.d\underline{\mathbf{H}} = \frac{1}{2}\mu_0 V H_c^{\,2} \tag{2.2.5}$$

$$G_n(T,H_c) - G_n(T,0) = -\mu_0 V \int_0^{H_c} \underline{\mathbf{M}}.d\underline{\mathbf{H}} \approx 0 \tag{2.2.6}$$

As $G_s(T, H_c) = G_n(T, H_c)$ at the transition point, then:

$$G_s(T,0) - G_n(T,0) = -\mu_0 V \int_0^{H_c} \underline{\mathbf{M}}.d\underline{\mathbf{H}} = -\frac{1}{2}\mu_0 V H_c^{\,2} \tag{2.2.7}$$

As the expression relating the Helmholtz and Gibbs free energies is:

$$G_s(T,\underline{\mathbf{H}}) = F(T,\underline{\mathbf{H}}) + \mu_0 V \underline{\mathbf{H}}.\underline{\mathbf{M}} \tag{2.2.8}$$

and at zero applied field, $\underline{\mathbf{H}} = \underline{\mathbf{M}} = 0$, Eq. (2.2.7) can be re-written in terms of a Helmholtz free energy density, $f = F/V$:

$$f_s(T,0) - f_n(T,0) = -\frac{1}{2}\mu_0 H_c{}^2 \tag{2.2.9}$$

$\frac{1}{2}\mu_0 H_c{}^2$ is the condensation energy density (free energy difference per unit volume) between the normal and Meissner states at a particular temperature T, whose corresponding thermodynamic critical field is $H_c(T)$.

Comparing Eq.s (2.2.3) and (2.2.9) yields an expression for $H_c(T)$ which holds near T_c:

$$H_c = \frac{\alpha}{(\mu_0\beta)^{1/2}} \tag{2.2.10}$$

2.2.2 Coherence length within G-L theory

G-L Theory can also be used to describe regions where the superconducting state varies (spatially), for example at surfaces and other boundaries. Ψ is now taken to be a function of position, $\underline{r}$, and there is an extra contribution to the Helmholtz free energy due to spatial variations in Ψ :

$$f_s = f_n + \frac{\hbar^2}{2m^*}\left|\nabla\Psi(\underline{\mathbf{r}})\right|^2 + \alpha\left|\Psi(\underline{\mathbf{r}})\right|^2 + \frac{1}{2}\beta\left|\Psi(\underline{\mathbf{r}})\right|^4 + \ldots \tag{2.2.11}$$

where m^* is the effective mass. Integrating this free energy density over the superconductor, and minimising the resulting total free energy leads to the expression:

$$-\frac{\hbar^2}{2m^*}\nabla^2\Psi(\underline{\mathbf{r}}) + \left(\alpha + \beta\left|\Psi(\underline{\mathbf{r}})\right|^2\right)\Psi(\underline{\mathbf{r}}) = 0 \tag{2.2.12}$$

This is known as the **First G–L Equation**, and can be solved at an S-N (Superconducting-Normal) boundary (perpendicular to the x direction, with $x > 0$ for S). If the substitution $\sqrt{\frac{-\hbar^2}{2m^*\alpha}} = \xi(T)$ is made, the expression yields:

$$\Psi(x) = \Psi_0 \tanh\left(\frac{x}{\sqrt{2}\xi(T)}\right) \tag{2.2.13}$$

This equation shows that the coherence length, $\xi(T)$, is a characteristic distance over which the order parameter can change. When compared to microscopic Bardeen-Cooper-Schrieffer (BCS) theory, this length is found to be the size of a superconducting Cooper pair. The temperature dependence of the coherence length, $\xi(T)$, comes from the appearance of the G-L parameter α in the substitution, and since $\alpha(T) \propto (T - T_c)$, it is clear that:

$$\xi \propto (1-t)^{-1/2} \tag{2.2.14}$$

for $T \approx T_c$, where t is the reduced temperature $t = T/T_c$.

2.2.3 Penetration depth within G-L theory

G-L Theory can be used to describe the effect of applying a magnetic field to a superconductor. In the presence of a magnetic field, a more general expression of the Gibbs free energy is required:

$$g(\underline{\mathbf{r}}) = f_n + \alpha|\Psi(\underline{\mathbf{r}})|^2 + \frac{1}{2}\beta|\Psi(\underline{\mathbf{r}})|^4 + \frac{1}{2m^*}\left|(-i\hbar\nabla - 2e\underline{\mathbf{A}})\Psi(\underline{\mathbf{r}})\right|^2 + \frac{\underline{\mathbf{B}}^2}{2\mu_0} + \frac{1}{2}\mu_0\underline{\mathbf{H}}_a{}^2 - \underline{\mathbf{H}}_a.\underline{\mathbf{B}} \tag{2.2.15}$$

This can be minimised w.r.t. the vector field, $\underline{\mathbf{A}}$, to yield the **Second G-L Equation** for the supercurrent density, $\underline{\mathbf{J}}_s$:

$$\underline{\mathbf{J}}_s = \frac{-ie\hbar}{m^*}\left(\Psi^*\nabla\Psi - \Psi\nabla\Psi^*\right) - \frac{4e^2}{m^*}\left|\Psi\right|^2\underline{\mathbf{A}} \tag{2.2.16}$$

Far enough into the bulk of a superconductor (i.e. many coherence lengths), it can be assumed that $\Psi = \Psi_0$ (i.e. the superconducting order parameter has reached its steady maximum value), and so Eq. (2.2.12) becomes:

$$\left(\alpha + \beta\left|\Psi(\underline{\mathbf{r}})\right|^2\right)\Psi(\underline{\mathbf{r}}) = 0 \tag{2.2.17}$$

which has a (superconducting) solution of:

$$-\frac{\alpha}{\beta} = \left|\Psi(\underline{\mathbf{r}})\right|^2 \tag{2.2.18}$$

Applying $\Psi = \Psi_0$ changes Eq. (2.2.16) into:

$$\underline{\mathbf{J}}_s = -\frac{4e^2}{m^*}\left|\Psi\right|^2\underline{\mathbf{A}} \tag{2.2.19}$$

Substituting Eq. (2.2.18) into Eq. (2.2.19) gives:

$$\underline{\mathbf{J}}_s = \frac{4e^2\alpha}{m^*\beta}\underline{\mathbf{A}} \tag{2.2.20}$$

Taking the curl of both sides of (2.2.20) yields:

$$\nabla\times\underline{\mathbf{A}} = \underline{\mathbf{B}} = \frac{m^*\beta}{4e^2\alpha}\nabla\times\underline{\mathbf{J}}_s \tag{2.2.21}$$

Substituting $\nabla\times\underline{\mathbf{B}}/\mu_o$ for $\underline{\mathbf{J}}_s$, and using the identity $\nabla\times(\nabla\times\underline{\mathbf{B}})=\nabla(\nabla\cdot\underline{\mathbf{B}})-\nabla^2\underline{\mathbf{B}}$ results in:

$$\nabla^2\underline{\mathbf{B}}=\left(\frac{-4e^2\mu_o\alpha}{m^*\beta}\right)\underline{\mathbf{B}} \tag{2.2.22}$$

If the substitution $\sqrt{-m^*\beta/4e^2\mu_0\alpha}=\lambda$ is made, this can be solved in 1 dimension to give:

$$\underline{\mathbf{B}}(x)=\underline{\mathbf{B}}_0(x)\exp(-x/\lambda) \tag{2.2.23}$$

The penetration depth, λ, is therefore a characteristic distance over which a magnetic field decays, assuming that $\Psi=\Psi_0$ and $T\approx T_c$. In a similar way to $\xi(T)$, the temperature dependence of the magnetic field penetration depth, $\lambda(T)$, comes from the appearance of the G-L parameter $\alpha(T)$ in the substitution. Introducing the reduced temperature, $t=T/T_c$, means that for $T\approx T_c$:

$$\lambda\propto(1-t)^{-1/2} \tag{2.2.24}$$

2.2.4 Ginzburg-Landau parameter, κ

Note that λ and ξ have the same temperature dependence in G-L theory, and so their ratio, λ/ξ, is temperature independent for $T\approx T_c$. Therefore, if λ and ξ are written in terms of their original Ginzburg-Landau parameters, $\lambda(T)=\sqrt{-m^*\beta/4e^2\mu_0\alpha}$ and $\xi(T)=\sqrt{-\hbar^2/2m^*\alpha}$, the ratio λ/ξ becomes:

$$\kappa=\frac{\lambda}{\xi}=\sqrt{\frac{m^{*2}\beta}{2\hbar^2e^2\mu_0}} \tag{2.2.25}$$

where κ is the temperature-independent (near T_c), dimensionless, Ginzburg-Landau parameter.

Analysis of an SN region using G-L theory reveals a balance of positive and negative contributions to the free energy of the boundary surface, which determines whether a superconductor is Type I (homogeneously all normal or all superconducting) or Type II (mixed state allowed). There is a positive contribution to the surface energy from the region in which the superconductivity is recovering from the normal boundary (i.e. the coherence length, ξ, over which Ψ increases to Ψ_0), which is clearly less energetically favourable than if the whole region was totally superconducting with $\Psi = \Psi_0$. However, there is also a negative energy contribution from the region in which the field has been allowed to penetrate, as the "pressure" of the externally applied field has been relieved. The size of this region is determined by the penetration depth, λ. Detailed calculation (see de Gennes [14]) shows that the mixed state becomes energetically favourable when $\kappa > 1/\sqrt{2}$, so that for:

Type I Superconductors:	$\kappa \leq 1/\sqrt{2}$
Type II Superconductors:	$\kappa > 1/\sqrt{2}$

G-L theory can also be used to derive experimentally useful expressions for the upper critical field, B_{C2}, which is the field at which Type-II superconductors undergo the mixed state-normal phase transition:

$$B_{C2}(T) = \sqrt{2}\kappa(T_C)B_C(T)\Big|_{T_C} \tag{2.2.26}$$

$$B_{C2}(T) = \frac{\Phi_0}{2\pi\xi(T)^2}\Big|_{T_C} \tag{2.2.27}$$

where Φ is the quantum of flux = 2.07×10^{-15} T m^2

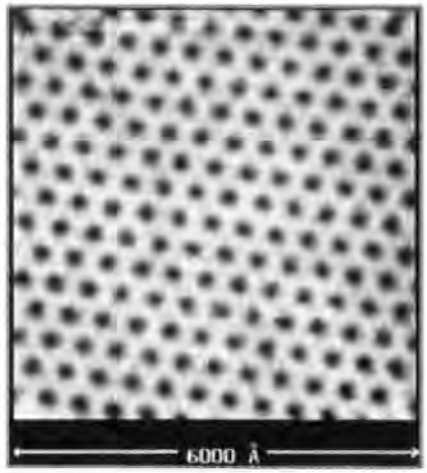

Figure 2.1 STM image of fluxon lattice, from Hess et al [15]

2.2.5 The mixed state in Type-II superconductors

In Type-II superconductors, where $\kappa > 1/\sqrt{2}$, it is energetically favourable between B_{C1} and B_{C2} to have normal (allowing magnetic flux through) and superconducting (shielding out magnetic flux) regions co-existing within the same sample. The superconducting boundary regions shield the bulk of the superconducting region from the magnetic flux in the normal regions. Because the complex macroscopic wavefunction Ψ is single valued at any point, the phase change of Ψ around any closed loop must be equal to $2n\pi$, and so the amount of flux in the normal region that can be shielded out is quantised into "fluxons" of value $\Phi = h/2e$. Work by Abrikosov [16] and subsequently Kleiner et al. [17] calculated that in a homogenous Type-II superconductor, fluxons would preferentially arrange themselves in a triangular lattice due to fluxon-fluxon repulsion (resulting from the interaction between the magnetic field of one fluxon and the shielding current of a second), see Figure 2.1.

By solving the full G-L equations using a perturbative method, Abrikosov determined the $M(H,\kappa)$ relationship in the reversible region near H_{C2}:

$$M = \frac{-(H_{C2} - H)}{\beta_A (2\kappa^2 - 1)} \tag{2.2.28}$$

where H is the applied field, κ is the G-L parameter for the material, and $\beta_A = 1.16$ for the ground-state triangular flux line lattice.

2.2.6 Flux pinning in superconductors

A real (inhomogeneous) superconductor contains regions of weaker superconductivity (e.g. centred on impurities or lattice defects such as grain boundaries) which can be driven into the normal state with a lower energy penalty than for the bulk of the material. This means that these regions will be preferentially occupied by fluxons, and because fluxon movement away from the site has an associated energy cost, the fluxon is attracted or "pinned" to the site. When a transport current is flowing through a Type-II superconductor in the mixed state, the fluxons will experience a Lorentz force. Fluxon movement is dissipative, and so for lossless conduction, the fluxons must held in place by a retaining force equal to the Lorentz force. In most cases, the only significant retaining force is the pinning force, F_p, and so this is given by:

$$\underline{F}_p = \underline{J} \times \underline{B} \tag{2.2.29}$$

2.2.7 Critical current density

Microscopic theory implies the existence of a maximum theoretical current density in the limit where the kinetic energy (as determined by the momentum of the macroscopic wave-function) of each Cooper pair (paired electrons making a composite boson) equals the de-pairing energy [11]. However, in practice, the critical current, J_c, of

the technologically useful Type-II superconductors is determined by the onset of dissipation resulting from Lorentz-force-induced flux movement, and so the distribution, density and type of flux-pinning sites becomes crucial.

2.3 Bean model

Bean's original paper [18] describes a critical state model that can be used to analyse experimental data to get useful numbers for superconducting parameters for materials in the mixed state. As discussed above (Sections 2.2.4 and 2.2.5), when a magnetic field larger than B_{C1} is applied to a type-II superconductor, it is energetically favourable to allow some magnetic flux to penetrate the sample in the form of (quantised) fluxons. If there are no pinning sites (e.g. in a perfect single crystal), the fluxons that have penetrated are able to move freely, and so the fluxon-fluxon repulsions mean that they arrange themselves uniformly within the bulk of the sample. However, when fluxons penetrate a Type-II superconductor with pinning sites, it is energetically favourable for the fluxons to coincide with these regions of weaker superconductivity. The first fluxons penetrating a sample will therefore be pinned at sites near the surface. Subsequent fluxons entering the sample will exert a repulsive force on the first fluxons, directed into the sample. However, a pinned fluxon a distance d below the surface will remain pinned as long as the difference in fluxon concentration between $d+\delta d$ and $d-\delta d$ is such that the net repulsive force from the fluxons around it is less than its pinning force. Therefore, unlike perfect single crystals, applying a magnetic field to a sample with pinning sites can result in stable spatial variations in fluxon density (i.e. a field gradient).

The critical field gradient at which the pinning force balances the net repulsive force due to the fluxon concentration gradient is most easily understood with reference to Maxwell's equation $\nabla \times \underline{B} = \mu_0 \underline{J}$, which means that this magnetic field gradient

corresponds to an effective screening current (the sum of the circulating currents from each fluxon vortex). As discussed in Section 2.2.6, the maximum value that this effective screening current can take is related to the pinning force by $\underline{F}_p = \underline{J}_c \times \underline{B}$. Therefore, the maximum static field gradient that a superconductor can maintain is directly related to the critical current of the superconductor, J_c.

The Bean model postulates that fluxons in a sample in the mixed state arrange themselves in such a way that the field gradient at any point in the sample is either zero or its maximum possible value. This means that the effective screening current in a particular region of a Type-II superconductor in the mixed state can only take the values J_c (if the region is in the "Critical State"), or 0 (otherwise).

If a magnetic field is applied to a previously fluxon-free superconducting sample, the field gradient will decrease linearly with depth to a minimum and then increase linearly out to the other side of the sample, although the exact details will depend on the sample's geometry. Therefore, if the magnetic moment of a sample due to its superconductivity ($M_{s/c}$) is measured in a particular field, the sample's geometry is known and the applied field is large enough that there is no zero-gradient region in the centre, Bean's model can be used to estimate its critical current using the formula:

$$M_{s/c} = \frac{1}{2}\gamma_{sf} J_c \tag{2.3.1}$$

where γ_{sf} is a shape factor which takes into account the geometry of the sample

2.3.1 Magnetisation hysteresis

As discussed above, in superconductors with pinning sites, stable field gradients can exist, up to a certain maximum value determined by the pinning force. This means that

unlike perfect single crystals, different field profiles (with different magnetic moments) can be stable in a particular applied field. This leads to magnetic hysteresis.

If a (slowly) increasing magnetic field is applied to a flux-free Type-II superconducting sample (at constant temperature T, $T < T_c$), the sample will exhibit perfect diamagnetism up to B_{C1} (i.e. all flux is excluded). Then flux will penetrate such that there is a field gradient near the surface, decreasing to zero field in a central region. However, the magnetic field range that these two regimes correspond to is extremely small in comparison to B_{C2}. At higher fields, the usual situation is that the magnetic field decreases linearly from the surfaces of the sample to a point minimum at the centre of the sample, according to the Bean model.

It should be emphasised that the field gradient depends on the value of $J_c(B,T)$, which in turn depends on $F_p(B,T)$. F_p (and so J_c) decrease to zero as B approaches $B_{C2}(T)$, as the pinning force depends on an energy difference between the superconducting and normal regions which is zero when the whole sample is normal. At B_{C2}, the sample becomes normal. Here, the sample's moment has no contribution from superconductivity, and so the moment is determined by the (usually) weak normal-state susceptibility. Hence the magnetic field inside the sample is essentially the same as the applied field. If the applied field is then reduced below B_{C2}, the sample becomes (weakly) superconducting, and the fluxons become weakly pinned, preventing the fluxon concentration (field) from decreasing to the applied field value.

Therefore, according to the Bean model, as the field is decreased, the magnetisation of the sample due to its superconductivity should be equal and opposite to its value when the field was increasing. In reality there are other contributions to the sample's moment, but as long as these contributions are reversible, then they can be excluded by calculating the difference in total magnetic moment induced (at a particular applied field) when increasing the field compared to decreasing the applied field, i.e. $M_+ = M_{s/c} + M_n$,

$M_- = -M_{s/c} + M_n$. A value for J_c for a particular applied field can then be found from the maximum difference in magnetisation using the formula [6, 8, 19]:

$$\Delta M = M_+ - M_- = \gamma_{sf} J_c \tag{2.3.2}$$

where M_+ is the positive magnetisation response, M_- is the negative magnetisation response and γ_{sf} is the shape factor, which is based on Bean model calculations of the macroscopic effect of the different microscopic values of magnetisation within a sample of a particular shape. A demagnetisation factor must also be taken into account when determining the magnetic response characteristic of the sample from measurements.

2.4 BCS theory

BCS theory provides a microscopic description of superconductivity, but will not be covered in detail in this report. However, certain key equations are needed for the analysis of results: Orlando et al. [20] derived an equation which can be written in the form:

$$B_{C2}(0) = \frac{R(\infty)}{R(\lambda_{tr})}\left(8.3\times10^{34}\left(\frac{\gamma T_C}{S}\right)^2 + 3.1\times10^3 \gamma T_C \rho_N\right) \tag{2.4.1}$$

where $R(\infty)/R(\lambda_{tr})$ is a strong coupling correction close to unity, γ is the Sommerfeld constant (related to the electronic density of states), S is the Fermi surface area and ρ_N is the normal state resistivity. It can be seen that increases in $B_{C2}(0)$ are possible if ρ_N can be increased without affecting T_c and the density of states too badly. Increases in resistivity result in a reduction of the electron mean free path, with a consequent reduction in the

coherence length, ξ. Hence κ increases and allows superconductivity in the mixed state to exist at higher fields.

Doping can be used to introduce disorder and can thereby increase ρ_N, but also seriously affects the density of states, so only small increases in $B_{C2}(0)$ can be produced with low levels of doping. Disorder can be introduced in other ways (e.g. lattice defects and grain boundaries), and increases in $B_{C2}(0)$ have been successfully produced in Nb_3Sn in thin film form by preparing non-equilibrium layers [21]. As will be outlined in Section 3.2, ball milling is another means of introducing disorder, and in 2003, the Superconductivity Group in Durham used milling to prepare disordered nanocrystalline $PbMo_6S_8$ (PMS) with a very high $B_{C2}(0)$ value [3]. The introduction of disorder also has the result of providing strong fluxon pinning sites, which can have a positive effect on J_c as well, although this is not normally a limiting factor in magnet technology.

Two other useful expressions can be derived from microscopic theory in the BCS limit [3]:

$$\left(\frac{\partial B_C(T)}{\partial T}\right)\Bigg|_{T_c} = -1.20\mu_0^{1/2}\gamma^{1/2} \tag{2.4.2}$$

$$B_C(0) = 0.69\mu_0^{1/2}\gamma^{1/2}T_C \tag{2.4.3}$$

Wertmaner-Helfand-Hohenberg theory [22] provides an expression which can be useful for approximating $B_{C2}(0)$ from experimental data:

$$B_{C2}(0) = -0.69T_C\left.\frac{\partial B_{C2}}{\partial T}\right|_{T_c} \tag{2.4.4}$$

Chapter 3

Experimental techniques

3.1 Introduction

This chapter provides a description of some key experimental techniques used in this work. Ball milling to drive microstructural change is covered in the next section. X-Ray Diffraction (XRD) allowed microstructural change to be measured, and XRD techniques and analysis are introduced in Section 3.3. The chapter concludes in Section 3.4 with the basic principles of ICP-MS, used for compositional analysis, together with results of consistency tests.

3.2 Ball milling

3.2.1 Mechanism and effects of ball milling

Ball milling is the general name given to materials processing techniques developed in the late 1960s [4] in which structural change is induced in powder samples by subjecting particles (~10 μm) to a large number of impacts by relatively massive (~2 cm diameter) milling balls. This is achieved by partially filling a vial with milling balls and sample powder. The vial is sealed and then continuously accelerated so that milling balls fly across the vial at high speed, resulting in chaotic impacts between the milling balls, sample powder and vial walls. Ball milling is roughly sub-divided into Mechanical

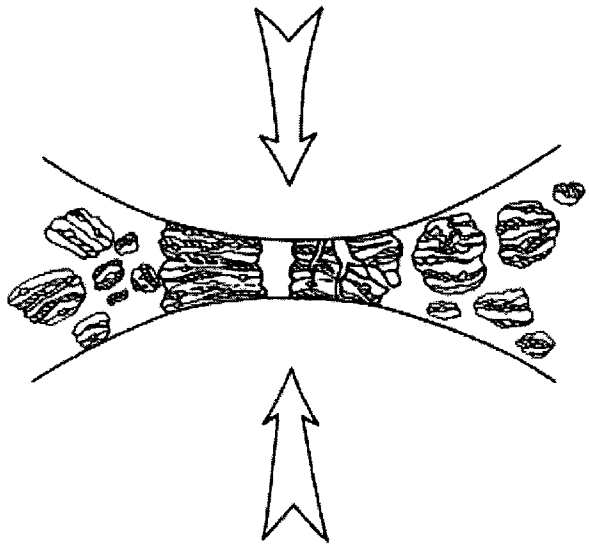

Figure 3.2 Collision event during ball milling causing welding and fracture

Alloying (MA) and Mechanical Milling (MM), depending on whether the primary purpose is chemical or microstructural change. The MA and MM mechanisms are outlined in Sections 3.2.1.1 and 3.2.1.2 respectively, with details of the commercial milling machines used in this work in Section 3.2.2.

3.2.1.1 Mechanical Alloying

When ball milling is used to form alloys from elemental powders, synthesise complex alloys from simpler compounds, induce chemical reactions and disperse gas within a solid, it is referred to as Mechanical Alloying (MA). In the most general case, powder particles are subject to plastic deformation when trapped in collisions with milling balls, which cold welds particles together as well as causing microstructural disorder and particle fracture. Reactions with other solids, liquids or gases in the vial then take place at the fresh atomic surfaces exposed during fracture, allowing the formation of novel alloys or homogeneous gas dispersions which would otherwise be difficult to synthesize. The most common example of MA is the production of alloys from elemental powders. The accepted mechanism in the literature for this is that cold welding and

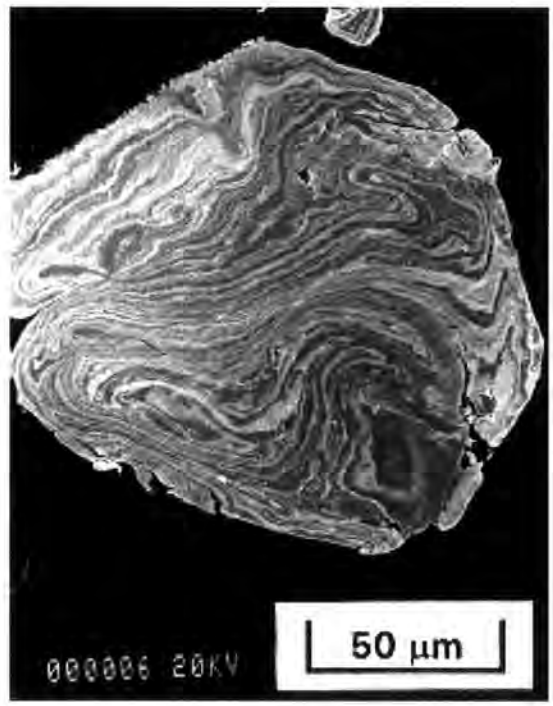

Figure 3.3 Lamellar structure seen part way through Mechanical Alloying.

fracture (Figure 3.2) initially result in lamellar structures with alternate layers of elements (Figure 3.3). As cold welding and fracture continues, these elemental lamellae become so thin that it becomes energetically possible for atoms to diffuse out of the disordered elemental layers to form an alloy in the boundary regions. As milling continues, the cycle of fracture and alloy formation after cold welding can result in a single-phase sample. As MA was not used in this work, this cursory explanation is sufficient, as there are a number of review articles [23-25] which provide a fuller description.

3.2.1.2 Mechanical Milling

The work in this report focuses on MM, the use of ball milling as a means of changing the microstructure of a pre-existing phase (in this case Nb_3Sn). A fuller discussion of the microstructural effects of MM is included in Section 5.3.4, but a basic description is included here. Collisions during MM result in particle fracture, cold work and some cold welding. This can result in a reduction in particle size to sub-micron

Table 3.1 Summary of millers used in this work

Miller	Type	Milling action lengths			Inner vial dimensions		
		Milling action	Amplitude (mm)	Frequency (Hz)	Diameter (mm)	Length (mm)	Milling media
Fritsch P6	planetary	rotation	~60 [a]	2-10 [b]	~75	~70	agate, copper [f], niobium [f], titanium [f]
Retsch MM301	shaker	linear	~30	3-30 [c]	~32	~55	steel, tungsten carbide
SPEX 8000D	shaker	figure of eight (∞)	~60 x ~25 [d]	15	43-50 [e]	45-65 [e]	copper [f], steel, tungsten carbide

[a] Distance from pot centre to axis of disk rotation
[b] Frequency of rotation to revolution speed ratio set to -0.8 (i.e. pot rotates in opposite sense to revolution of disk pot is mounted on)
[c] Manufacturer recommended a maximum frequency of 25 Hz be used
[d] Linear motion x lateral movement
[e] Exact dimensions vary depending on milling medium
[f] Milling pot and balls manufactured in departmental workshop, Durham

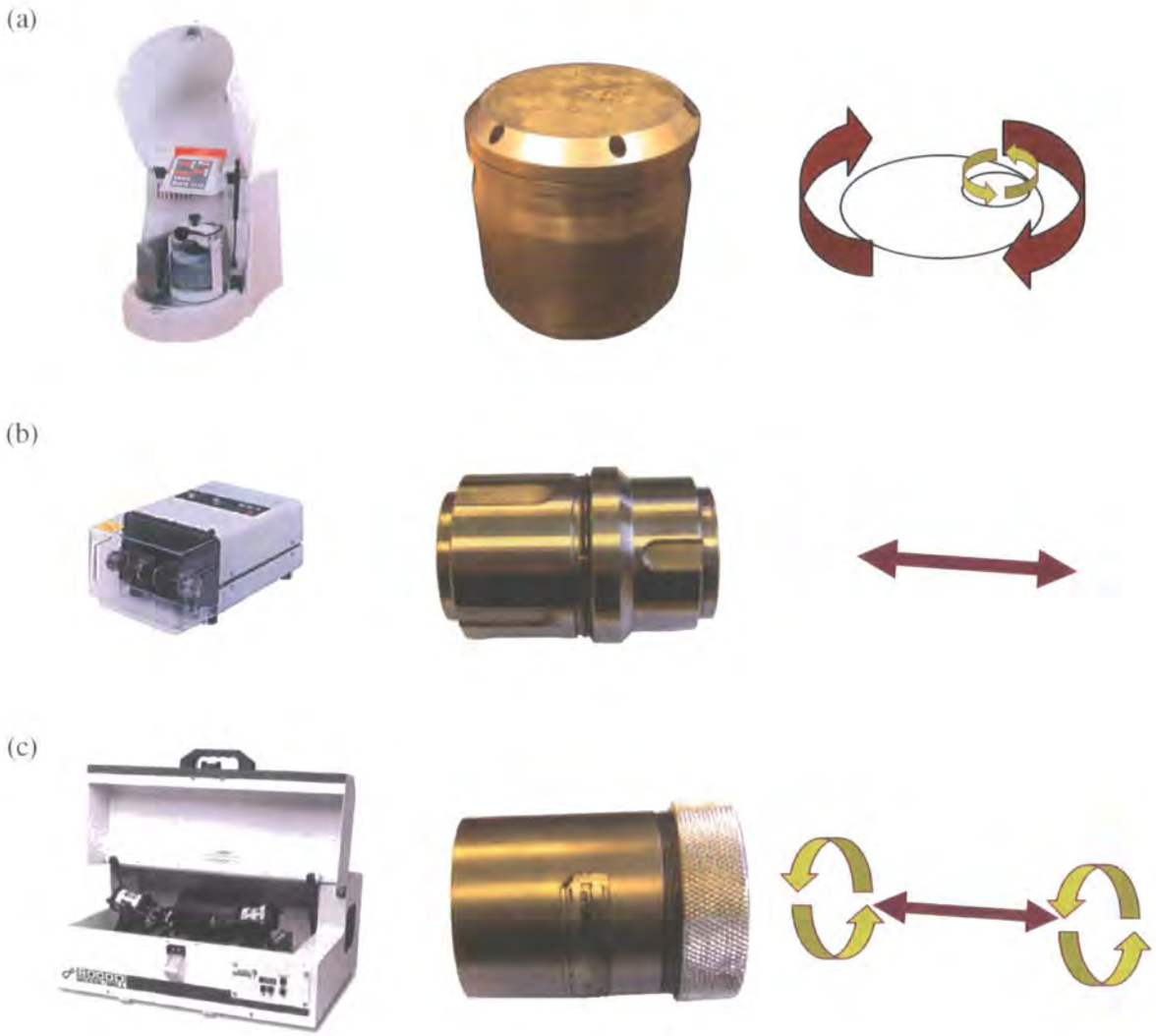

Figure 3.4 Photographs, milling pots and schematic representation of the milling pot motion for the: (a) Fritsch P6, (b) Retsch MM301 and (c) SPEX 8000D

levels, reduction of grain (crystallite) size, and the introduction of other crystal defects such as dislocations, vacancies and anti-site disorder. The disorder energy associated with such defects can be considerable [24], and so MM can drive synthesis of a variety of metastable states, including nanocrystalline, amorphous and de-mixed phases.

Although MA has been used for Nb_3Sn production in Durham [26] and elsewhere [27-29], it had a number of disadvantages over MM for this work. The aim of this work was to produce Nb_3Sn with a disordered microstructure, and it has been seen previously that although MA can be used to form amorphous Nb_3Sn, the time taken is much longer than that needed to produce amorphous Nb_3Sn by MM. As greater milling time generally corresponds to increased contamination, this is undesirable. MM also has the advantage of producing a series of samples with continuous increase in disorder. The effect of disorder can therefore be isolated by direct comparison of milled samples with both the unmilled starting material, and with annealed milled powder. In contrast, MA occurs by a different mechanism, meaning that when Nb_3Sn forms, its level of disorder is unlikely be altered by further milling, so there is less choice of microstructure. In addition, niobium and tin have different propensities to stick to the sides of the pot, resulting in changes in stoichiometry and inhomogeneity. MM has therefore been used exclusively in this work.

3.2.2 Ball millers used

Because ball milling has allowed the formation of novel materials, a variety of ball milling machines are available commercially. Most of the work in this thesis was carried out using a Fritsch Pulverisette 6 planetary miller. Results from successful trials arranged on SPEX 8000D and Retsch MM301 are also presented, as well as the use of a Hosokawa 100AS Spiral Jet mill (courtesy of Leeds University). Table 3.1 includes technical details of the main three millers used. The Fritsch Pulverisette 6 (P6) is a planetary ball miller with one vial station, which means that the vial is set on the edge of

a horizontal revolving disk, and the pot itself rotates about its own axis, in the opposite direction (Figure 3.4a). The Retsch MM301 has a simple linear action (Figure 3.4b), and two milling pots are clamped in place and shaken concurrently. The SPEX 8000D miller also has two milling stations with vials slightly bigger than the Retsch's, and has a more complex rotating figure-of-eight motion (Figure 3.4c), with a linear component along the length of the milling pot, and a lateral see-saw rotation. The jet miller accelerates powder particles using high pressure gas, and grinding is achieved by inter-particle collisions.

3.2.3 Milling parameters

The most important characteristics of the powder produced by milling are yield, contamination and microstructure. Yield is simply the mass of sample obtainable after milling as a proportion of the sample mass added initially (Section 5.3.2). Contamination from wear of milling media is expressed in this thesis as a percentage by weight of the total sample mass, as determined by ICP-MS (Section 3.4). Microstructural change is the object of milling, and has been measured using XRD (Section 3.3). The key milling parameters which have been investigated in this thesis are: the miller used (Fritsch P6, Retsch MM301, SPEX 8000D and the Hosokawa 100AS jet miller), the material used to make the milling pot and balls (milling media include 99.95 wt. % niobium, agate, 99.95 wt. % copper, steel, 99.8 wt. % titanium, and tungsten carbide), milling time (15 minutes up to 240 hours), milling speed (this varies from miller to miller), the ratio of the ball weight to the powder weight (BPRs used vary from ~3 to ~75), ball size (~6 mm to ~30 mm diameter), temperature (using liquid nitrogen), and the effect of scraping the sides of the pot regularly (using a niobium rod). Where possible, these factors have been investigated in a systematic way, but restrictions on time and available materials have not always allowed this. Results showing the effect of varying milling parameters, together with information from the literature, are included in Section 5.3.

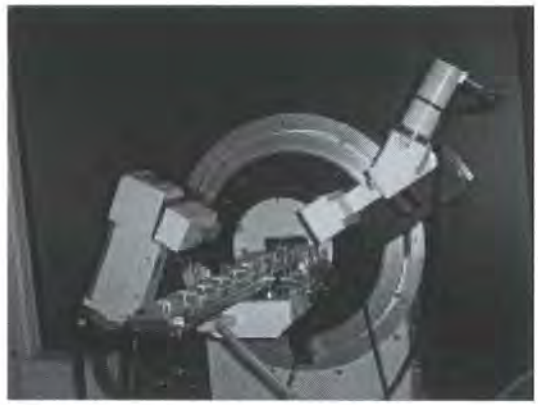

Figure 3.5 Bruker D8 used for the XRD measurements (access courtesy of J S O Evans)

3.3 X-Ray Diffraction

X-Ray Diffraction (XRD) is a useful source of information about the crystal structures present in a sample. A Bruker D8 diffractomer was used for this work (Figure 3.5). X-rays are shone on the sample from a Cu Kα source (λ = 1.5418 Å, E = 8.04 keV), producing a series of diffraction peaks at different angles, which are characteristic of the particular (crystalline) chemical phase. Fine powders (particle size ~1 μm) were produced in this work, making powder XRD the most suitable technique to use. Powders are pressed flat on to a sample slide, preferably so that crystallites within the particles are randomly orientated. The X-ray beam typically shines on an area of sample about 6 mm across, the sample slide rotates (in the plane of the flat surface as the measurement is taken), and the X-ray probes ~10 μm depth. This means that millions of particles could contribute, and the resulting data are a sum of these signals. The X-rays are incident at an angle θ to the sample plane, reflect off certain atomic planes and are detected opposite the source (at the same angle to the sample plane). The angle θ is then varied, with source and detector remaining symmetrically aligned, so that atomic planes with different spacing are detected. Only planes of atoms which are roughly in-line with the mirror plane will produce a signal, although finite beam width, finite detector width

and finite crystallite size allow a small range of atomic plane angles around this mirror plane to contribute. The peak width of a particular series of atomic planes is a convolution of a number of factors, namely: finite source width, finite detector width, the range in the X-ray wavelengths from the source, strain within the crystal, and crystallite size. The first three are generally described as the machine width, and can be corrected for in a variety of ways. Strain in this case refers to a narrow distribution of inter-atomic spacing around the equilibrium value, and so is not the same as a macroscopic strain such as the tensile strain discussed in Section 4.1. Peak broadening is also affected by average crystallite size and by the distribution of crystallite sizes (although the latter is often ignored).

There are a number of ways of analysing XRD peak broadening data, including Scherrer [30], Williamson-Hall (WH) [31] and Rietveld refinement [32]. Rietveld refinement uses a computer program to vary user-inputted crystal structure parameters to get a best-fit to XRD spectra, and crystallite sizes obtained from this have been found to be in good agreement with TEM studies [33]. However, Rietveld refinement can be time-consuming, meaning that WH and Scherrer analysis techniques remain popular [34]. Of these, WH can be used to estimate both microstrain and crystallite size, using the different angular dependence of their broadening effects. However, peaks at high angles are often indistinct and convoluted with each other in milled samples (such as those in this work), making accurate WH analysis impossible. In addition, approximations made in the derivation of WH mean that, without corrections from a parallel TEM study, it does not provide accurate quantitative analysis [34]. Therefore, for this work, Scherrer analysis has been used, as it is quick and does not require peak width data at a wide range of angles. However, although Scherrer analysis provides reliable qualitative information about relative disorder in a series of samples, absolute crystallite sizes calculated in this way must be treated with caution. The main approximations [35] in the derivation of the

Scherrer equation are that: the powder sample has small cubic crystals, there are no faults or strain in the crystals and the peak shape can be fitted to a Gaussian curve for the purposes of peak integration. This leads to the equation:

$$B(2\theta) = {}^{0.94\lambda}/_{LCos\theta} \tag{3.3.1}$$

where $B(2\theta)$ is the 2θ machine-width-corrected Full Width Half Maximum (FWHM) of the XRD peak (in radians), λ is the wavelength of X-rays used (1.5418 Å in this case), θ is the Bragg angle and L is the Scherrer crystallite size. In this work, the machine-width is taken to be the FWHM of a Nb_3Sn sample with large grain size, and rather than simply subtract this from peak widths, the following approximation is used as it is more accurate [35]:

$$\Delta(2\theta)_{Corrected} = \sqrt{\Delta(2\theta)_{Raw}{}^2 - \Delta(2\theta)_{MachineWidth}{}^2} \tag{3.3.2}$$

where $\Delta(2\theta)_{Raw}$ is the FWHM of the raw XRD spectrum, $\Delta(2\theta)_{MachineWidth}$ is the FWHM of the same peak for a Nb_3Sn sample with large grain size and $\Delta(2\theta)_{Corrected}$ is the broadening in the FWHM due to factors other than the machine width.

It should be noted that the peak intensity is reduced as disorder increases, and non-crystalline phases appear as an increased background. Because XRD spectra in this thesis are normalised to the maximum peak intensity for clarity, this gives a false impression that the noise on the data has increased. Please note also that there are different ways of defining where on the scale from no long-range order to no short-range order a sample becomes "amorphous". Therefore, for clarity, samples whose XRD peaks are too broad and convoluted to accurately determine a FWHM value for will be referred to as "X-Ray amorphous" in this work. Transmission Electron Microscopy (TEM) studies of samples would be required to ascertain the exact level of micro-structural order.

3.4 Inductively Coupled Plasma - Mass Spectrometry

3.4.1 Introduction

Although X-Ray Diffraction can provide data on crystalline phases in samples, it provides very little information about contamination at low levels or about the exact ratio of elements within a phase. Inductively Coupled Plasma Mass Spectrometry (ICP-MS) is a sensitive elemental analysis technique which measures the total amount of a particular element in a sample. All ICP-MS measurements were made by C J Ottley in the Earth Sciences department, although initial sample preparation and subsequent data analysis are the responsibility of the author. The basic principles of ICP-MS will be described in Section 3.4.2. The use of ICP-MS was new to the group, and so the results of standardisation experiments will then be discussed in Section 3.4.3.

3.4.2 Overview of technique

ICP-MS uses an inductive-coupling method to produce the high temperatures needed to ionise atoms from a sample, which are then analysed using standard Mass Spectrometry. ICP-MS is a destructive technique, so it is desirable to minimise the sample mass analysed. In the cases of determining contamination levels (typically 1 %) or the exact Nb:Sn ratio, the sample mass required will not be limited by ICP-MS sensitivity (which is at the ppb level). Instead, ensuring that the sample is representative of the material as a whole and minimising weighing errors are more important considerations, and for these reasons a sample mass of ~100 mg is used. Following accurate mass determination, the sample is dissolved in a suitable acid – typically a combination of HF and HNO_3 for niobium-based compounds. For accurate compositional analysis, it is critical to ensure that the sample is fully dissolved and this is achieved by:

choosing the solvent with reference to the literature, allowing a lengthy dissolution period with heating, and a final visual inspection. Subsequent sampling and dilution in de-ionised water bring the concentration (of elements in the sample to be analysed) down to the ppb by weight level. A peristaltic pump and nebuliser are used to create an aerosol of the sample at a steady rate, and a spray chamber allows only the finest aerosol droplets (~5-10 μm) to pass into the plasma torch, representing only 1-2 % of the sample solution. The torch is an argon gas plasma heated to 6000-7000 K by RF inductive coupling. Sample ions in the fine aerosol undergo rapid desolvation, vaporisation, atomisation and ionisation after they are injected into the base of the torch. Ions then pass through an interface region operating at ~2 Torr (~200 Pa) into a standard mass spectrometer operating at ~10^{-6} Torr (~10^{-4} Pa). The mass spectrometer is used to measure the Counts Per Second (CPS) signal at m/z ratios specific to the isotopes being looked for. Comparison of these signals with those of standard solutions with elemental concentrations around that expected of the sample allow the elemental concentration to be determined, and by working back from the dilution process and the original sample mass, elemental composition by weight can be determined.

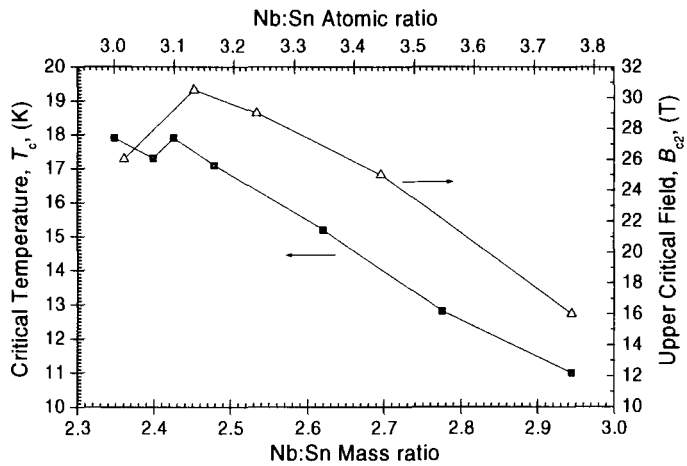

Figure 3.6 Plot of T_c and B_{C2} (determined resistively) against Nb:Sn ratio in thin-film Nb_3Sn (Flukiger [36], Orlando et al. [21]). Thin-film data is used due to the difficulty of forming off-stoichiometric bulk samples, but still gives some indication of the scale of stoichiometry effects.

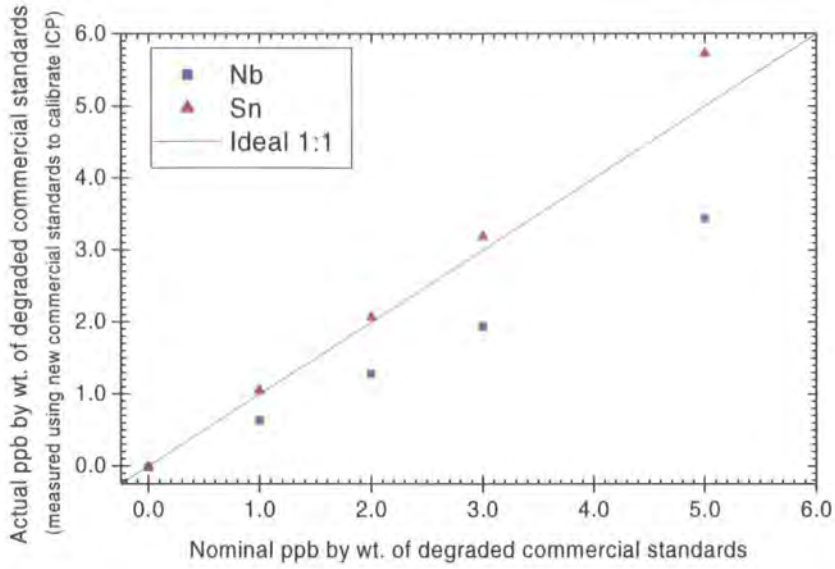

Figure 3.7 Measurement of niobium and tin ppb by weight of a standard stored in a dilute state, which originally had a Nb:Sn mass ratio of 1. Niobium ions have precipitated out of solution over time, which would introduce a large systemic error if the standard was used for calibration. Measurement made by C J Ottley.

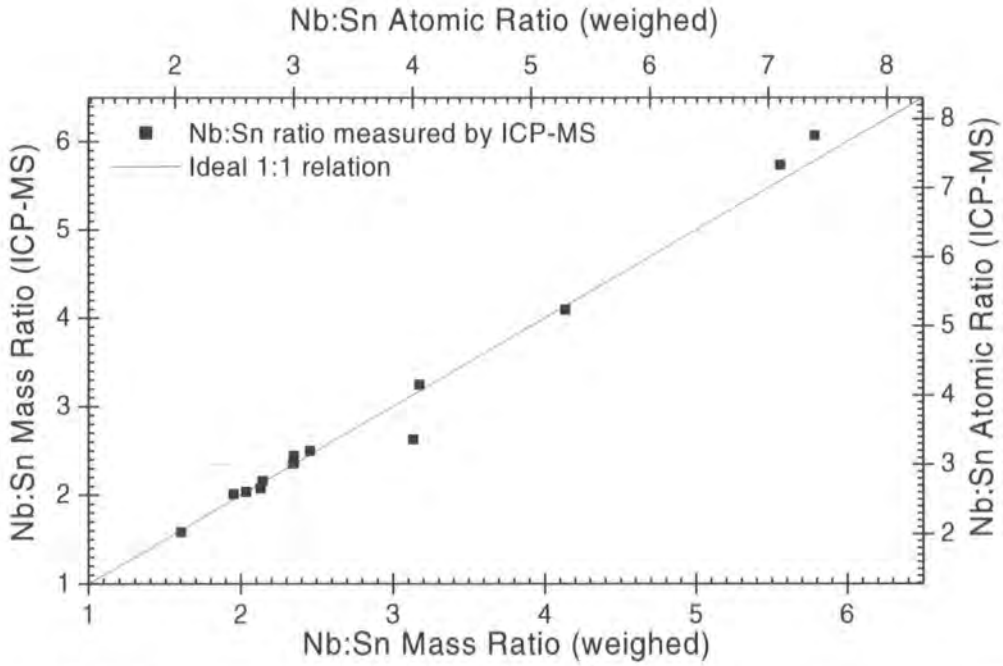

Figure 3.8 Plot of Nb:Sn ratio (atomic and mass) determined by ICP-MS against Nb:Sn ratio of as-weighed standard samples. This consistency check can be used to estimate the error in determining the Nb:Sn ratio by ICP-MS. This does not reflect the error involved in measuring contamination levels, as it excludes errors introduced by the dilution process. Measurement made by C J Ottley.

Because ICP-MS is so sensitive, it is typically used for determining impurities at very low levels. In the work presented in this thesis, the technique has been used in a different way - primarily to determine the Nb:Sn ratio in Nb_3Sn samples, as a ~2 % change in Nb:Sn mass ratio could equate to decreases in T_c and B_{C2} of ~6 % (Figure 3.6). A series of standardisation experiments were carried out to determine the errors involved in this process.

3.4.3 Standardisation experiments

As mentioned in Section 3.4.2, translation of a sample's raw CPS data into elemental concentrations is based on a calibration line. A commercial standard solution with a known concentration of a specific element is diluted in stages to produce solutions with concentrations around that of the sample to be measured. The calibration line is then based on measurement of these known solutions and so the reliability of the original commercial standard's concentration is absolutely critical. It was found that if a standard solution is stored in a dilute state, ions could precipitate out of solution over time, leading to large systemic errors (Figure 3.7). This problem was eliminated by only storing the standard solution in its (as-supplied) concentrated state, and by preparing a solution of a bench-marked Nb_3Sn powder with each measurement. When this systemic error had been eliminated, a series of samples with known Nb:Sn ratios was run. Figure 3.8 indicates that the error in measuring the Nb:Sn mass ratio in Nb_3Sn was around 2 % for this run of measurements. More detailed analysis reveals that this error is largely due to instrument drift over the course of the measurement run, which could be reduced further by running standard solutions immediately before and after each sample.

It is relative Nb:Sn signal strengths not absolute signal strengths which are important for working out Nb:Sn mass ratios, but when calculating contamination values, absolute signal strengths become crucial. By comparing the contaminant signal strength from a

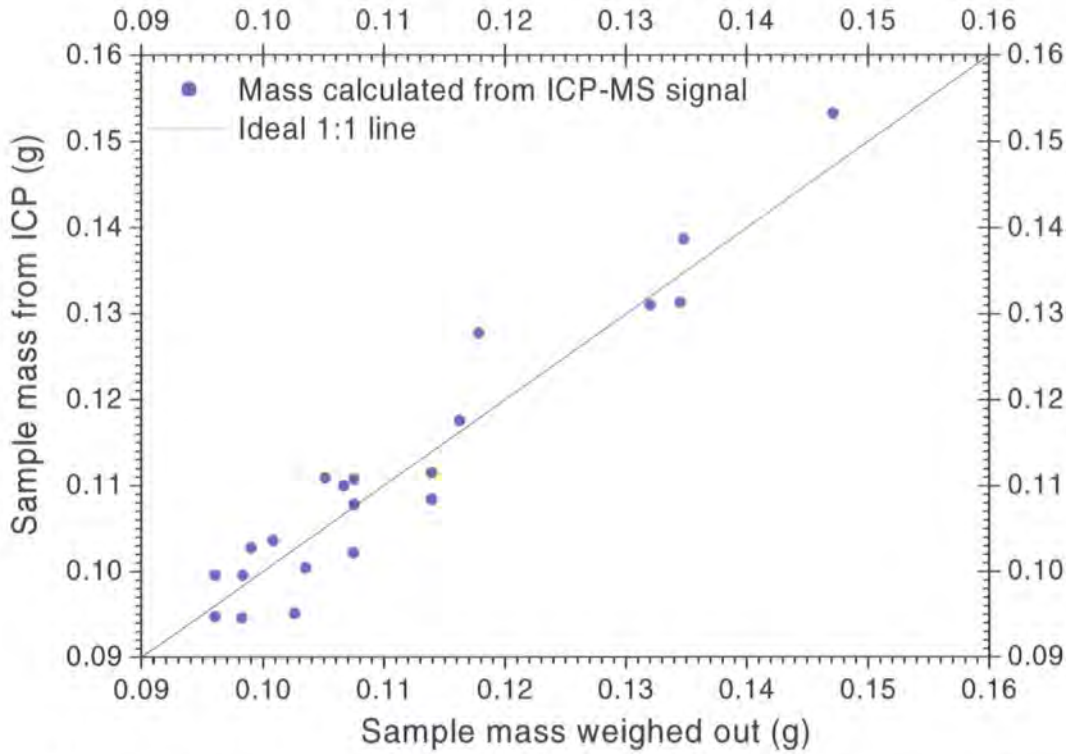

Figure 3.9 Plot of sample mass worked back from ICP-MS signal strength against the weighed sample mass for Nb-Sn powders. This consistency check can been used to estimate the error in determining contamination levels. This error is not a reflection of the error in measuring elemental ratios (e.g. Nb:Sn), as the accuracy of the dilution process has no effect on this. Measurement made by C J Ottley.

sample solution with that of a known standard, the concentration of contaminant in the solution run is calculated. The dilution process used to create the sample solution is known, so the original contaminant mass is worked back, and as the original total sample mass is also known, a percentage by mass of contaminant is arrived at. Sources of error which were not important for Nb:Sn ratio determination but are now important are introduced by the dilution process and by differences in the way sample solutions and standard solutions are delivered into the plasma torch. By comparing the weighed sample masses of pure Nb and Sn powders with those back-calculated from the resulting signal strengths (Figure 3.9), the error in determining contamination levels is shown to be around 5 % for this run of measurements.

The standardisation experiments highlighted the need for standards to be run before and after sample solutions, and the importance of using fresh standards which could not have degraded. Unfortunately, there are no viable alternatives for quantitative determination of elemental composition. Some work has been carried out to assess the use of Proton-Induced X-Ray Emission (PIXE) [37] which is potentially a more attractive alternative to ICP-MS, as it is non-destructive, but this is still work-in progress and it is as yet unclear whether this would offer improvements in accuracy. Other techniques such as electron microprobe analysis could give useful indication of overall composition, but provide a fundamentally local measurement and so are of limited use.

3.5 Physical Property Measurement System (PPMS)

3.5.1 Introduction

Measurements of the resistivity and magnetic properties of samples in this work were made using a Quantum Design (QD) Physical Property Measurement System (PPMS) with an A.C. Measurement System (ACMS) attachment. The measurements were computer-controlled, including automated temperature and magnet control. The PPMS system used can apply magnetic fields up to 9 T, and temperatures down to ~2 K. Details of sample preparation are outlined in the next section. The ACMS can be used as a d.c. magnetometer or an a.c. susceptometer, and these are briefly discussed in Sections 3.5.3 and 3.5.4 respectively.

3.5.2 Sample preparation

Measurements detailed in this thesis were made exclusively on bulk samples (i.e. with dimensions ~mm). Bulk samples were shaped using fine emery paper, weighed and

dimensions measured using a micrometer. Two-part gelatin capsules were used to keep the sample fixed in position during the measurement. The gelatin capsules used were similar to those used for containing medicines, and have two cup-shaped halves which slot together. The sample was positioned and aligned inside the wider half of the capsule. The bottom of the thinner half of the capsule was then wrapped in 7.5 x 10^{-5} m thick PTFE tape and jammed down into the wider half to fix the sample in position. This meant that the two cup-shaped halves of the capsule were nesting, with the sample trapped in between. Small holes were punctured in the capsule to allow air to escape during evacuation of the sample chamber. Additional PTFE tape was then wrapped around the sample capsule and this was then pushed down inside a plastic straw. It is important to note that the sample was firmly fixed in position by this process, as measurements involved quick movements of the sample. The straw was cut to length, so that when it was mounted on the ACMS probe, the centre of the sample was aligned to within 2 mm of the centre of the drive and detection coils. Finer sample positioning was automated by the ACMS. Approximately 30 small holes were then punctured along the length of the straw to allow air to escape during sample chamber evacuation. The straw with the sample at the end was then mounted on to the end of a thin, rigid sample rod with a motor to move the sample longitudinally within the sample space.

3.5.3 DC magnetometer

During d.c. magnetometer measurements, the applied magnetic field from the PPMS was kept constant, and the motor on the sample rod was used to swiftly (~1 m s^{-1}) extract the sample from copper detection coils on the ACMS, inducing a signal from which the sample's magnetic moment was automatically calculated. The speed of extraction allowed several measurements to be quickly taken at each field and

temperature. In this work, the d.c. magnetometer was used to measure hysteretic magnetic moment at a fixed temperature as applied field was slowly ramped up and down, which could be used to estimate J_c, the critical current density of the sample (see Sections 2.3.1 and 7.2).

3.5.4 AC susceptometer

During a.c. susceptometer measurements, drive coils on the ACMS insert applied a small alternating magnetic field (e.g. amplitude ~10^{-4} T, frequency ~10^3 Hz) to the sample, in addition to the larger stable field applied by the PPMS (~1 T). The magnetic response of the sample induced a signal in the ACMS detection coils, whose amplitude and phase were automatically analysed to extract the sample's real and imaginary magnetic moment components. In this work, a.c. measurements of magnetic moment at particular applied fields were taken as temperature was ramped down, which can be used to determine samples' superconducting transition points (Section 7.3).

Chapter 4

Electroplating titanium using HF

4.1 Introduction

The major market for superconductors is in the production of high-field electromagnets, most notably for the ITER nuclear fusion tokomak [39]. Nb_3Sn is a brittle material, and strain has a considerable effect on its superconducting properties. Nb_3Sn is too brittle to be drawn into thin filaments, so commercial Nb_3Sn wires are typically formed by encasing strands of more ductile Nb_3Sn precursor materials within a copper matrix. Wires are then drawn out and shaped before Nb_3Sn formation during a heat treatment (~1000 K). As the operating temperature for electromagnets made in this way is ~4.2 K, the differential thermal contraction between the Nb_3Sn strands and the

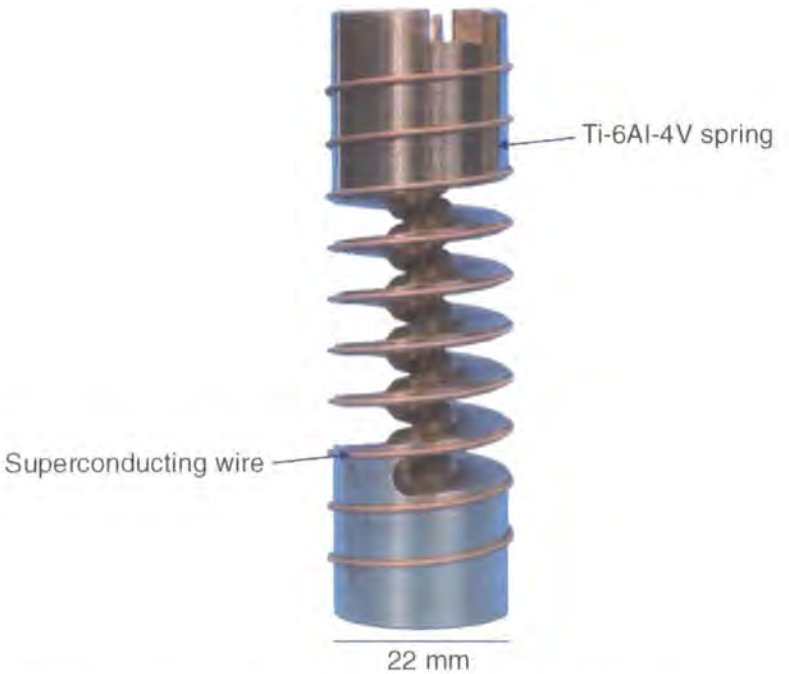

Figure 4.1 Ti-6Al-4V alloy "Walters" spring used in variable strain measurements [38].

copper matrix on cooling by ~1000 K is considerable, and this introduces strain into the wires. In strong electromagnets, the Lorentz forces on the superconducting strands are significant, and this also introduces strain. The ITER fusion reactor is a multi-billion dollar project, and so in recent years it has become imperative to accurately characterise the critical current of candidate wires as a function of strain, temperature and field. The Superconductivity Group in Durham has developed considerable expertise [40] in measuring this strain-dependence. Tensile and compressive strains need to be applied uniformly along the length of the wire and this, together with the space constraints of working within the bore of a high field magnet, means that a modified Walters [41] spring (Figure 4.1) is used. The wire is soldered to the outside of the thick coils, and strain is then applied by turning one end of the spring with respect to the other. In order to reliably transmit the strain from the spring to the wire, it is crucial for the wire to be firmly attached to the spring at all points along its length. Initial strain work in Durham used a copper-beryllium spring, which was easy to solder to, but a comparative study of spring materials [38] showed that the higher elastic limit of the engineering alloy Ti-6Al-4V improved both the strain range available and the uniformity of strain along the length of the wire. However, Ti-6Al-4V is extremely reactive in air, and forms a very stable oxide layer on its surface, making it difficult to form the metal-metal bond needed to attach the wire. Hydrofluoric acid (HF) is the only acid which will remove the oxide layer, but after removal of this layer, the titanium must be prevented from forming a new oxide layer. Work in this section describes a method developed from a Rolls Royce patent [42], which uses a HF-based etch to remove the oxide layer but then protects the surface from re-oxidation until it is electroplated. However, HF is a highly corrosive and dangerous acid, and so Health and Safety (H+S) and materials considerations will be discussed in Sections 4.2.1 and 4.2.2 respectively.

4.2 Experimental

4.2.1 H+S considerations

As mentioned above, hydrofluoric acid (HF) is essential for the removal of the titanium oxide layer, because of its corrosive properties. However, this reactivity also makes HF potentially dangerous, and fatal accidents [44] have highlighted the need for stringent health and safety precautions. HF causes severe and very painful burns on contact with skin, and fumes from concentrated HF (such as that used in this work) are extremely hazardous on inhalation. In addition, HF readily penetrates deeper tissues, and reaction between calcium ions in the body and fluoride ions from HF can lead to hypocalcaemia (calcium deficiency). So as well as causing visible damage, exposure to HF can result in metabolic changes culminating in organ failure, which is the cause of most HF fatalities. The aim of this work was to set up a safe electroplating procedure which would be used by future members of the group. Therefore, the emphasis was on

Table 4.2 Materials specifically corroded or not corroded by HF [43].

Corroded		Not corroded	
Metals	Non Metals	Metals	Non Metals
aluminium	ABS	Hastelloy	Chemraz (FPM)
aluminium bronze	acetal copolymer	Monel	ETFE (Tefzel)
brass	CPVC	nickel	Halar
carbon steel	Epoxy	gold	Hypalon
cast iron	Nylon	platinum	Kalrez (FPM)
high silicon iron	bisphenol A polyester	silver	Koroseal
silicon bronze	EPT	bronze (< 40% conc.s)	Neoprene GR-M
silicon copper	NBR	copper (< 40% conc.s)	polypropylene
Inconel	polysulfides	lead (< 40% conc.s)	PVDF (Kynar)
Incolloy	SBR Styrene (Buna-S)		Teflon® (FEP and TFE)
stainless steels	hard rubber		PTFE
tantalum	natural rubber		Viton
titanium	silicone rubbers		
zirconium	coal tar epoxy		
bronze (> 40% conc.s)	epoxy polyamide		
copper (> 40% conc.s)	Polyester		
lead (> 40% conks)	Vinyl		
	glass		
	silicate ceramics		
	leather		

step-by-step instructions which, if followed, would minimise the risk of HF-exposure. The exact details of this procedure will not be included here, but the key safety precautions will be outlined.

When making up the HF-etch, HF was added drop-wise using a dedicated HF-dispenser. Concentrated HF was always transported within a screw-top canister. When not in use, all chemicals were kept in a lockable cupboard which, as well as the lab itself, was labelled to warn of their presence. The work area was sealed off for the duration of the work involving HF, although this time was minimised to less than 15 minutes (Section 4.2.3). Work was restricted to normal working hours and was never undertaken alone. In practice, this meant that for the 15 minutes that the HF work was being carried out, there was another person in the room aware of safety procedures. HF was used exclusively on HF-proof trays in a fume cupboard to reduce the chances of vapour inhalation and to contain any spills. When completely closed, the sash of the fume cupboard provided complete protection, and the step-by-step instructions ensured that the sash was partially open for only a few minutes when the HF-etch bottle was open. Tripping-up, and spilling chemicals on to an unprotected lap whilst seated, are both common accidents in chemistry laboratories, and so all stools were cleared away. Special protective clothing was worn during the HF-work itself, which could be replaced by ordinary lab-clothing when the HF-etch had been put away. A lab coat, inner nitrile gloves, outer neoprene-coated gauntlets, lab coat, rubber apron, PVC boots, a face mask and a dust-mask were worn. There was a danger that if protective clothing was too impractical, it could have caused more accidents than it prevented, so the procedure set up eliminated any need for manual dexterity when wearing the gauntlets. Stable, wide-necked bottles and funnels allowed easy and safe liquid transfer.

It was also important to consider the procedure in the event of a spill, so a neutralising slaked lime solution was always on hand, together with spill granules to

absorb any liquid so that it could be swept up. HF-waste could be neutralised by pouring it into a half-full bottle of (basic) slaked lime solution for safe disposal. In the unlikely event of skin contact, the most important course of action is immediate rinsing in copious amounts of water, removal of clothing around the area and liberal application of calcium gluconate gel (which both neutralises and helps prevent hypocalcaemia). Hospital treatment is essential, regardless of the scale of the contact, and medical information on HF was on hand to be taken with a casualty. A two-way respirator was also provided in the extremely unlikely event of inhalation. Providing caution is exercised, these precautions reduced the risks associated with the electroplating procedure to very low levels.

4.2.2 Materials considerations

The highly corrosive nature of HF meant that containers, tools, surfaces and protective clothing had to be chosen with considerable care. As can be seen from Table 4.2: polypropylene (PP), Teflon® (TFE by DuPont) and PTFE are not corroded by HF. Copper is also resistant to HF when the HF concentration is below 40 % (which it was for the etch). Funnels for transferring the etch, drip trays to contain spills, and all storage bottles used were made of polypropylene; and a Teflon® beaker and spatula were used for the HF-etch process. A dedicated jig was specifically designed for transferring the spring into and out-of the HF etch, consisting of a thin copper rod with a protective TFE heat-shrink coating, which threaded through the central axis of the helical spring. Solid Teflon® end-pieces screwed on to the ends of the rod to keep the spring in place, and the rod was sufficiently long that hands could be kept ~10 cm from the etch during transfer. Protective clothing was also chosen with care. Neoprene-coated gauntlets are HF-proof. Whilst not resistant over a long period, the thick rubber apron, lab-coat and PVC boots also provided an excellent barrier, preventing skin exposure.

Table 4.3 Composition of chemicals needed for HF etch and nickel-plating process.

Description	Components	mass (g)	volume
HF etch	dimethylformamide	607	640ml
	water	290	290ml
	35 % hydrofluoric Acid	107	91ml
nickel-plating solution	nickel sulphamate	230	
	water		make up volume to 900ml
	nickel chloride	4	
	boric acid	19	

4.2.3 Electroplating procedure

The HF-etch and the nickel-plating solutions were made in advance to the compositions in Table 4.3. The HF etch was made up in the engineering department in Durham using facilities in which HF is regularly used. This allowed access to dispensers specifically designed for concentrated HF use, thereby minimising the risk of skin contact. The use of standard laboratory equipment in a fume-cupboard was sufficient for making the nickel-plating solution, so this was done in the physics department. The spring's surface was first thoroughly degreased using acetone and cotton buds, followed by rinsing in methanol. This cleaning process ensured even etching and hence even plating, and the spring was then mounted on the dedicated jig. The jig's TFE sheath both protected its central copper rod from the HF-etch, and provided electrical insulation to prevent the copper from being electroplated. Electrical contacts were attached prior to etching, so that the electroplating circuit could easily be completed using a crocodile clip even when wearing neoprene gloves. The nickel-plating solution was set up with the nickel-plate anode to provide a current of ~1 A, so that the activated (etched) Ti spring could be transferred straight from the HF solution for immediate electroplating. The

room was then prepared for HF-work, as described in Section 4.2.1. The HF etch was transferred into a beaker, and the spring on its jig was lowered into the etch. Etching took 10 minutes, during which the spring evolved gas bubbles and an even grey coating formed, which provided protection against oxidation. The spring was slowly pulled out of the etch and transferred into the nickel electroplating solution for immediate electroplating. The HF etch was transferred back into the storage bottle and sealed. After rinsing the funnel, beaker, etch storage bottle, drip trays and protective gloves, the HF bottle was stored away and HF-precautions could be relaxed. Nickel plating took around 10 minutes, and a superconducting wire could then be attached to the Ti-6Al-4V spring using standard copper electroplating and soldering.

4.3 Results of electroplating

Bringing this procedure in-house ensured that each spring was electroplated in the same way, removing any doubt from data comparisons. Springs electroplated using the method outlined above have been used in a number of experiments, specifically at the high field facility in Grenoble [38, 45]. In these experiments, measurements on wires have successfully been made with strains from -1 % (tensile) to +0.3 % (compressive). In summary: a safe procedure has been set up, based on a patented process, to allow the attachment of superconducting wire to an engineering alloy which is notoriously difficult to form a bond with. This method of attachment has successfully transmitted applied strain without failing.

Chapter 5

Ball milling

5.1 Introduction

In this chapter, work on creating Nb_3Sn powder with a disordered microstructure by ball milling pre-alloyed Nb_3Sn using three milling machines (Section 3.2), is presented. Milling conditions used and data from samples produced are tabulated in Section 5.2, followed by a discussion of the effect milling parameters have on the most important sample characteristics: yield (5.3.2), contamination (5.3.3) and microstructure (5.3.4).

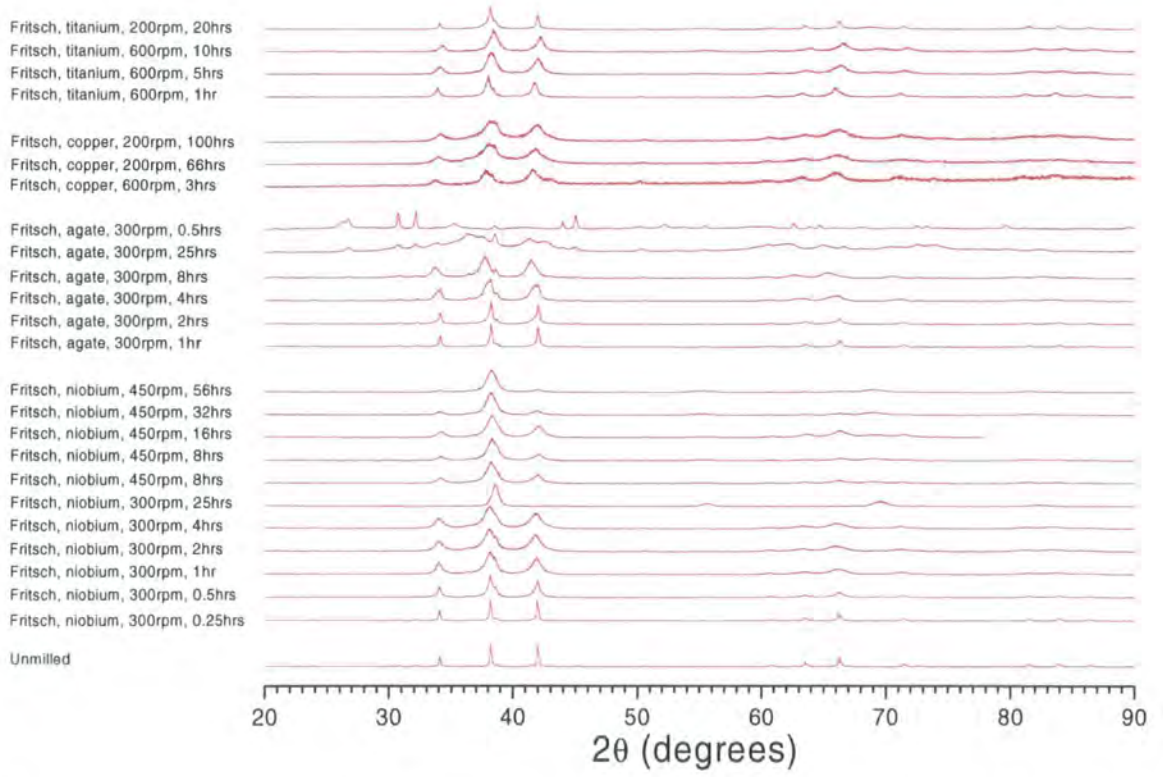

Figure 5.1 Compilation of all XRD spectra from samples milled using Fritsch miller in niobium, agate, copper and titanium milling media at a range of speeds

Table 5.1 Summary of Nb_3Sn samples milled in Fritsch miller. Note that due to a larger time penalty associated with putting Fritsch pots into an argon glove box, scraping every 30 minutes and cooling (used for SPEX and Retsch millers) were not used as parameters for Fritsch milling.

Miller	Media [a]	Speed (rpm)	Mill time (hours)	BPR	Yield (%)	Scherrer grain size (nm)	Weight % contaminant			
							Nb (extra)	Agate	Ti	Cu
Fritsch	niobium	300	0.25	59	94	~1000				
Fritsch	niobium	300	0.50	74	-	34				
Fritsch	niobium	300	1	59	-	12				
Fritsch	niobium	300	2	60	-	9				
Fritsch	niobium	300	4	60	90	8				
Fritsch	niobium	300	25	50	205	large Nb peak interference				
Fritsch	niobium	300	60	~60	-	large Nb peak interference				
Fritsch	niobium	350	35	5.8	18					
Fritsch	niobium	300	10	22.3	23					
Fritsch	niobium	150	1.75	43.3	40					
Fritsch	niobium	150	8	43.3	12					
Fritsch	niobium	450	0.5	∞ (no powder)	∞ (3.636 g)					
Fritsch	niobium	450	8	43	65					
Fritsch	niobium	450	8	42	75					
Fritsch	niobium	450	8	34	73	20	25			
Fritsch	niobium	450	8	36	195	20	27			
Fritsch	niobium	450	16	42	116	19				
Fritsch	niobium	450	32	42	275	22				
Fritsch	niobium	450	56	~40	~200	20				
Fritsch	agate	300	0.5	18.3	85	-				
Fritsch	agate	300	1	17.9	97	176				
Fritsch	agate	300	2	18.8	99	107				
Fritsch	agate	300	4	18.3	95	18				
Fritsch	agate	300	8	19.0	104	18				
Fritsch	agate	300	25	~20	~110	large interference peaks		10		
Fritsch	agate	300	50	~20	~110	large interference peaks				
Fritsch	agate	300	60	22.6	178	large interference peaks				
Fritsch	agate	300	75	~20	~110	large interference peaks				
Fritsch	agate	300	100	~20	~110	large interference peaks		21		
Fritsch	agate	300	200	~20	~110	large interference peaks				
Fritsch	copper	600	0.5	~40	0	-				
Fritsch	copper	600	1	~40	0	-				
Fritsch	copper	600	1.5	~20	13	-				1.6
Fritsch	copper	600	2	~8	35	-				
Fritsch	copper	600	2.5	~6	27	-				
Fritsch	copper	600	3	~6	25	24				5.9
Fritsch	copper	200	25	~9	0	-				
Fritsch	copper	200	66	~9	8	13				5.2
Fritsch	copper	200	100	~9	0.1	11				
Fritsch	copper	200	50	~6	5	-				
Fritsch	copper	200	100	~9	0	-				
Fritsch	copper	200	50	~9	1	-				
Fritsch	titanium	600	0.5	8	70					
Fritsch	titanium	600	1	8.1	76	43			10	
Fritsch	titanium	600	2	9.4	52					
Fritsch	titanium	600	5	9.4	63	24			16	
Fritsch	titanium	600	10	9.6	13	31			23	
Fritsch	titanium	200	100	~4	8	-				
Fritsch	titanium	200	200	~7	15	-				
Fritsch	titanium	200	220	~10	25	-				
Fritsch	titanium	200	240	~5	24	-				

[a] milling media purity: 99.95 wt. % niobium, 99.95 wt. % copper, 99.8 wt. % titanium, agate pot bought commercially

5.2 Samples produced

5.2.1 Fritsch

As discussed in Section 3.2, the Fritsch Pulverisette 6 (P6) is a planetary ball miller. In all but the final stages of the work presented in this thesis, the Fritsch P6 was the only miller available. The milling medium, milling speed, ball-to-powder weight ratio (BPR) and milling time were varied in an attempt to produce amorphous Nb_3Sn powder at acceptably high yields and with low contamination levels. The details of samples produced are set out in Table 5.1, together with sample characterisation from XRD (Figure 5.1 and Section 3.3) and ICP-MS data (Section 3.4).

Table 5.2 Summary of Nb_3Sn samples milled in SPEX 8000D and Retsch MM301 millers.

Miller	Media	Cooled?	Scraped?	Mill time (hours)	No of balls	Ball Wt (g)	Powder wt (g)	BPR	Yield (%)	Grain size (nm)	Weight % contaminant Fe	WC	Cu	
SPEX	steel	not cooled	not scraped	8	7	24.73	3.00	8.2	8	9	1.8			
SPEX	steel	not cooled	scraped	4	3	10.69	3.69	2.9	114	12	0.18			
SPEX	steel	not cooled	scraped	8	7	25.09	3.10	8.1	86	A	0.4			
SPEX	steel	cooled	scraped	8	7	25.04	2.97	8.4	62	A	1.9			
SPEX	steel	cooled	scraped	12	7	25.04	2.97	8.4	67	A	1.1			P
SPEX	WC	not cooled	not scraped	8	2	23.48	3.17	7.4	37	7		2.3		
SPEX	WC	not cooled	scraped	8	2	23.42	2.56	9.2	76	A		2.3		
SPEX	WC	not cooled	scraped	10	2	23.42	2.56	9.2	83	A		2.9		
SPEX	copper	not cooled	scraped	8	4	19.28	4.79	4.0	60	8			5.4	
SPEX	copper	cooled	scraped	8	4	19.72	4.62	4.3	87	8			4.8	
SPEX	copper	cooled	scraped	12	4	19.72	4.62	4.3	84	A			6.0	
SPEX	copper	cooled	scraped	16	4	19.72	4.62	4.3	44	A			8.3	
Retsch	steel	not cooled	scraped	4	3	10.69	3.67	2.9	80	80	0.04			
Retsch	steel	not cooled	scraped	8	7	24.74	3.89	6.4	98	40	0.06			P
Retsch	steel	cooled	scraped	8	12	25.01	3.14	8.0	48	190	0.04			
Retsch	steel	cooled	scraped	12	4	25.01	3.14	8.0	43	80	0.05			
Retsch	WC	not cooled	scraped	8	1	64.54	7.06	9.1	14	8		0.3		
Unmilled	steel			0							0.02			
Unmilled	WC			0								0.06		
Unmilled	copper			0									0.02	

A: Samples which are too amorphous for peak widths to be determined

P Samples which were pyrophoric and needed special handling

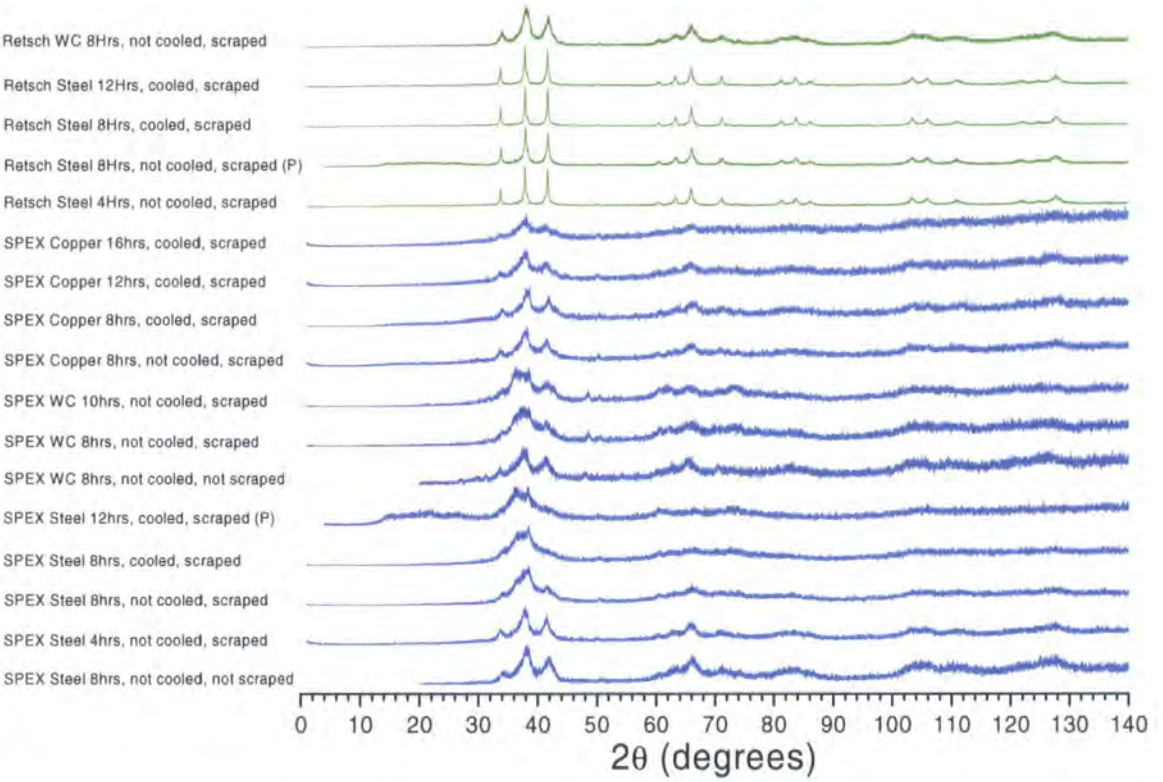

Figure 5.2 XRD spectra of the Nb_3Sn samples milled using SPEX and Retsch millers (see also Table 5.2), discussed in detail in Section 5.3. Spectra labelled with a (P) were pyrophoric, and so were measured through 8 μm Kapton® (DuPont) HN polyimide film to prevent combustion.

5.2.2 SPEX

As will be discussed in Section 5.3, the work with the Fritsch P6 miller was characterised by low yield, high contamination and low microstructural change despite extensive experimentation with milling parameters. As outlined in Section 3.2, the SPEX and Retsch millers have a very different action and so these were trialled as an alternative approach. The SPEX 8000D miller is widely used in research work, particularly in the United States. Although the milling speed of this machine cannot be varied, the small vials mean that temperature effects could be easily investigated, as well as the effects of varying BPR, milling medium and milling time. The effect of scraping the sides of the milling vial every 30 minutes in an attempt to improve powder homogeneity and yield was also investigated. The milling parameters and results from comprehensive XRD

(Figure 5.2) and ICP-MS analyses are tabulated in Table 5.2, and will be discussed in Section 5.3.

5.2.3 Retsch

Retsch is a German competitor to SPEX, and their products are primarily used in Europe. The MM301 is Retsch's counter-part to the SPEX 8000D, the notable difference being that the MM301 has a simpler linear milling action but operates at roughly twice the frequency (Section 3.2). The milling parameters varied were the same as those investigated using the SPEX miller, namely: milling media, BPR, cooling, scraping, and milling time. Details of samples produced using this miller are included in Table 5.2, and XRD spectra in Figure 5.2. Results are presented and discussed in the next section.

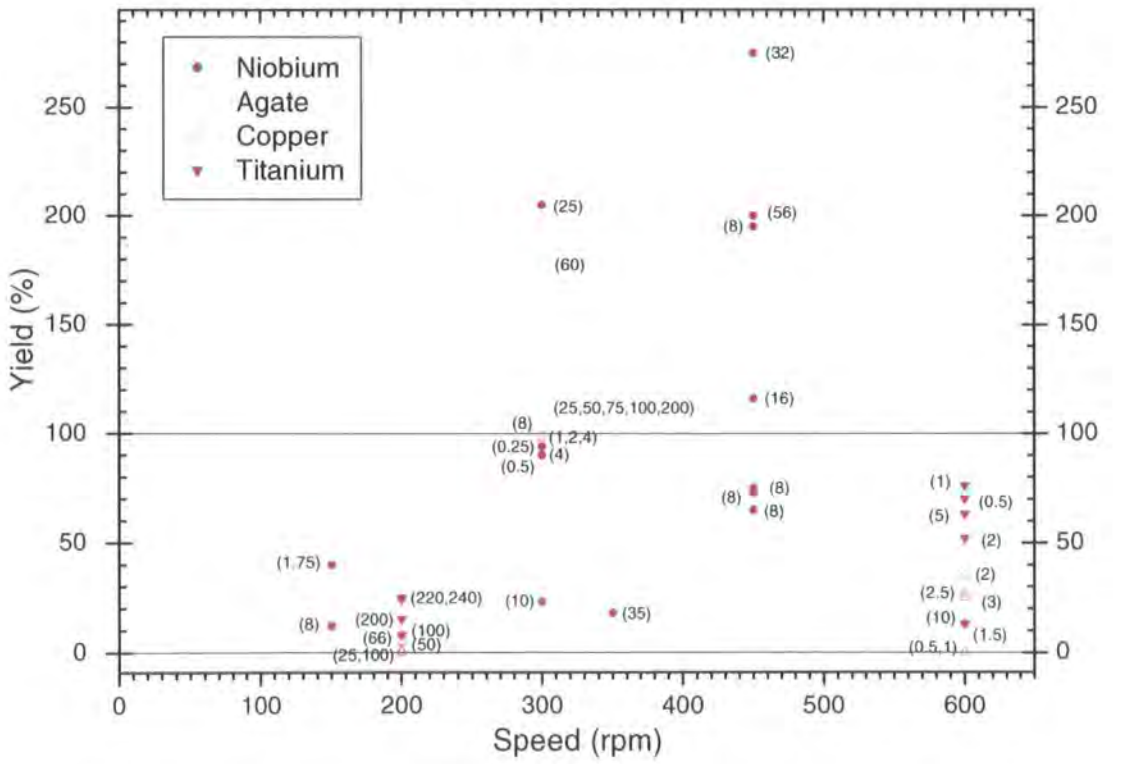

Figure 5.3 The effect of varying milling speed on yield for milling in niobium, agate, copper, and titanium milling media using the Fritsch P6 miller. Milling times (hours) are in brackets.

Figure 5.4 Photographs of 99.95 wt. % copper pot (inner diameter ~10 cm) used in Fritsch P6 milling before milling (left) and after 90 minutes of milling Nb_3Sn (right). In the photo on the left before milling, the loose Nb_3Sn powder can be seen with the clean milling balls of 10 mm and 20 mm diameter. The balls have been taken out of the pot in the photo on the right to show the extent of coating of the pot sides.

Figure 5.5 Photographs of 99.8 wt. % titanium pot (inner diameter ~10 cm) used in Fritsch P6 milling: before milling (left) and after 30 mins (centre) and 60 mins (right) of milling Nb_3Sn. For clarity, the 10 mm and 20 mm diameter milling balls are not included in the photos of the pot after milling.

Figure 5.6 Photographs of the wear patterns on the 99.8 wt. % titanium pot (left) and lid (right).

Table 5.3 Purity of selected materials used in this work

Material	Form	Purity (wt. %)	Specified contamination levels			Supplier
			O (%)	Fe (%)	Ni (%)	
niobium	ingot	99.95	0.0094	< 0.001		Ulba Metallurgical Plant, Kazakhstan
copper	ingot	99.95 [a]	< 0.001 [a]	< 0.001 [a]	< 0.001 [a]	Smith Metal Centres, U.K.
titanium	ingot	99.8 [b]	0.11	0.06		ATI Titanium International Ltd., U.K.
argon	gas	99.998 [c]				BOC, U.K.
Nb_3Sn	powder (< 250 μm)	99.9 [d]				Goodfellow Ltd., U.K.
tin	powder (< 44 μm)	99.8				Alfa Aesar, Germany
niobium	foil (25 μm)	99.8				Sigma Aldrich, U.K.

[a] Copper is C103 grade, and contamination levels stated are typical values for this grade
[b] Titanium is commercial Grade 2, but values are specific to the batch used
[c] Argon gas used in a glove-box which has oxygen and water filters to reduce levels further
[d] Goodfellow blended and compacted Nb and Sn powders of 99.9 % purity, which were vacuum arc-melted twice and then ground to form the as-supplied Nb_3Sn powder used in this work.

5.3 Results and discussion

5.3.1 Introduction

In the previous section, details of Nb_3Sn samples milled in Fritsch, SPEX and Retsch millers were presented in Tables 5.1 and 5.2. Powder milling can only be considered a success if the yield from the process is at a level which allows enough powder for bulk (HIP'ed) samples to be made on a reasonable time-scale and with minimal waste. Equally, although there are limited data on the effect of contamination on Nb_3Sn's superconducting properties, it is desirable to minimise contamination introduced during milling. Finally, the object of milling Nb_3Sn is to introduce microstructural disorder, with the ultimate aim of creating amorphous powder, and if this is not achieved then high yield and low contamination are of no interest. Consequently, in the following section, data from these samples are presented and discussed in terms of the effect of varying milling parameters on yield, contamination and microstructural change.

Table 5.4 Physical properties of materials used as milling media (pot and balls), and of Nb_3Sn

Material	Density (10^3 kg m^{-3})	Melting pt (K)	Vickers Hardness (10^9 N m^{-2}) [a]	Mohs Hardness (relative)	Thermal conductivity (W m^{-1} K^{-1})	Poisson Ratio	Refs
Copper	8.96	1358	~0.4-0.9	2.5 - 3.0	1401	0.34	[46, 47]
Niobium	8.35	2183	~1.1-1.6	6.0	59	0.40	[46, 47]
Titanium	4.50	1941	~0.6-1.0	6.0	21	0.36	[46, 47]
WC/Co	14.9-15.3	~1700 [b]	~1.2-1.8	8.0 - 8.5 [c]	100-120	0.23	[47, 48]
Hardened Steel	7.7-8.0	~1700	~0.7	5.5 - 6.0	~100	0.32	[48, 49]
Agate	2.65	2000	~1.0	7.0	1.38 [d]	0.17 [d]	[48]
Nb_3Sn	8.95 [e]	~2000	~8-11	-	-	-	[27, 50, 51]

[a] Vickers Hardness in N m^{-2} is related to the traditional unit of kg mm^{-2} using a conversion factor of 1.02 x 10^5 N m^2 kg^{-1} mm^{-2}
[b] Sintering temperature limited by Co binder; melting point of WC is ~3070 K [48]
[c] Hardness quoted is of composite WC/Co; hardness of WC generally stated as 9.0 on the Mohs scale [48]
[d] Values for quartz SiO_2, to give some indication of agate values
[e] Calculation based on lattice parameter of 5.290 Å [51]

5.3.2 Yield

In order to minimise powder agglomeration (and therefore maximise yield), milling media are conventionally chosen for their wear resistance, high density and low chemical affinity for the sample being milled. However, contamination from milling media is inevitable (see Section 5.3.3), and the impact of contaminating superconducting samples with conventional milling media such as stainless steel, tungsten carbide and agate is potentially great. The milling work in this thesis has therefore involved experimentation with unconventional milling media such as niobium, copper and titanium (the latter two being common ternary additions to Nb_3Sn superconducting wires [52]). As can be seen from Table 5.3, the niobium, copper and titanium from which milling media were manufactured (in-house) were of high purity. These milling media are rarely used by other research groups: copper has been used once [53]; titanium once [54]; and niobium balls have been used in conjunction with a vial of a different material [55]. None of these papers quantify agglomeration effects explicitly, and so information in the literature on yield is restricted to the case of milling soft, ductile metals in conventional (hard) media

[56-58]. In contrast, in this work, very brittle and hard Nb_3Sn powder has been milled using comparatively soft milling media (Table 5.4), making the yield data in this thesis particularly interesting.

Initial work used the Fritsch P6 planetary miller, so yields achieved in this miller (Table 5.1) in conjunction with agate, copper, niobium, and titanium media will be discussed first. As might be expected, yields from agate (the hardest milling medium used) are consistently around 100 % (Figure 5.3), suggesting little agglomeration between powder and vial. In contrast, yields from the softer copper, niobium and titanium media are much less consistent and of these, copper results in the lowest yields. In photos of the copper pot (Figure 5.4) after a short milling time (90 minutes) at low speed (200 rpm), a substantial coating of Nb_3Sn can be seen. Copper has a Mohs hardness of only 2.5 - 3.0 (Table 5.4) in comparison to agate (7.0), niobium (6.0) and titanium (6.0), so it seems likely that the low yields (all below 35 %) are, at least initially, due to Nb_3Sn particles adhering to and embedding into the soft copper surfaces. As mentioned above, Figure 5.4 shows that a Nb_3Sn coating quickly forms. It might be expected that yield would stabilise after this coating stage, but in fact yield continues to be low in a variety of milling conditions (Table 5.1), implying that the Nb_3Sn coating increases the chemical affinity between powder and pot resulting in further cold welding. Yields improved slightly (~5 % to ~25 %) on increasing the milling speed from 200 rpm to 600 rpm (the maximum). This small improvement is likely to be due to increased wear between the milling balls and the pot sides, decreasing the overall rate at which the Nb_3Sn coating builds up. However, the limited ICP-MS data available (Table 5.1) suggest that higher milling speeds also result in an increase in the rate at which copper contamination is introduced (Section 5.3.3). Given copper's poor wear resistance (low hardness), it seems plausible that higher milling speeds led to greater milling media wear. In the only other work using copper milling media, Suryanarayana et al. [53] reported

high wear of copper milling media (9 at. % increase in Cu content after 2 hours) using a Fritsch P5 (very similar to the P6). Although no yield data are stated explicitly, this implies that yield problems with copper milling media are not confined to Nb_3Sn.

The results of milling in niobium (Figure 5.3) follow a similar pattern to copper, but with some interesting differences. When the niobium pot was clean, it could be seen that distinct boundaries between powder and milling media were retained for much longer (~8 hours) than was the case for copper (which was coated almost immediately). This is presumably due to niobium's greater hardness delaying Nb_3Sn particles becoming embedded in the milling surfaces. During the initial regime at 300 rpm, with distinct boundaries, yields were consistently high (> 90 %). After surfaces became coated with Nb_3Sn, yield decreased to around 20 % despite all other milling parameters being the same (Table 5.1), and it can be assumed that, as with copper, this can be attributed to a high chemical affinity between the powder and powder-coated milling surfaces. The formation of a Nb_3Sn layer on the milling tools thereby significantly affects the outcome of milling under otherwise identical conditions. Higher milling speeds (450 rpm) resulted in yields considerably higher than 100 %, in conjunction with substantial increases in niobium content (~25 wt. %), implying that, as seemed to be the case for copper, more vigorous milling conditions reduce the agglomeration of Nb_3Sn on to the sides of the pot by increasing wear, but that this increased abrasion also results in niobium pot material being worn away. This is unsurprising given that, although niobium's wear resistance is higher than that of copper, it is still much lower than that of agate or tungsten carbide (see Mohs Hardness, Table 5.4). Presumably, in more wear-resistant milling media, increasing the milling speed could primarily only increase the rate at which the powder coating on the sides is worn off, leading to improved yields. Evidence from milling ductile metals in a planetary miller would seem to support this [58].

Titanium has a similar hardness value to niobium and, like niobium, the titanium milling media retained distinct milling surfaces well during the initial stages of milling (Figure 5.5), with correspondingly high yields (~70 %). Again, the yield dropped substantially (to ~10 %) when the sides became coated, and remained low for all subsequent milling. As with copper and niobium, milling at high speeds led to high contamination rates from the milling media, due to titanium's relatively poor wear resistance (particularly when the initial oxide layer had been worn away). Work by Chu et al. [54] on milling in titanium in a Fritsch P6 miller at 460 rpm does not quantify yields explicitly, but does mention that the titanium content in a $Ti_{40}Mn_{60}$ sample increased by ~4.5 at. % after 40 hours milling, which Chu et al. attribute to milling media wear. Subsequent milling of $Ti_{60}Mn_{40}$ resulted in a decrease in titanium content of ~1.7 %, which is put down to selective adherence of the titanium powder to the titanium balls. As with copper, this provides some confirmation that agglomeration and high contamination are not unique to Nb_3Sn when milling in titanium using Fritsch millers.

In conclusion, using a Fritsch miller in conjunction with soft milling media such as copper, niobium and titanium results in low yields and high rates of contamination which it is suggested is due to: powder particles becoming embedded in the soft media initially; high chemical affinity between powder and pot sides once the Nb_3Sn coating has formed; and the low wear resistance of these metals. The highest yields were achieved when distinct boundaries between the milling surfaces and the powder were maintained, so strategies to achieve this will be discussed later in this section. In contrast to the consistently low yields achieved in copper media using the planetary Fritsch P6 miller, much higher yields are possible (Table 5.1, Table 5.2) in copper using a SPEX 8000D miller (this has been noted before [56]). Milling action (not just the media used) is clearly an important factor and so the effect of the milling action as an explanation for the low yields achieved in the Fritsch miller will be discussed next.

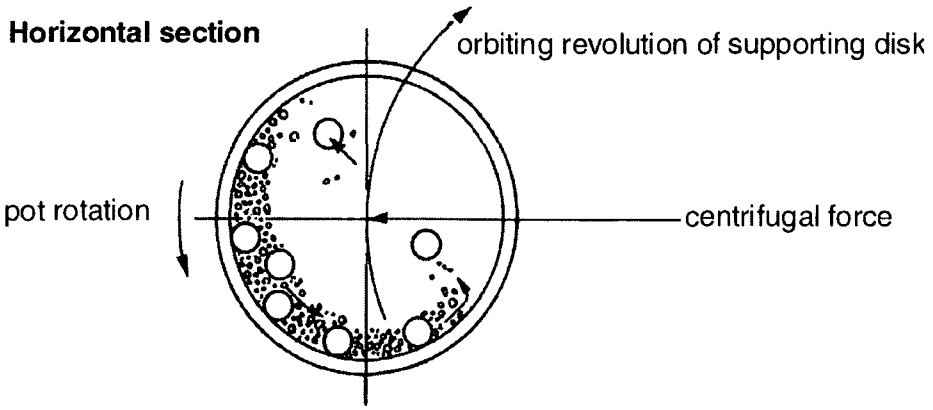

Figure 5.7 Conventional schematic of ball motion in a planetary ball mill [24]

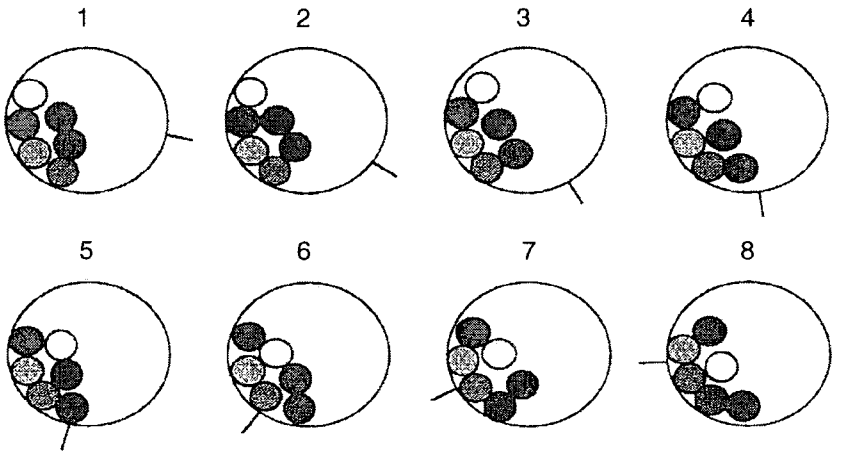

Figure 5.8 Motion of balls within a planetary ball miller from high speed video footage [59], showing that balls spend little time in the centre of the pot, and that collisions occur infrequently during the rotation of the pot. It should be noted that the balls do not move with the pot, resulting in the balls rolling or grinding against the sides of the pot as it rotates.

Figure 5.7 provides a schematic diagram of the conventional view of ball motion in planetary ball millers (e.g. the Fritsch P6), which is the one provided by manufacturers [60]. In this picture, each ball rotates with the sides of the pot until the relative motion of the disk and pot force the ball to fly across the pot, colliding with the side at right angles. Although early computational models [61] supported this view, later analysis of high speed video footage [59] of balls in a Fritsch P7 planetary ball miller (Figure 5.8) show

that there is a high degree of slip between the balls and the pot sides. It was found that balls are carried round at only 20 % of the speed of the pot sides, meaning that balls spend a majority of the time rolling and grinding against the sides of the pot, with relatively infrequent collisions and very little contact with the central area of the bottom of the pot. This is supported by the wear patterns on the insides of the pots in this work (Figure 5.6). Yield at milling speeds below 300 rpm in copper, niobium or titanium was never more than 40 % (Table 5.1), suggesting that at low speeds, the predominant rolling action of the balls allows powder to build up on the sides, with little wear or collisions to break up the agglomerated sample. Higher Fritsch milling speeds produce greater contamination, so the main effect of increasing miller speed is to increase wear between the milling balls and pot sides, with the hard coating of Nb_3Sn particles acting as an abrasive. At all speeds, the Fritsch miller allows powder to cake at the bottom of the pot, and as the balls do not touch the central region, there are no collisions or wear to prevent powder becoming caked there. Work by Mio et al. [62] suggested that changing the miller speed will not substantially change the milling ball trajectories, but that instead the ratio of the speed at which the pot turns to the speed at which the pot station orbits is the critical factor in determining ball motion, and an equation for the optimum ratio (when the most cascading motion occurs) is derived:

$$r_C = \sqrt{\frac{R}{l_C} - 1} \tag{5.3.1}$$

where r_C is the optimum ratio of pot rotation to pot station orbit, R is the distance from the pot centre to the centre of the orbit and l_C is the distance from the centre of a milling ball at the edge of the pot to the centre of the pot. These lengths in the Fritsch P6 miller correspond to an optimum ratio of speeds of ~1.2, significantly different from the actual ratio of speeds of 0.8. Unfortunately, this ratio is fixed in the Fritsch P6, so the balance

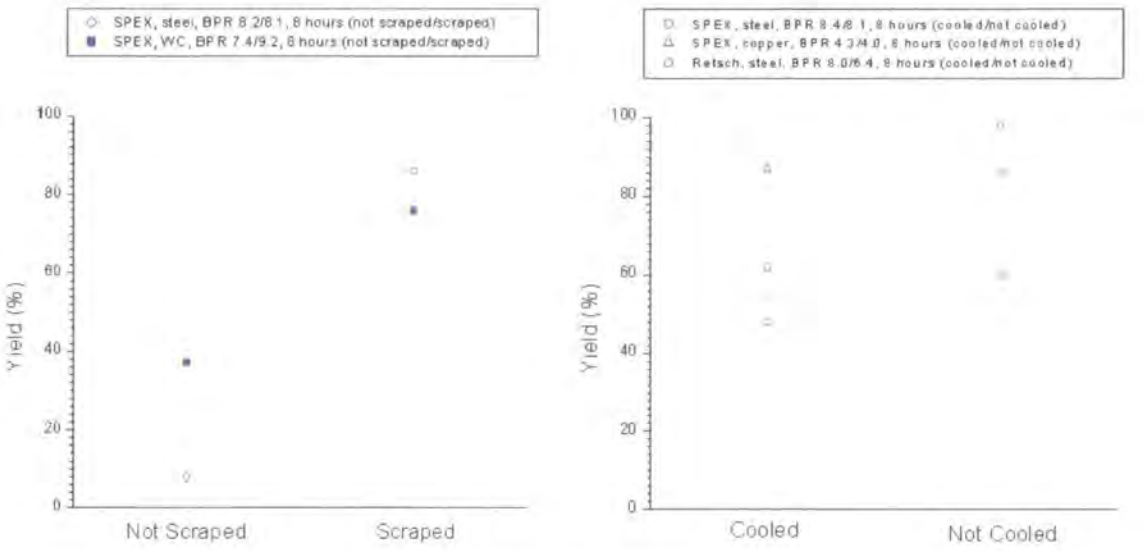

Figure 5.9 A comparison of yields in particular conditions: with and without scraping every 30 minutes (left); and with and without liquid nitrogen cooling (right).

between grinding and impacts could not be adjusted without substantially altering the pot design.

In contrast to the Fritsch miller, according to modelling in the literature [63-66], the shaking actions of the SPEX 8000D and Retsch MM301 millers mean that balls move along more chaotic trajectories, resulting in a much greater proportion of head-on collisions over rolling and wear. It could be seen in this work that the most pronounced collision marks in the SPEX vials were at either end of the cylindrical vial. It is likely that this prevalence of energetic impacts in the SPEX miller, over the Fritsch's rolling and grinding action, helps to increase yield, and also results in a reduction in contamination (Section 5.3.3). The effect of milling parameters on yields achieved in the SPEX and Retsch millers will now be discussed.

The similarity of the vials used in the Retsch MM301 and the SPEX 8000D allowed a more systematic comparison to be made of the effect on yield of cooling, scraping, milling medium and miller (Table 5.2). As concluded for the Fritsch miller, powder

coating of milling surfaces can have a significant impact on yield. It is therefore unsurprising that, of the parameters varied, scraping the powder off the sides of the milling vial regularly produced the clearest improvement in yield (Figure 5.9), and has been used in previous work [56]. The simplest effect of scraping is likely to be by re-introducing powder loosely coating the sides back into the milling process before it becomes compacted on the pot wall. Reducing this Nb_3Sn coating may also reduce the chemical affinity between pot and powder and thereby decrease further agglomeration. Some scraping was done for the Fritsch miller, but not every 30 minutes, as the milling times for adequate microstructural change were longer for the Fritsch miller, and the process of putting Fritsch milling pots into the glove-box is more time-consuming, so scraping the pot this regularly would have tripled the time taken for milling. Takacs et al. reported a problem of malleable zinc powder agglomerating in the corners of the pot when milling in a SPEX miller, and used mixed sizes of milling balls to stop this happening [67]. As copper, niobium and titanium Fritsch milling media were specially manufactured for this work, it was sensible to use this strategy, and Fritsch milling in these media was carried out with equal numbers of balls of 10 and 20 mm diameter (the only commercial agate balls available were ~15 mm diameter). Mixed ball sizes might make tracking (balls repeatedly following the same trajectory) less likely, and small balls may help to break up compacted powder, but as no data with balls of the same size were taken for comparison, this cannot be confirmed. The strategy was not used in the SPEX and Retsch millers, as they have higher yields and more chaotic milling actions anyway.

Milling in SPEX and Retsch millers was carried out in steel, copper and tungsten carbide milling media. Yields were generally high for all these media, except in the cases when scraping was not used (Tables 5.1 and 5.2). The small scale of the differences in yield between milling media of very different hardness (at least 3.0 – 8.0 on the Mohs scale, Table 5.4) for the SPEX and Retsch millers in comparison to the large differences

found between milling media for the Fritsch planetary mill provides further evidence that the shaking action is much less prone to agglomeration problems than the planetary action. Although cooling with liquid nitrogen was tried primarily for possible microstructural change effects (see Section 5.3.4), cooling might also be expected to increase the hardness of the milling media and thereby affect the yield, but there is not enough evidence in this work of a systematic impact (Figure 5.9).

It should be mentioned that the conventional solution to low yields is to use a Process Control Agent (PCA), but as will be discussed further in the next section, ordinary PCAs can introduce significant carbon, oxygen and hydrogen contamination. The possibility of using liquid argon [68] as a means of controlling agglomeration was explored, but this would have required a complete redesign of milling equipment with no guarantee of success. In this section, it has been shown that using a shaker miller, increasing the hardness of the milling medium and regularly scraping the powder coating from the pot sides can be used to produce high yields, so there seemed no reason to compromise sample purity unnecessarily by using PCAs.

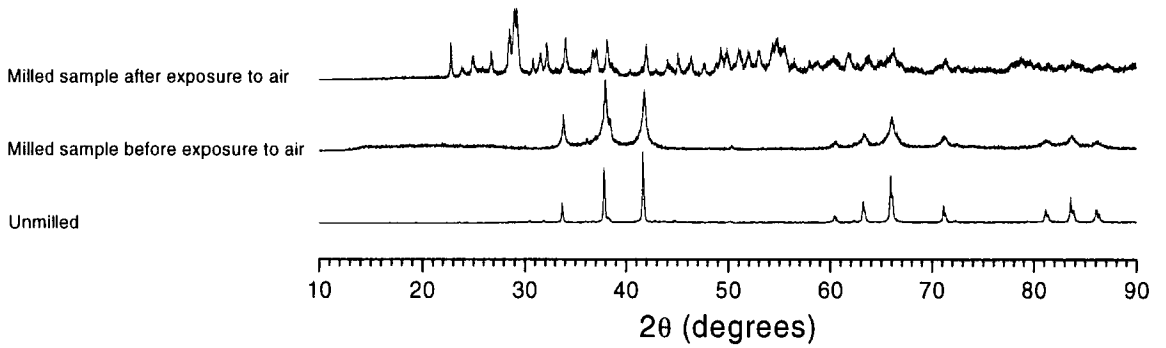

Figure 5.10 XRD spectrum of Nb_3Sn milled for 8 hours in a Retsch miller in steel, before and after exposure to air. In this case, ball milling in an argon atmosphere created unusually small particle sizes which were pyrophoric on exposure to air, forming oxide and nitride phases. Phases identified (using peak-fit software with a database of spectra) include $SnNb_2O_6$ (principal peaks: 25°, 28.8°, 29.1°, 31.4°, 49.1°), SnO (30.8°, 32.2°, 34.1°), SnO_2 (26.8°, 34.1°, 55°, 51.9°), Nb_2N (34.1°, 38.5°, 60.7°, 66.8°), Nb_5N_6 (38.8°, 43.6°, 62.0°) and NbO (37.0°, 43.0°).

5.3.3 Contamination

The pre-alloyed Nb_3Sn powder used in this work was a bespoke alloy of 99.9 wt. % (metals basis) starting purity with a particle size of < 250 μm, obtained from Goodfellow Ltd. in the UK (Table 5.3). Contamination is introduced during ball milling in three ways: reaction with the milling atmosphere, any Process Control Agents (PCAs) used and wear of the milling pot and balls. In this section, varying milling parameters in order to minimise each of these three sources will be discussed. ICP-MS (Section 3.4) and XRD (Section 3.3) have been used to determine contamination levels.

Reaction with the milling atmosphere is the source most easily dealt with. The way particles are constantly cold welded and fractured to expose fresh atomic surfaces means that samples are particularly susceptible to nitride and oxide contamination during milling [24]. In all work in this thesis, milling was carried out in an inert argon atmosphere (minimum 99.998 % purity), by sealing the milling pot in an argon glove-box, using an o-ring on lids which were then screwed down on to the pot. Any work with milled powders was then carried out in the glove-box. There is the provision in Durham to run the Fritsch millers in a secondary argon atmosphere, but as there is no evidence to suggest that the primary pot seal ever failed, and the process typically doubled the time taken for milling, this secondary atmosphere was only used for the agate and niobium-milling. Although oxidation and nitrogenisation during ball milling in air is frequently reported in the literature [28, 69], there is limited evidence for it during Nb_3Sn milling [70]. However, in this work, some milled Nb_3Sn samples were pyrophoric and burned red-hot on exposure to air, emphasizing the importance of using an inert milling environment. Figure 5.10 shows XRD spectra of one of the pyrophoric samples (Nb_3Sn milled in the Retsch miller with steel media for 8 hours) before and after exposure to air. This shows that if powders are fine enough, Nb_3Sn can react with air to form a complex mixture of oxides and nitrides of tin and niobium. It should be noted that before exposure

to air, there is no evidence of nitride or oxide formation, although the insensitivity of XRD to amorphous phases means the presence of oxygen or nitrogen cannot be completely discounted. However, given that powders were kept in a high purity argon atmosphere at all times, it seems reasonable to assume that oxidation and nitrogenisation are very limited prior to air exposure. The milled powders consolidated to form bulk superconducting samples (Chapter 6) were milled in niobium under primary and secondary argon atmospheres to minimise the risk of air contamination as far as reasonably practicable. As will be outlined in the next chapter, procedures were also developed in this work which ensured that after milling, powders were not exposed to air until after they had been consolidated into a bulk sample by Hot Isostatic Pressing (HIP'ing). Even after heat treatment up to 850 ^{o}C, no additional oxide or nitride peaks were discernable in the XRD spectrum (Figure 6.3 in Chapter 6), so there is no evidence to suggest that the precautions taken to avoid oxide or nitride formation were not successful. Unfortunately, there are no facilities in Durham for the determination of oxygen or nitrogen levels, as ICP-MS analysis cannot be used to measure gaseous elements directly. Thermogravimetric reduction and wet chemical analysis have been used to determine oxygen contents in high temperature oxide superconductors [71], but these methods have not been adapted for Nb_3Sn, meaning that experimental technique and error determination would constitute new work. Alternatively, an Energy Dispersive X-ray (EDX) detector on a Scanning Electron Microscope (SEM) with the capability for light-element analysis could be used to provide local measurements, and might be more sensitive to amorphous phases than X-ray or neutron diffraction. Analysis of nitrogen and oxygen would be most accurate using an inert-gas fusion instrument suited for refractory compound work, such as the Eltra ON900 [72] or the Leco TC600 [73]. The rate at which oxygen and nitrogen are given off and detected using these instruments as a function of temperature could also give some information about the position of the gases

in the sample. Any technique used would ideally enable analysis to be done without exposure to air, which is possible for X-ray diffraction, but may be more difficult for other techniques. Given the care taken to avoid oxygen contamination, the lack of evidence in the literature for oxygen having a positive effect on $B_{C2}(0)$, and the absence of oxide peaks in XRD spectra of milled samples, no further work has been done to more accurately quantify oxygen levels.

PCAs are a common source of contamination mentioned in the literature. They are liquid surfactants added to powders during milling in order to decrease particle size and increase yield [56, 74-78] by reducing the surface energy of the particles in the miller and forming a physical barrier to cold welding. They are typically polar organic molecules containing oxygen (e.g. stearic acid, ethyl acetate, ethylenebidisteramide, methyl alcohol, ethyl alcohol or polyethylene glycol), although non-polar hydrocarbons can be used if oxygen contamination is a particular concern (e.g. hexane, heptane, dodecane, cyclohexane or benzene). Optimum levels of PCA are around ~3 % [24, 75], but as these molecules decompose during milling and typically need to be replenished, their use can introduce significant (e.g. 12 wt % carbon) contamination, particularly at grain boundaries [79, 80]. As mentioned in the previous section, the use of liquid argon as an inert PCA was investigated for this work, but not pursued due to lack of evidence about argon's properties as a surfactant, the need to redesign milling equipment, practicalities of how to ensure an argon atmosphere above the liquid, and the possible effects low temperatures might have on miller mechanisms such as the Fritsch P6. PCAs have therefore not been used in this work, and so contamination from this source has been eliminated.

Milling atmosphere and PCAs have been discounted as significant sources of contamination, leaving only milling media wear. As mentioned in the previous section, unconventional milling media were used in an attempt to limit the impact of

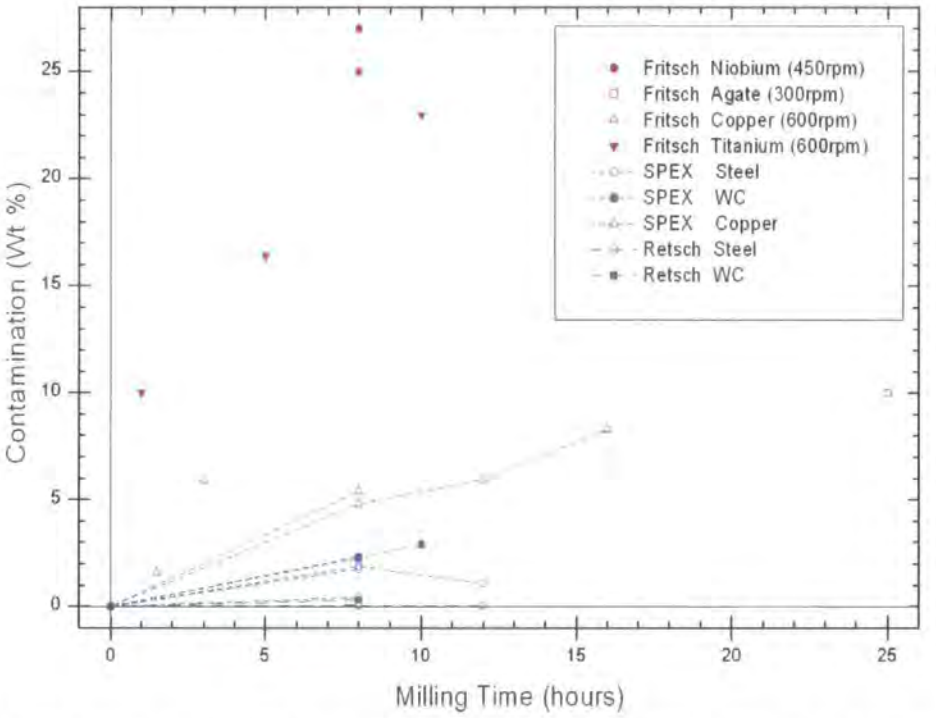

Figure 5.11 Data on the effect of miller, milling medium and speed on the rate at which contamination is introduced during milling. ICP-MS measurements made by C J Ottley.

contamination on the superconducting properties. This involved sourcing and manufacturing novel high purity niobium, copper and titanium milling tools. As detailed in Table 5.3: the niobium was of 99.95 % purity; the copper used was 99.95 % C103 grade; and the titanium was 99.8 % grade 2. Levels of oxygen and magnetic impurities were low for all these materials (Table 5.3). As found in the previous section, the Fritsch's planetary action has very different effects to the shaking actions of the SPEX and Retsch millers, so contamination data for the Fritsch miller will again be presented first.

In the case of milling in the Fritsch P6 miller: Figure 5.11 shows that agate, the hardest (most wear-resistant) medium, introduced contamination at the lowest rate (~0.3 % per hour of milling). This figure also shows that the soft milling media (copper, niobium and titanium) all introduce contamination at a rate of ~3 % per hour of milling. This high rate makes drawing firm conclusions about which of these softer media

introduces contamination slowest irrelevant – only niobium contamination at these levels can be tolerated whilst still retaining confidence in the superconducting properties of the resulting sample. As outlined in Chapter 6, although not ideal, any additional niobium introduced from the pot can be corrected for by adding extra tin prior to consolidation. As was seen in Section 5.3.2, there is evidence in the literature that milling ball trajectories do not change significantly with milling speed and that the Fritsch milling action involves a high proportion of wear and friction, implying that higher milling speeds will result in higher contamination rates. The qualitative XRD spectra, limited quantitative ICP-MS data, and yields being above 100 % at high milling speeds appear to support this, although the link is not conclusive. The effect that milling tools becoming coated had on yield is clearer. XRD spectra (Figure 5.1) and yield data (Table 5.1) from niobium milled at 300 rpm show a large increase in niobium contamination, under otherwise identical milling conditions, when the pot became coated and the distinct boundaries between milling tools and powder were blurred. Therefore, as well as being important for consistent yields (5.3.2), maintaining clean milling surfaces may help to reduce contamination in the Fritsch miller by reducing abrasive wear. Regular scraping to remove powder coating, as well as occasionally re-machining the milling surfaces to remove the Nb_3Sn layer could therefore result in lower contamination rates.

The rate of introduction of contamination in the shaker SPEX and Retsch millers is much lower than in the planetary Fritsch miller (Figure 5.11). The highest contamination rate in the SPEX miller is for the softest medium, copper, but even this is only ~0.5 % per hour of milling - comparable to agate, the hardest milling medium, in the Fritsch miller. The lowest contamination rates in the SPEX miller were ~0.25 % per hour for tungsten carbide and steel which may be due to higher hardness values over copper (Table 5.4). Contamination in the Retsch miller is negligible (<0.01 % per hour) and, as will be discussed in Section 5.3.4, Scherrer grain sizes for the Retsch-milled samples are

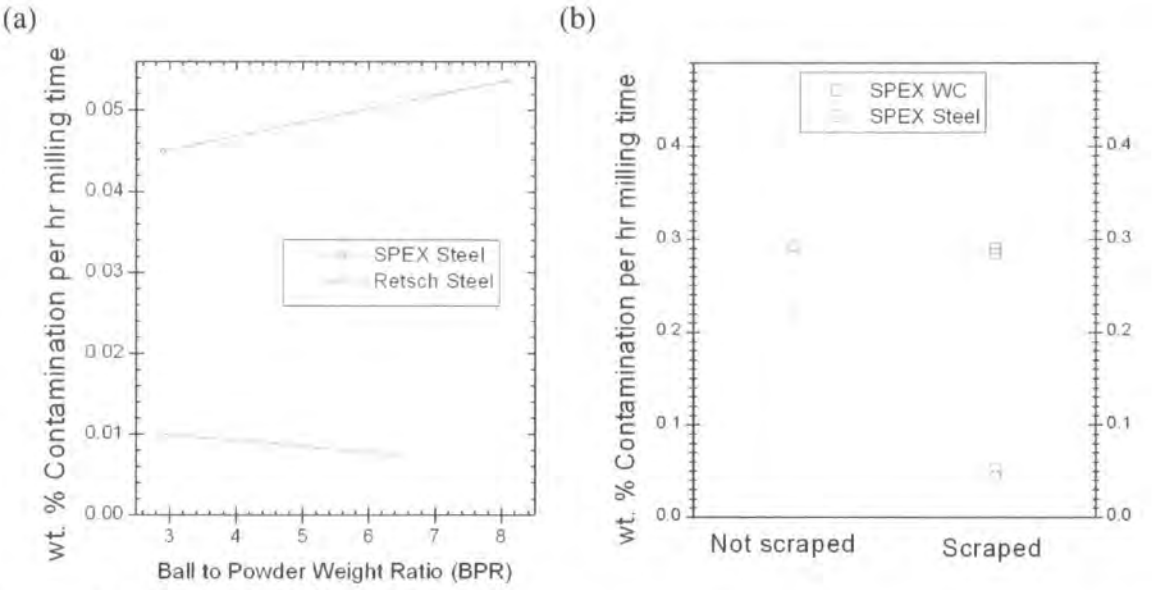

Figure 5.12 (a) The effect of Ball to Powder weight Ratio (BPR) on the rate at which contamination is introduced during milling in the SPEX and Retsch millers in steel milling media. (b) Data showing the effect of scraping and cooling on the contamination introduced by milling in SPEX and Retsch millers. ICP-MS measurements made by C J Ottley.

comparable to the best from the Fritsch miller, making the Retsch MM301 an attractive alternative to the Fritsch P6. The SPEX miller introduces more contamination than the Retsch miller, but as will be seen in the next section, this is counterbalanced by the large increase in microstructural disorder, which represents a sea change from either the Retsch or Fritsch machines. The effect of Ball to Powder weight Ratio (BPR) on the rate of introduction of contamination (in otherwise identical conditions) was investigated for the SPEX and Retsch millers with steel milling media. Figure 5.12a shows that doubling the BPR has no significant effect on contamination. It is also important to note that, from the limited data available (Figure 5.12b), there is no evidence that scraping increases contamination from the milling media. These results are particularly positive in the case of increasing BPR and scraping, as these factors can increase the rate of microstructural change introduced by milling, as will be seen in the next section.

5.3.4 Microstructural change

The motivation of ball milling is to induce microstructural change, and although yield and contamination are important factors, if the right changes are not produced, then milling cannot be considered to have been successful. The overall aim of this work was to produce bulk Nb_3Sn with an average crystallite size similar to (or lower than) that of commercial superconducting wires (~100 nm [36]). Heat treatment of milled powder is necessary for producing non-porous bulk samples, and as this will inevitably result in some recrystallisation, the focus of ball milling was simply to reduce crystallite size as far as possible. In the most successful work on improving superconducting properties in the chevrel-phase superconductor PMS [3], ball milling was used to produce a mixed amorphous and nanocrystalline microstructure with a high degree of disorder [81]. Therefore in this work, XRD peak broadening has been used to track the level of microstructural change. As explained in Section 3.3, XRD does not yield information about the minutiae of exactly what kinds of microstructural disorder are introduced by ball milling, but it does offer a simple way of gauging the energy of disorder stored in a system, and so more detailed characterisation is not necessary for the overall aims of this work. Transmission Electron Microscopy (TEM) could be used to yield information about disorder such as dislocations and grain boundaries [82], but thin (~1 μm) sample sections would be need to be prepared (whilst avoiding alterations to the microstructure in the process), which would probably restrict such TEM studies to bulk (HIP'ed) Nb_3Sn samples unrepresentative of as-milled powder. However, it is interesting to note work done by other groups in this area.

Analogies are often made in the literature between disorder introduced by quenching, neutron irradiation and ball milling [83-85]. These comparisons can yield useful information, but the different mechanisms involved in these processes mean that

conclusions drawn from such analogies must be treated with some caution. Quenching is relatively well understood [47] as a means of preventing normal phase changes from occurring during cooling by shortening the period of time when the phase change is both kinematically and thermodynamically possible (e.g. close to the phase boundary) to such an extent that the phase change does not go to completion, resulting in the retention of a metastable state at (for instance) room temperature. In simple terms, the mechanisms involved in quenching are thermodynamic excitation and relaxation. In comparison, the mechanisms during ball milling and neutron irradiation involve the continuous addition of disorder (from collisions with milling balls and atoms being knocked out of position

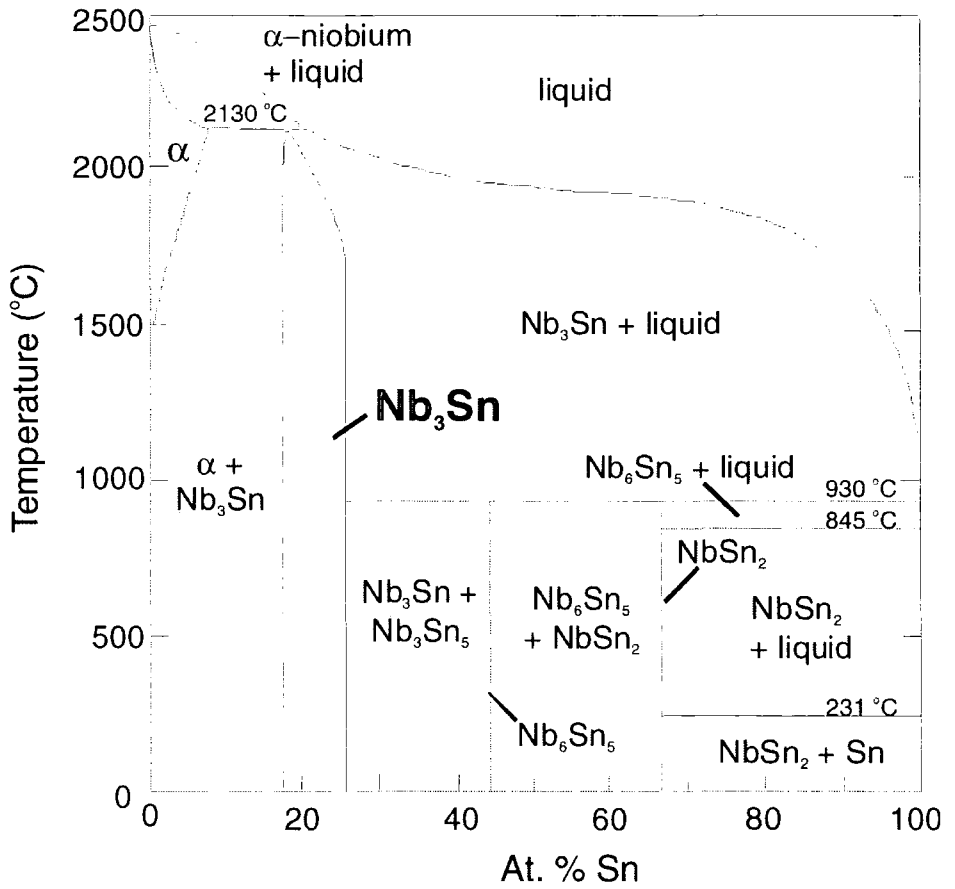

Figure 5.13 Phase diagram for the binary Nb-Sn system at high temperature (> 0 °C), adapted from Miyazaki et al. [86].

by neutrons) in addition to the normal thermal processes. Thus the system will tend towards a state of dynamic equilibrium, and if the disorder introduced dominates thermal effects, the system will be left in a metastable state when the milling or irradiation stops. This means that ordinary (thermodynamic) equilibrium phase diagrams (Figure 5.13) must be abandoned in favour of the concept of (dynamic) non-equilibrium phase diagrams [87]. Unfortunately, no non-equilibrium phase diagrams have been characterised for Nb_3Sn, and even if they had, it is unlikely that such a phase diagram defined for one source of disorder (e.g. neutron irradiation) could be used to reliably predict the stable phase due to another (e.g. ball milling), as the type of disorder introduced would vary. There is also evidence to suggest that altering milling parameters not only changes the rate at which disorder is introduced, but may also affect the proportions of different types of disorder [24]. Therefore, comprehensive characterisation of such non-equilibrium phase diagrams would only offer accurate information for the particular milling or irradiation parameters used. Despite this lengthy disclaimer, it is still enlightening to look at the general form of such diagrams and the types of disorder likely to dominate when milling Nb_3Sn.

It has often been claimed that atomic (chemical) disorder in Nb_3Sn introduced by ball milling is anti-site disorder [83, 84], and that the number of vacancies is very small [85]. The evidence for this is based on close correspondence between the form of the relationship between T_c and milling time for Nb_3Sn with the form of the same relationship in similar A15 materials on which characterisation and simulations have been more comprehensive. Modelling the effect of anti-site disorder would have on the lattice parameter and T_c of Nb_3Sn fits experimental data for Nb_3Sn disordered with milling, neutron irradiation and quenching. Therefore the suggestion that anti-site disorder predominates over vacancies when milling Nb_3Sn seems reasonable. However,

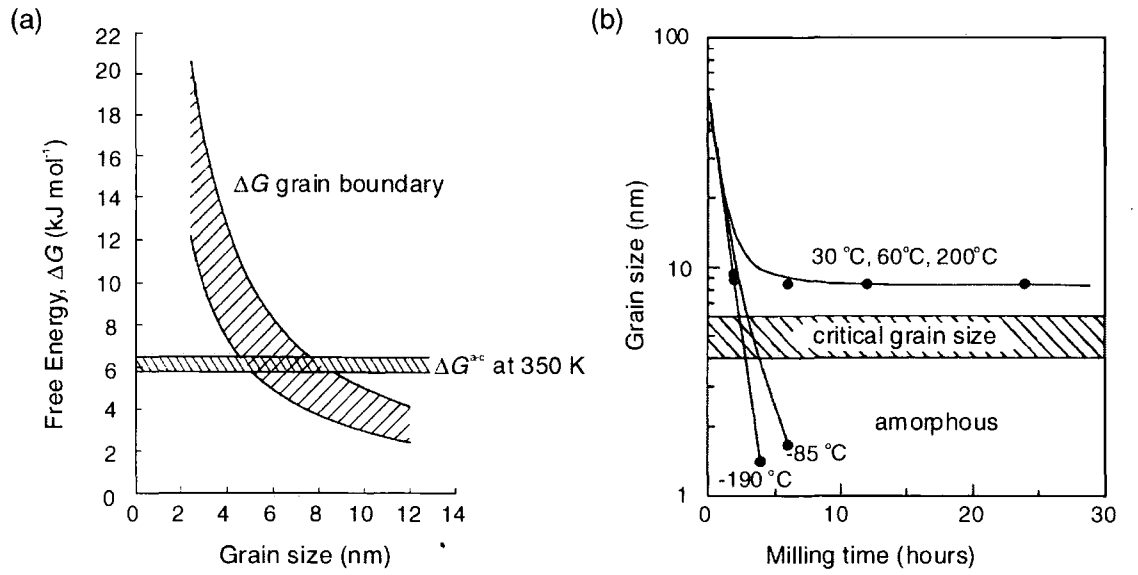

Figure 5.14 (a) Data for the intermetallic CoZr (adapted from Cho et al. [88]), showing that grain boundary energy can exceed the free energy difference between crystalline and amorphous states, and so could drive this phase change. (b) Data from milling CoZr (figure adapted from Suryanarayana [24]), showing the effect of milling temperature on the minimum grain size achieved, and a suggested "critical grain size" above which the crystalline-amorphous phase transition cannot occur.

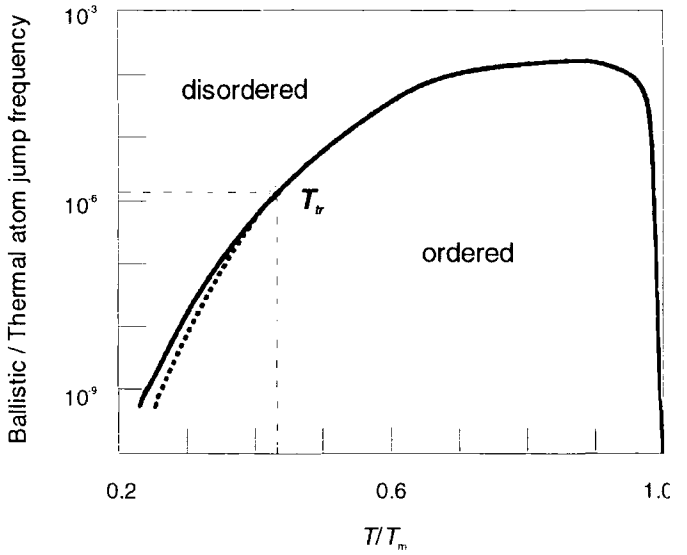

Figure 5.15 A computed non-equilibrium phase diagram (adapted from Bellon et al. [87]) for a material in terms of the rate of introduction of disorder (ratio of ballistic to thermal atom jumps) and the partial temperature, T/T_m. A point is marked, T_{tr}, above which the phase boundary changes from being a second- to a first-order phase transition.

the contribution of other types of disorder such as grain boundaries and dislocations has often been ignored, perhaps because these types of disorder are rarely formed by neutron irradiation. Close correspondence between computations of T_c assuming anti-site disorder and experimental evidence of the effect of milling time on T_c does not prove that anti-site disorder is the most significant form of disorder introduced by milling: grain size reductions and dislocations may not have a large effect on the value of T_c, but that does not mean that they are an energetically insignificant factor in the crystalline-amorphous phase change for example. Grain boundary energy has been found to be the critical factor in amorphisation in other materials [88], and the fact that Scherrer grain sizes of milled Nb_3Sn have been reduced to sub-10 nm levels before becoming X-Ray amorphous (this work, [27]), suggests that grain boundary energy is a potentially important factor. Work by Cho and Koch [27] estimated the difference in free energy between amorphous and crystalline Nb_3Sn at 300 K to be ~15 kJ mol^{-1} (half the enthalpy of fusion), so energy of this order must be introduced to create amorphous Nb_3Sn. Comparison with similar materials suggests that the energy associated with anti-site disorder in Nb_3Sn (the ordering enthalpy) is likely to be only ~5 kJ mol^{-1}, and so an additional energy of ~10 kJ mol^{-1} is needed to drive the phase change. A simplified calculation suggests that this energy would be provided by a reduction in grain size to ~7 nm (a grain boundary energy of ~500 mJ m^{-2} is assumed as no figures are available for Nb_3Sn). This is clearly not an exact calculation, but it seems reasonable to conclude that a combination of the energies associated with anti-site and grain boundary disorder drove milled Nb_3Sn to transform into an XRD-amorphous phase in this and other work [27, 28] and that of these, grain boundary energy is likely to be the dominant factor. More accurate free energy data exist for the intermetallic CoZr (Figure 5.14a), confirming that grain boundary energy can exceed the free-energy difference between crystalline and amorphous states if grain size is reduced below a critical level (Figure 5.14b).

Non-equilibrium phase diagrams have been modelled by Bellon et al. [87] for irradiation (as well as a simpler calculation by Bakker et al. [84]), and the general form (Figure 5.15) shows a reasonably intuitive relationship between temperature and disorder. Amorphisation, or at least a more disordered state, is stable in two cases: if the temperature is very high (i.e. it melts); or if the rate of disorder is high enough to dominate temperature effects (i.e. irradiation high and temperature low). Such phase diagrams for ball milling may be less straight-forward, as there is greater inter-dependency between grain boundaries, anti-site disorder, temperature and milling power. To elaborate, it may be imagined that if the concentration of grain boundaries increases, a decrease in anti-site disorder due to relaxation in the boundary region may result. It is also unclear what "temperature" means in the context of ball milling: macroscopic temperature rises of ~100 ^{o}C are known to occur during milling [24]; ball temperature rises of ~200 ^{o}C are expected; and microscopic temperature increases in powder trapped in a collision are estimated to be much higher (depending on the volume of powder assumed to be trapped [89]). Clearly, the scale of these temperature increases will vary with milling intensity, but also temperature increases may affect the milling power through changes in the properties of the milling medium and through variations in the way the powder coats the milling tools. Milling ball motion not only varies between milling machines but may also be different in a particular miller at different speeds, resulting in changes in the type of disorder introduced, and meaning that milling power is a less well-defined quantity than irradiation. Lastly, it is important to remember that as with any other phase diagram, the non-equilibrium phase diagram will only give information about the most stable phase under particular conditions, and nothing about the rate at which the phase will be reached, or indeed if a metastable phase could be formed instead. In summary, the milling power-temperature parameterisation implied by

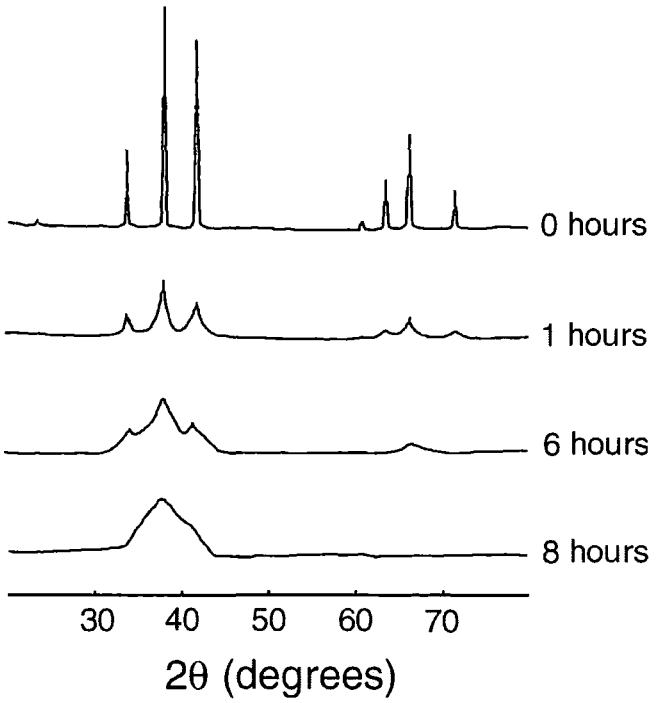

Figure 5.16 Data adapted from a paper by Cho et al. [27] showing the change in the XRD spectrum of Nb_3Sn with milling time. A SPEX 8000 miller was used with steel milling media. Long- range order has been destroyed, as shown in the single broad peak after 8 hours.

irradiation phase diagrams (Figure 5.15) is a useful concept, but it should be borne in mind that this simple picture is unlikely to be accurate.

Throughout the above discussion, it has been tacitly accepted that the disordered state which the milled powder changes into is an amorphous one. This has been found to be the case in Nb_3Sn in previous work [27], but this is not always true: Nb_3Al and Nb_3Au transform into bcc solid solutions for example [90, 91]. It has been suggested [24] that the phase which forms on raising the temperature can be used to predict the phase which forms if enough disorder is introduced by milling (an amorphous structure being considered to be the same as a liquid). It can be seen from Figure 5.13 that Nb_3Sn transforms to a mixture of liquid and Nb_3Sn at high temperature, equivalent to a mixed amorphous and nanocrystalline phase on milling. XRD data from this work (Figure 5.1 and Figure 5.2) and by other groups (Figure 5.16) show that Nb_3Sn has first been made

nanocrystalline and subsequently X-ray amorphous (in some cases). The "X-ray amorphous" state is likely to be a mixed amorphous and nanocrystalline phase which, by the above rule-of-thumb, may well be the final stable state possible from milling. Following the above discussion, it will be assumed that grain boundary energy is a significant factor in the amorphisation process, and that the formation of a nanocrystalline structure with a critically small grain size is a prerequisite to amorphisation. As discussed in Section 3.3, XRD peaks are broadened by both microstrain and crystallite-size-reduction. In this work, both broadening effects will be considered to be two aspects of disorder energy: microstrain is associated with grain boundaries (and therefore grain boundary energy) and atomic disorder (with its associated disorder energy); and crystallite-size reduction is clearly associated with an increase in grain boundary energy. This means that the effect of different milling parameters varied in this work can be directly compared through peak broadening in XRD spectra.

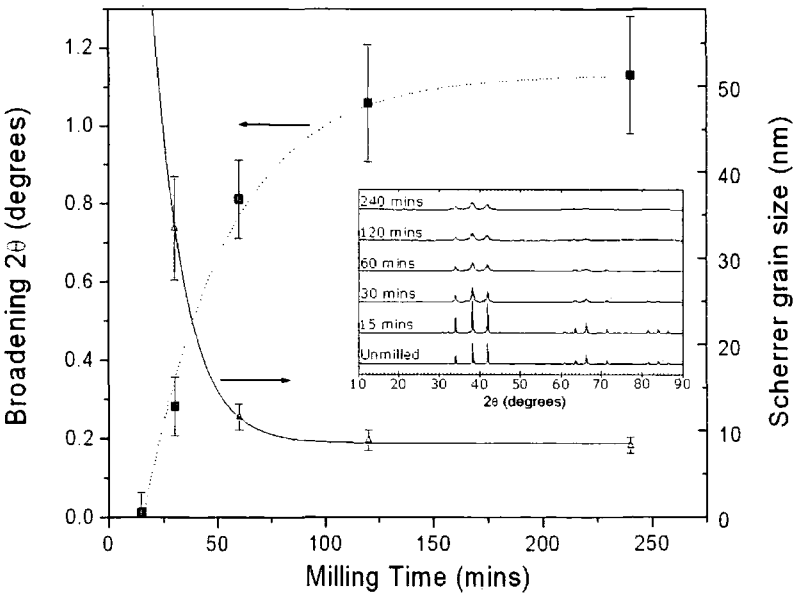

Figure 5.17 Grain size change with time as Nb_3Sn is milled (Fritsch miller, Nb milling media), showing that grain size reaches an equilibrium after a certain time after which no further reductions are achieved. **Inset**: XRD spectra used to calculate grain sizes (Scherrer analysis).

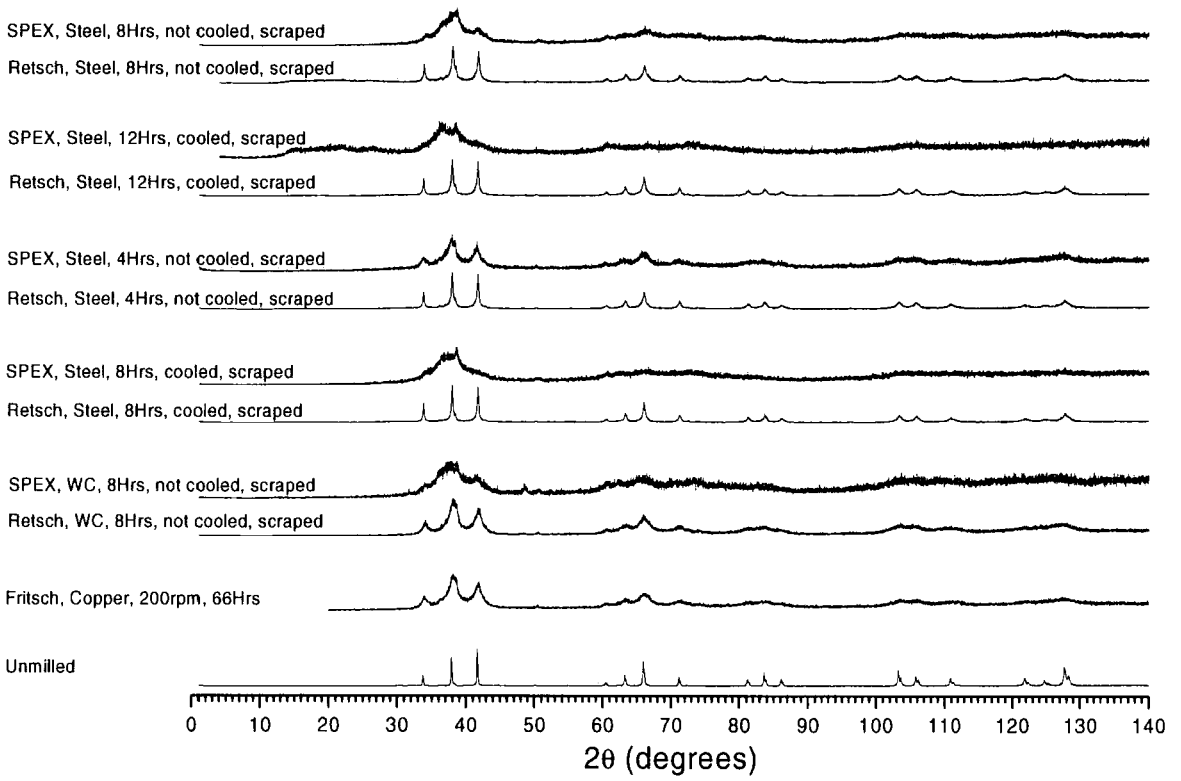

Figure 5.18 Comparison between SPEX 8000D and Retsch MM301 millers in similar conditions

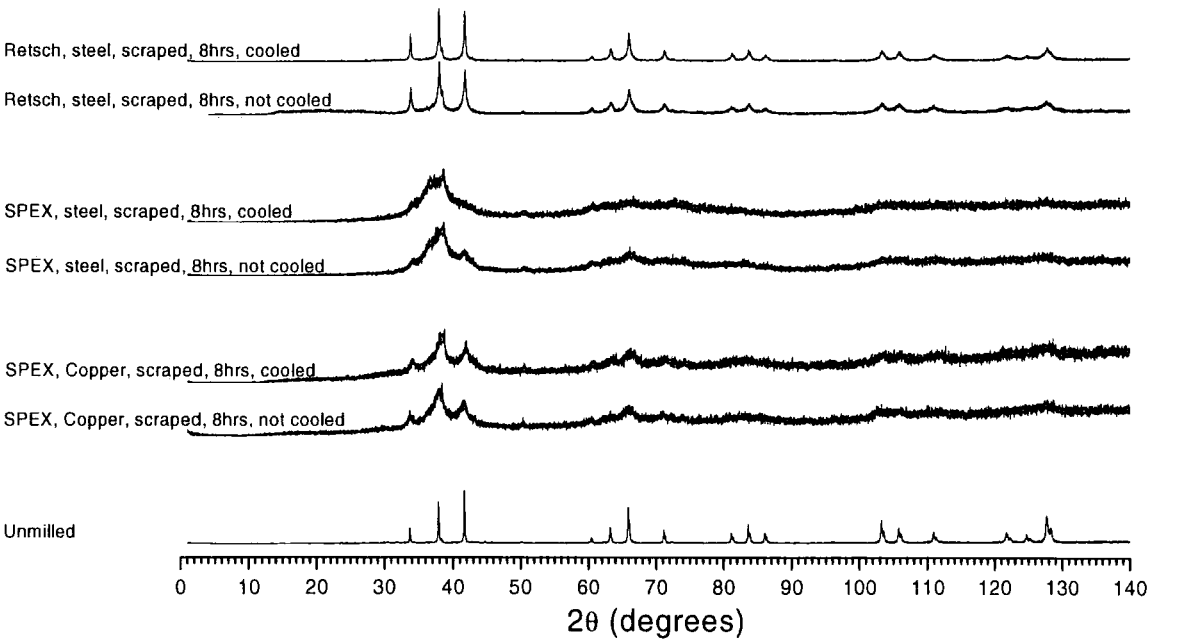

Figure 5.19 Data showing the effect of cooling using liquid nitrogen on the microstructural change produced under otherwise similar milling conditions.

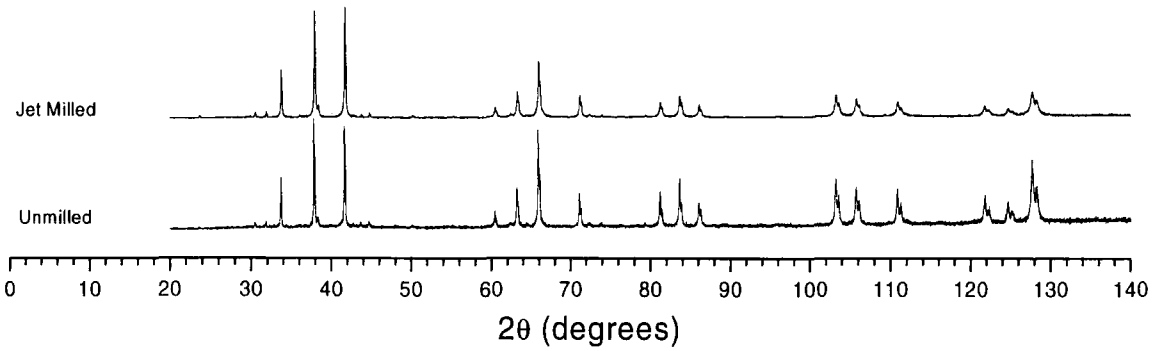

Figure 5.20 XRD spectrum of Nb_3Sn before and after jet milling. The jet milling was done in a Hosokawa 100AS jet miller by M Ghadiri's group at Leeds University, UK. Virtually no microstructural change has occurred.

As might be imagined from the description of milling as a non-equilibrium phase diagram, there is a certain milling time required before a dynamic equilibrium of disorder introduction and thermal relaxation is reached. If a phase change has not occurred by the time this equilibrium state is reached, then it will not happen unless the milling conditions or chemical composition (e.g. by the introduction of contamination) are altered. The exponential decrease in grain size (to a constant value) with milling time seen in this work (Figure 5.17) is typical of data in the literature. It is usual to stop milling once the steady state regime is reached, in order to minimise contamination.

The parameter with the clearest effect in this work is the milling machine. Four different milling machines have been used in this work: the Fritsch P6, Retsch MM301, SPEX 8000D and the Hosokawa 100AS jet miller. The jet miller ejects powder when the particle size drops below a certain size, and at this stage no noticeable change in microstructure had occurred (Figure 5.20). As ejection precludes further jet-milling, this was not investigated further. Of the other millers, it can be seen from Figure 5.18 that despite varying other milling parameters (Table 5.1), the widest XRD peaks achieved in the planetary Fritsch miller are about as broad as the narrowest achieved in the Retsch and SPEX shaker millers. It can also be seen from Figure 5.18 that under the same milling conditions, the SPEX milled samples were consistently more amorphous than

those from the Retsch miller. As discussed in Sections 5.3.2 and 5.3.3, the motion of the milling balls in the different millers are quite distinct. There is a predominance of rolling and grinding of the milling balls around the sides of the pot over ball-powder-pot collisions in the planetary Fritsch miller. It was shown above that the phase formed in such dynamic equilibrium systems is determined by the rate at which disorder is introduced and the temperature. As there is no evidence to suggest that the temperature reached in the Fritsch miller is substantially different to the other millers, it can be assumed that collisions in the Fritsch miller are too infrequent to reduce the grain size to a low-enough level for amorphisation to occur. As was mentioned previously, the rotational speed of the pot and disk in the Fritsch miller are fixed in an un-optimised ratio, so the frequency of collisions cannot be substantially increased. Modelling of shaker-millers [66] suggests that the power, P, imparted to the powder by shaker millers such as the Retsch MM301, is related to the frequency, f, and amplitude, A, of the action by the expression:

$$P \propto Af^3 \tag{5.3.2}$$

The Retsch has a recommended maximum frequency of 25 Hz and an amplitude of ~30 mm in comparison to 15 Hz (lower than for the same mill operating in the US) and ~60 mm (horizontal amplitude, with 25 mm lateral movement) for the SPEX miller. If the manufacturer data are accurate, and the SPEX motion is assumed to be the same as the Retsch motion, the power introduced by the SPEX miller should be ~half that of the Retsch miller. Therefore the fact that results in this work from the SPEX miller are significantly better than those achieved in the Retsch miller suggest that the more chaotic ball motion introduced by the figure-of-eight motion is more effective than the Retsch's linear action. It seems likely that this must be due in part to higher collision power, although increased sample homogeneity may also play a part if more of the powder

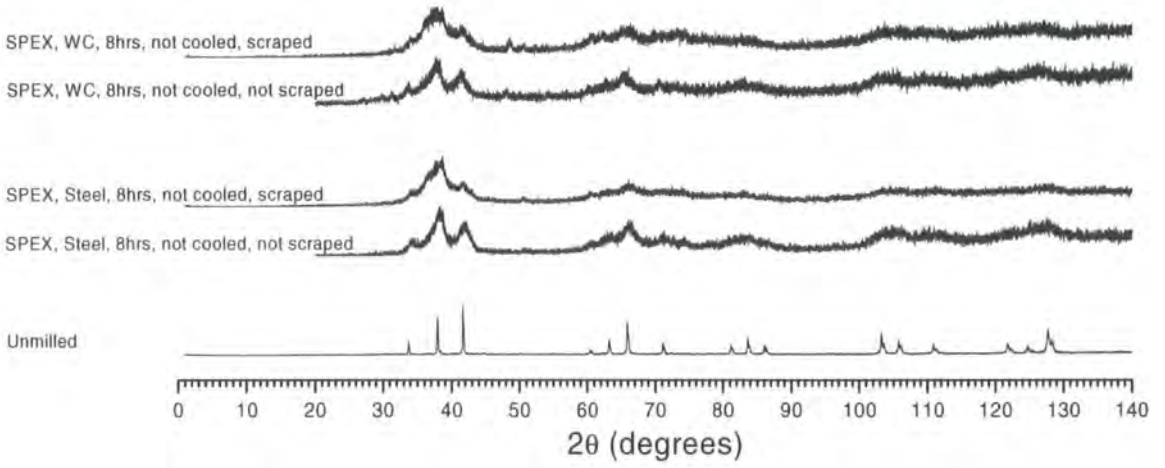

Figure 5.22 XRD spectra showing the effect of scraping the powder off the sides of the pot every 30 minutes during milling on Nb_3Sn samples milled under otherwise similar conditions. Scraping increases the overall microstructural change.

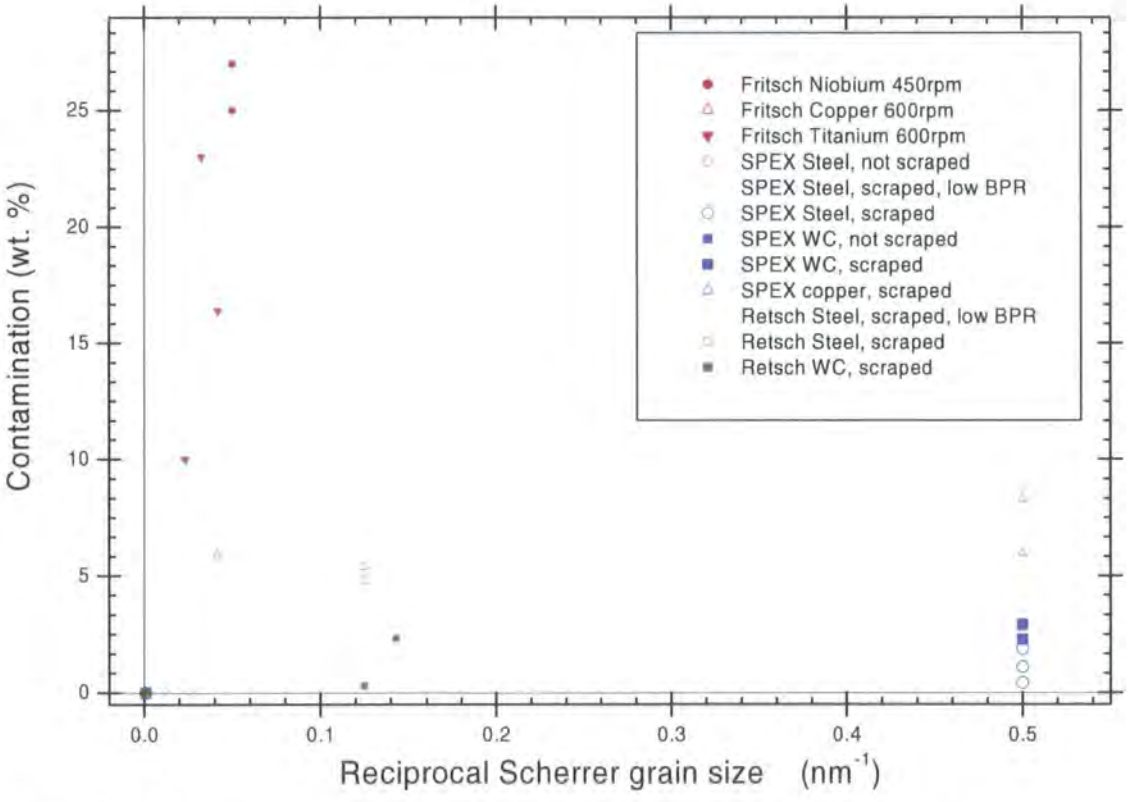

Figure 5.21 Plot of contamination introduced against inverse grain size achieved for a number of samples milled in the Fritsch, SPEX and Retsch millers. Datum points towards the bottom right of the plot have comparatively low contamination for the change in microstructure achieved. X-ray amorphous samples are plotted with an arbitrary grain size of 2 nm.

undergoes continuous collisions due to reduced tracking (balls repeatedly following the same trajectory). As mentioned in Section 5.3.2, mixed ball sizes were used for the Fritsch milling as there was evidence from the literature that this can reduce the powder coating on the balls and thereby increase yield. A computation by Gavrilov et al. [66] on a shaker-mill system (similar to the SPEX and Retsch millers) suggested that mixed ball sizes would increase collision energies, and although there are no directly comparable data from this work to confirm or deny this, it may be a factor worth investigating for the SPEX miller. Greater sample homogeneity is certainly the cause of the large increase in peak broadening when powder is regularly scraped off the sides of the pot during milling (Figure 5.22). This shows that the proportion of powder which becomes coated on the sides or trapped in the corners of the pot during milling can be considerable and that scraping is an effective way of reducing this problem particularly as no increase in contamination was found with scraping (Section 5.3.3).

As discussed above, the simple non-equilibrium phase diagram (Figure 5.15) would imply that amorphous phase formation may be more stable at lower temperatures, as has generally been found in previous work ([92], Figure 5.14b). However, this only means that the amorphous phase is more thermodynamically stable than the disordered crystalline structure, and although more disorder may be built up at reduced temperature, the kinematics of the crystalline-amorphous phase change at low temperature may be slower. Figure 5.19 shows very little difference in the XRD broadening between powder milled for the same time at room temperature in comparison to powder milled in pots pre-cooled in liquid nitrogen every 15 minutes. There are not enough data from this study to draw conclusions about the time-constant of microstructural changes, nor about the level of disorder when the material reaches dynamic equilibrium, so it is impossible to come to conclusions about the effect of temperature on the stability of different phases.

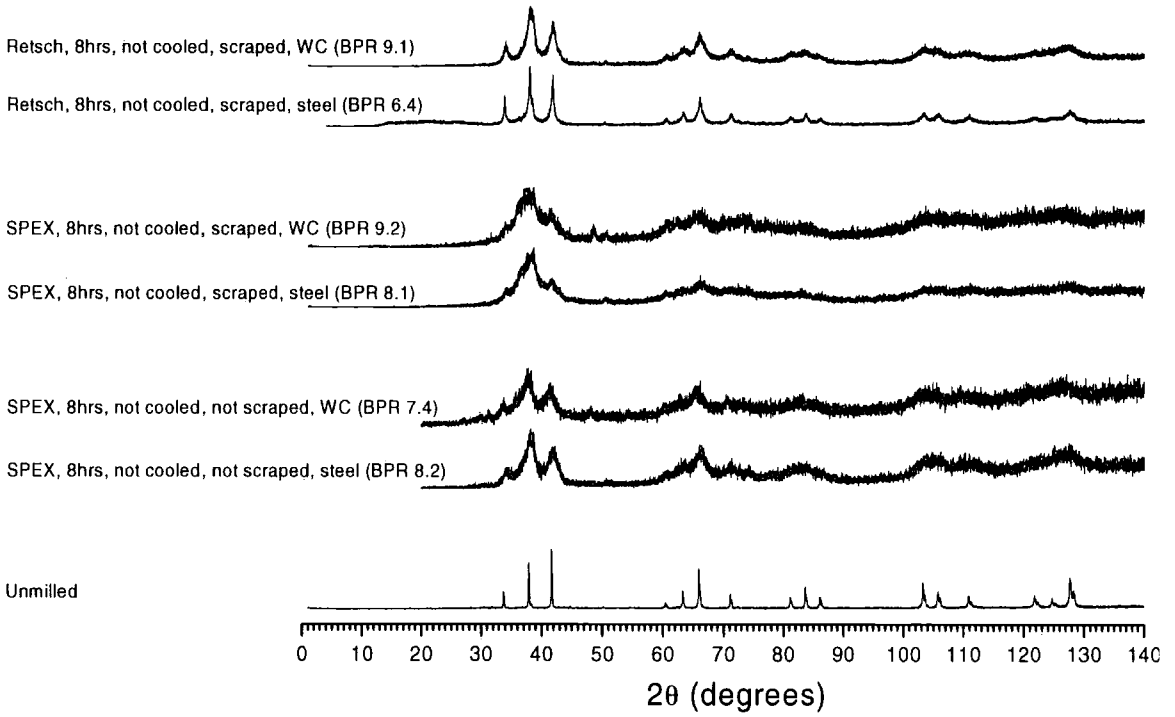

Figure 5.24 Effect of milling medium on microstructural change, showing that a combination of hardness and density differences make tungsten carbide slightly more effective than steel.

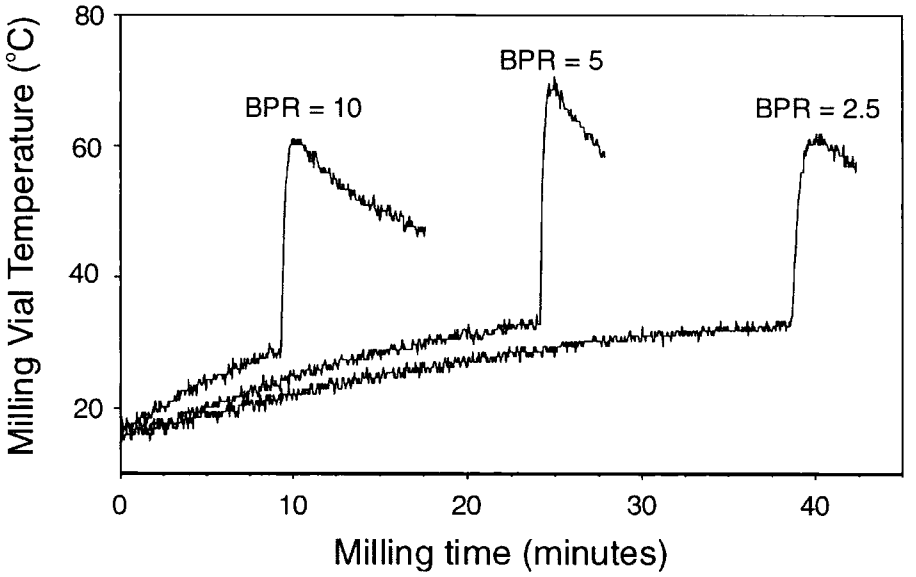

Figure 5.23 Figure from Ward et al. [47, 49, 65] showing the effect of changing the Ball to Powder weight Ratio (BPR) on the rate at which the microstructure changes to a point at which a reaction occurs (the sharp increase in temperature). In general, it can be seen that increasing BPR speeds up the microstructural change considerably, although practically, this will reach a peak due to too little powder or an over-full vial causing a decrease in efficiency.

Given success with cryomilling in previous work [24], it seems reasonable to suggest that cryomilling should be tried if milling at room temperature does not reduce crystallite size sufficiently to drive the crystalline-amorphous phase change. It is interesting to note that although cryomilling reduces average grain sizes, a greater spread in grain size has also been found – TEM data would be required to confirm this in this work. Cryogenic followed by brief room-temperature milling was used by Zhu et al. [93] and Zhang et al. [94] to combine narrow spread of grain sizes with a lower average value.

It was seen in Sections 5.3.2 and 5.3.3 that the hardness of the milling medium had a large effect on yield and contamination. Recent work by Ward et al. [65] showed that surface coating can have a significant effect on the collision energy, and thus milling media hardness is likely to have an effect on microstructure as well. However, the work by Ward also confirmed that BPR is an accurate way to parameterise the rate at which a particular level of disorder is introduced for a particular milling medium (Figure 5.23). The different densities of milling media mean that it is not possible to easily separate the effects of density and hardness on the resulting microstructure. Figure 5.24 shows comparative XRD spectra for powder milled in steel and tungsten carbide with similar BPR ratios in the SPEX and Retsch millers. The data suggest that tungsten carbide is perhaps a slightly more effective milling medium, although the differences involved are small in comparison with the effect of miller and scraping discussed previously. In Section 5.3.3, the effect of milling medium on contamination was discussed, and given the potentially significant impact of contamination on the superconducting properties, it is important to be able to maximise the microstructural change while minimising the contamination. Figure 5.21 shows that miller has a huge impact on this optimisation, with the Fritsch miller giving consistently high contamination coupled with low levels of microstructural disorder. The Retsch shaker mill introduces very little contamination, but the microstructural change induced is not as impressive as that achieved in the SPEX,

which was the only miller to drive Nb_3Sn amorphous. The SPEX miller introduced more contamination than the Retsch miller, but in many conditions, amorphisation had occurred by the time of the shortest milling time tried, so there is likely to be scope for milling time optimisation. Of the milling media successfully used to produce amorphous Nb_3Sn in the SPEX miller, the copper produced the worst contamination, followed by the tungsten carbide, with steel producing the lowest contamination levels. This is unfortunate give the relative effect on superconducting properties these contaminants are likely to have.

Chapter 6

Ball milled samples subsequently HIP'ed

6.1 Introduction

The purpose of the work in this thesis was to produce bulk nanocrystalline Nb_3Sn with the aim of improving its superconducting properties. In the previous chapter, results from ball milling Nb_3Sn powder to introduce disorder (and reduce grain size) were presented in the context of the current state of knowledge about this materials fabrication technique. In this chapter, details of the Hot Isostatic Press (HIP) method used to consolidate Nb_3Sn powder disordered by milling into bulk, nanocrystalline samples are presented. This will focus on several aspects: which milled powder was used, how HIP parameters were chosen; precautions taken to retain sample purity; and XRD characterisation of the results of HIP'ing. Characterisation of the superconducting properties of the resulting bulk nanocrystalline samples will then be covered in Chapter 7.

6.2 Process

The aim of HIP'ing in this work is to produce dense, bulk samples from the very fine (particle size ~1 μm, grain size ~25 nm) powder produced by milling. The conventional techniques to achieve densification either involve high temperatures (sintering) or high

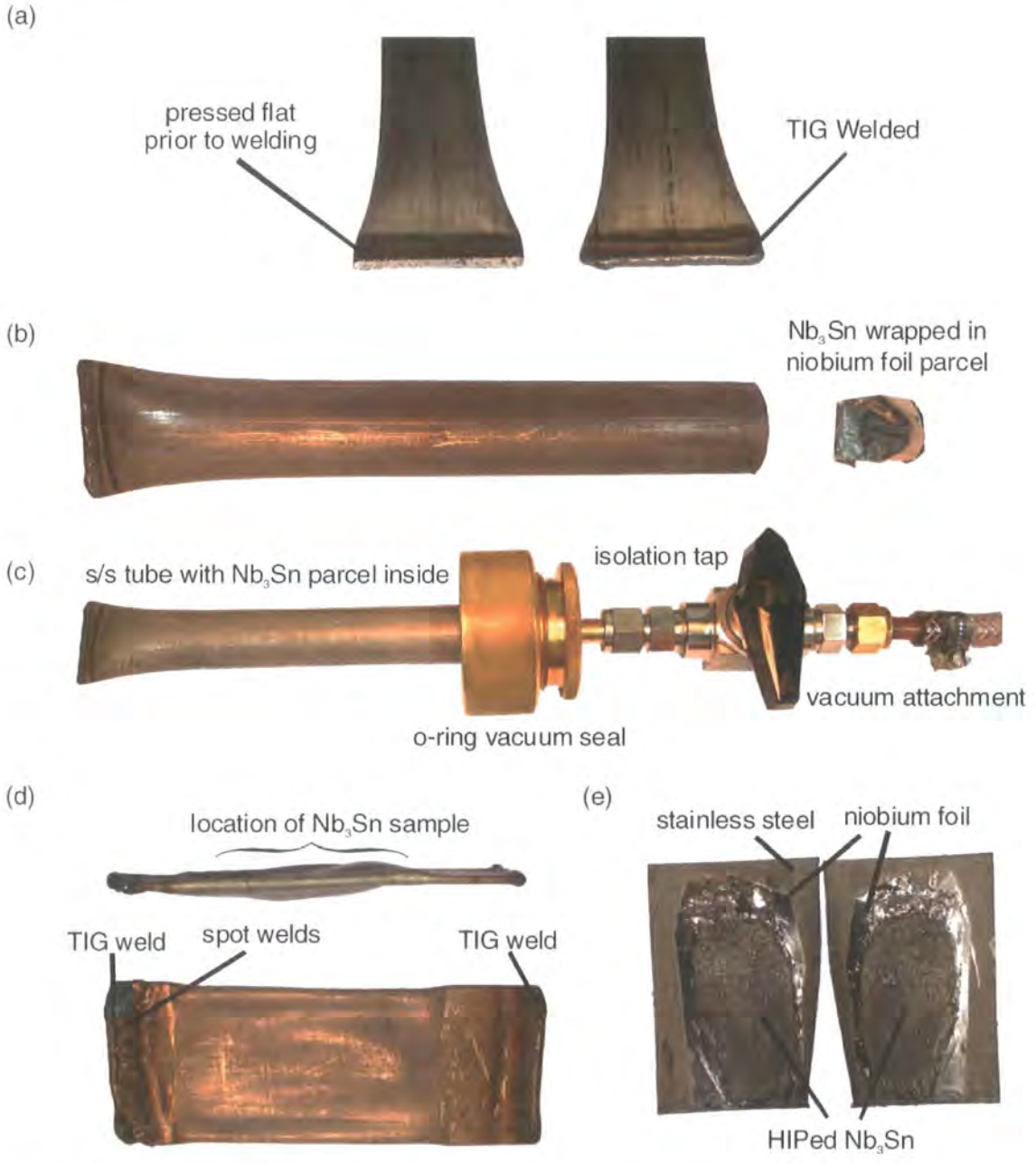

Figure 6.1 (a) 22 mm diameter seamless 316 stainless steel tube (s/s), with wall thickness 1 mm, was pinched and TIG welded at one end; (b) in an argon glove box, 25 μm niobium foil was used to contain the Nb_3Sn powder sample, which then slid into the s/s tube; (c) sample was retained in an argon environment outside the glove box by closing the open end of tube with an o-ring seal and closed tap, s/s tube was then evacuated, and sealed under vacuum by pinching the tube above the position of the sample, spot welding and subsequent TIG welding to form a HIP billet; (d) views of billet after Cold Isostatic Pressing (CIP'ing), showing s/s flattened around the sample; (e) two halves of a HIP'ed billet after being cut open, showing HIP'ed Nb_3Sn was still protected from contact with s/s by the niobium foil.

pressures (e.g. unidirectional pressing). To achieve full density, sintering would result in extensive re-crystallisation and grain growth, and the times and extreme pressures which would be required for cold pressing would be impractical. The HIP uses a combination of pressure (≤2000 Bar) and temperature (≤2000 °C), allowing densification to occur at a lower temperature (pressure) than sintering (cold pressing) would alone. This means that grain growth during densification is minimised. Pressure is applied isostatically by compressing high purity (99.998 %) argon gas, which prevents sample incineration, minimises gas absorption into the sample and compresses samples evenly.

The milled Nb_3Sn powder chosen for consolidation was that milled in niobium for 8 hours at 450 rpm under a dual argon atmosphere, as this ensured that the sample produced was binary Nb_3Sn uncontaminated with ternary contaminants from the milling medium used. As mentioned previously (Section 5.3.3), milling in niobium media increased the niobium content of the sample, which had to be quantified and corrected for using ICP-MS analysis. Two batches of Nb_3Sn milled under the same conditions were needed to produce a series of HIP'ed samples, and ICP-MS analysis showed that the overall Nb:Sn atomic ratio in these batches had increased from 3 to 4.57 and 4.41 respectively. Tin powder (Table 5.3) from Alfa Aesar with a purity of 99.8 wt. % (metals basis) and a mesh size of -325 (particle size <44 μm) was used to bring the stoichiometry back to that of Nb_3Sn. The mixture of the two milled powders and the tin with total mass ~38 g was then homogenised by sealing the powder in a specially-designed oxygen-free (C101 grade, Table 5.3) copper pot which was then continually rotated for ~12 hours by a device purpose built for this work. All powder processing was carried out in an argon glove-box with low oxygen and moisture levels.

Care has to be taken to ensure that powder is kept contained during the HIP process, so that the HIP'ed sample is in a shape suitable for subsequent bulk superconductivity measurements. This was achieved by wrapping 5 - 6 g of milled powder in 25 μm

niobium foil of 99.8 wt. % (metals basis, Table 5.3) purity to form a shape as cubic as possible (Figure 6.1b). Tight folds were used to ensure that powder did not escape, and a secondary wrapping of niobium foil was then added for extra protection. As outlined in Section 5.3.3, oxygen and nitrogen contamination were avoided when milling the Nb_3Sn to be HIP'ed, by sealing the milling pot in an argon-environment and by setting up the milling machine within a secondary argon atmosphere as an additional precaution. Following the care taken during milling, a new procedure was introduced to ensure that the milled powder was not exposed to air before being HIP'ed. A seamless 316 stainless steel (s/s) tube of 20 mm diameter and 1 mm wall-thickness is sealed at one end by TIG (Tungsten Inert Gas)-welding (Figure 6.1a). The s/s tube is then put into the argon-glove-box, and the Nb_3Sn powder parcel is inserted into the tube so that it slides down to the bottom (Figure 6.1b). A vacuum-line fitting and a tap with an o-ring seal is then attached to seal the argon environment inside the s/s tube (Figure 6.1c). The tube can then be taken out of the glove-box whilst still retaining the argon environment, and evacuated using a rotary pump. The tube is then pinched closed above the position of the powder parcel in the end of the stainless-steel tube, and spot-welds across the pinched section of tube then seal the sample in the end of the s/s tube to form a ~10 cm-long evacuated billet. The billet is then cut off the main s/s tube and the spot-welded closure is reinforced by an additional TIG weld, as spot-welds may fail under the extreme stresses exerted in the HIP. As a check for this work, thermocouple measurements were made of the temperature reached in the powder billet during the spot welding and subsequent TIG welding processes. The temperature within a powder-parcel was found to reach ~130 ^{o}C, which is well below the temperatures subsequently used during HIP'ing. Samples were then Cold-Isostatic Pressed (CIP'ed) at 2000 Bar prior to HIP'ing, to ensure that the samples' seals would hold (Figure 6.1d).

There are no data in the literature on the use of a HIP for consolidation of pre-alloyed Nb_3Sn powder, so HIP temperatures were chosen with reference to the lowest temperatures in the literature at which pre-cursor materials formed Nb_3Sn. 450 °C was the lowest temperature found for the onset of Nb_3Sn formation by the bronze-route [95], well above 232 °C, the melting point of tin [48], and so this was chosen as the lowest HIP temperature. At the upper-end of the temperature scale, 675 °C is typically used for binary Nb_3Sn wire production [96, 97], and Nb_3Sn was found to recrystallize from amorphous material in the range 700 - 750 °C during DTA [27], so 750 °C was chosen as the highest temperature. The range chosen was confirmed by carrying out a temperature-dependent XRD measurement on the milled sample. Figure 6.2 is a plot of Scherrer grain sizes against temperature, suggesting microstructural rearrangement would start to occur

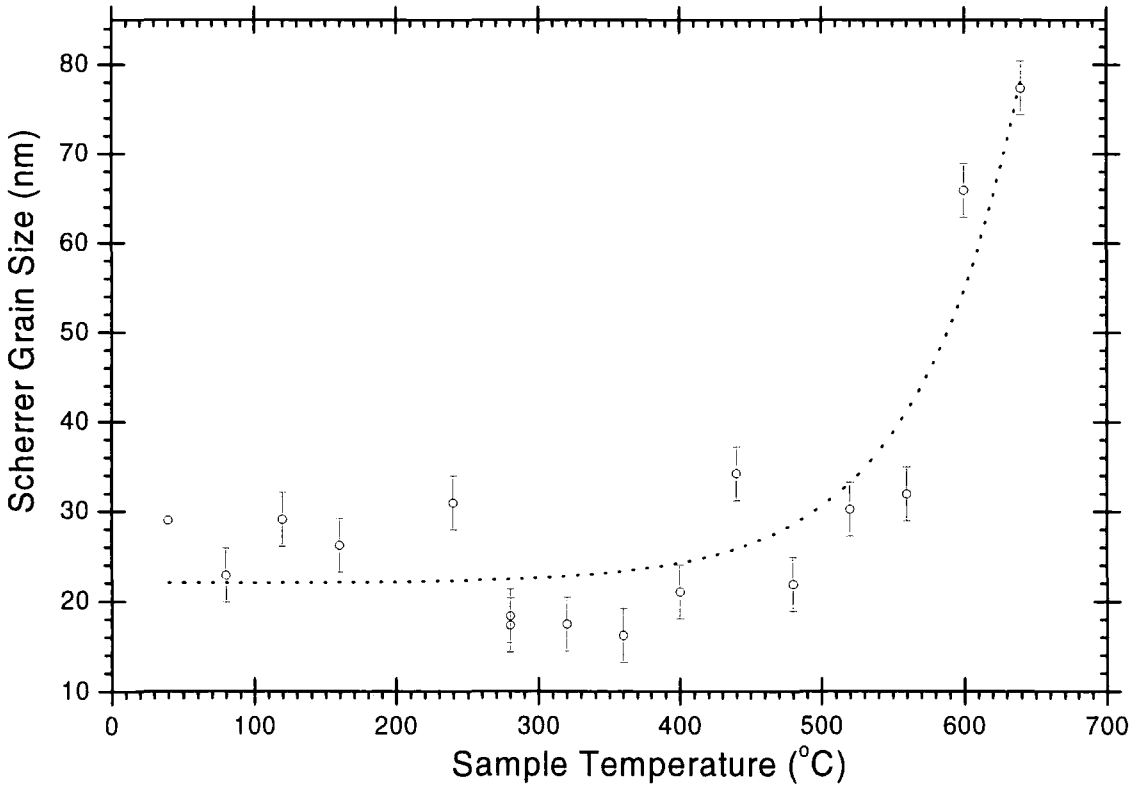

Figure 6.2 Grain size change with temperature for XRD measurements made in a variable-temperature diffractometer, showing that on short timescales, discernable grain growth in the milled Nb_3Sn occurs at temperatures above ~550 °C. The line is a guide to the eye.

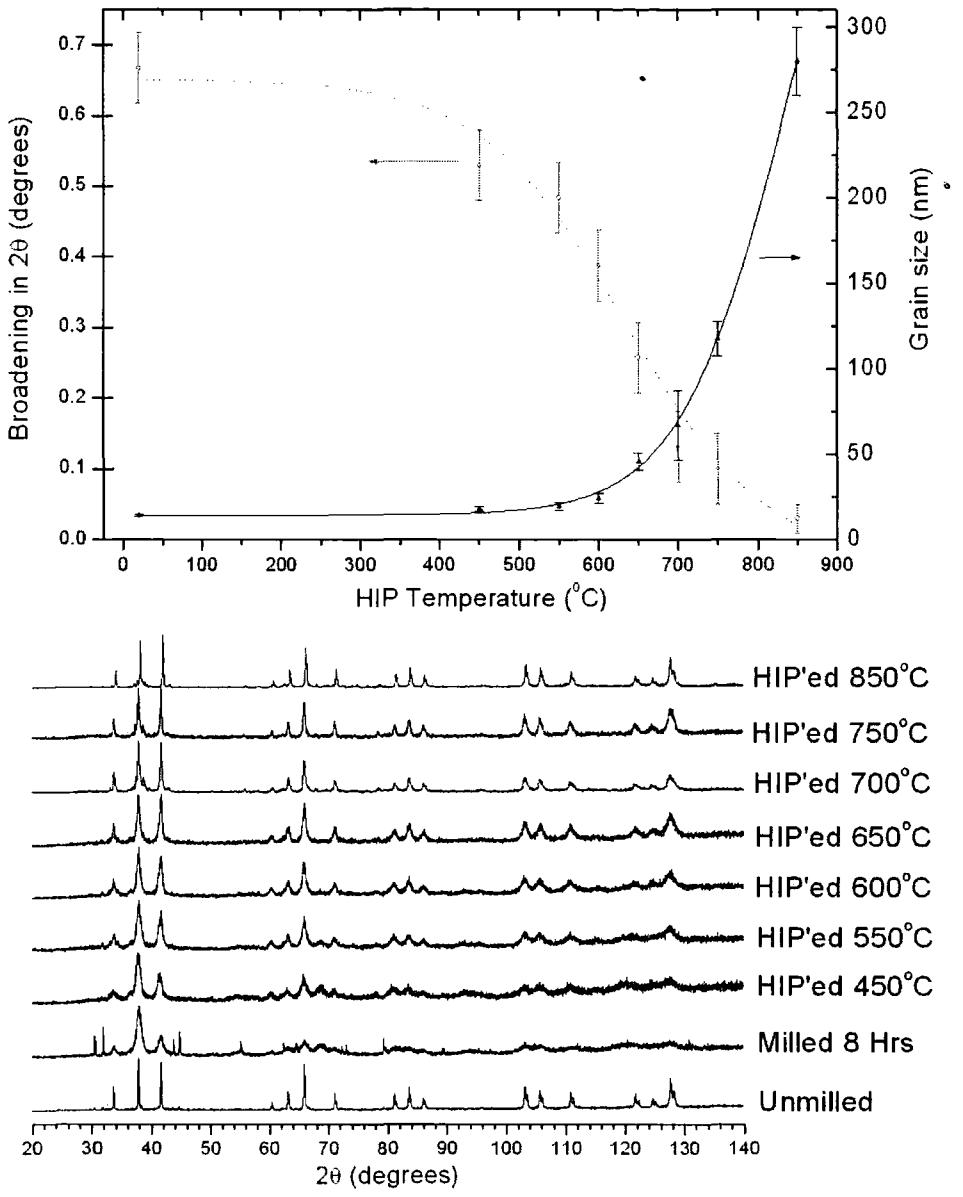

Figure 6.3 Effect of HIP temperature on grain size growth during consolidation. Grain sizes are calculated using Scherrer analysis of peak broadening in XRD spectra. The lines are a guide to the eye.

at around 600 °C. It should be noted that the crystallisation temperature of amorphous solids typically only increases with pressure by only 5 - 50 K GPa^{-1} [98], and as the pressure used for HIP'ing in this work is 2000 Bar (0.2 GPa), changes in crystallisation temperature are predicted to be < 10 K. It is therefore valid to choose HIP temperatures based on data at ambient pressure. After some characterisation of the samples HIP'ed at

lower temperatures, the final HIP temperatures used were 450, 550, 600, 650, 700 and 750 °C. Part of the 450 °C HIP'ed sample was re-HIP'ed at 850 °C to provide additional information about the superconductivity in a sample taken closer to the annealing temperature. HIP Samples of the as-supplied Nb_3Sn (unmilled) were also prepared at each temperature as a consistency check.

During each HIP cycle, the pressure was ramped at 23 Bar min^{-1} up to 2000 Bar, and the temperature ramp rate was chosen so that both pressure and temperature reach their target values at the same time. These conditions are maintained for ~5 hours, after which both temperature and pressure are ramped down, and the samples can be recovered by cutting open the HIP billets. Temperatures in the inner- and outer-zones of the HIP were measured using type-B thermocouples, and the error on the temperature maintained during the HIP period is likely to be of the order of ±10 °C. Figure 6.1e is a photo of an open HIP billet (of unmilled powder HIP'ed at 700 °C), showing that the niobium foil wrapping is retained during HIP'ing, ensuring that the Nb_3Sn is separated from contact with the stainless steel tube.

6.3 Results

XRD data of the milled and HIP'ed Nb_3Sn samples (Figure 6.3) show a systematic increase in Scherrer grain size with increasing HIP temperature. It can be seen that after HIP'ing at 850 °C, the grain size has recovered to levels of ~0.3 μm, approaching that of the as-supplied unmilled Nb_3Sn powder (particle size ~1 - 500 μm). As was seen with the temperature-dependent XRD data taken, 600 °C is a temperature at which significant microstructural change occurs. The superconducting properties of these HIP'ed samples will be the subject of the next chapter.

Chapter 7

Electromagnetic measurements on HIP'ed samples

7.1 Introduction

The previous chapter covered details of the HIP'ing process used to consolidate milled powder at a range of temperatures. In this chapter, data on the superconducting properties of these samples will be presented. In Section 7.2, d.c. measurements of hysteretic magnetic moment as field is ramped up and down will be discussed briefly. More comprehensive a.c. measurements of magnetic moment as a function of temperature were made at a range of applied fields, and these will be presented, analysed and discussed in Section 7.3, along with resistivity data for some samples.

Table 7.1 Summary of HIP'ed samples and their superconducting properties

ID	milling parameters				HIP conditions			grain size	real moment (m') vs. temperature				resistivity vs. temperature		
	miller	medium	time (hrs)	grain size (nm)	temp. (°C)	time (hrs)	pressure (Bar)	nm	onset of transition		half transition		half transition		ρ_N(20 K)
									$T_c^{\chi''=0}$	$B_{c2}^{\chi''=0}(0)$	$T_c^{0.5\chi''=0}$	$B_{c2}^{0.5\chi''=0}(0)$	$T_c^{0.5\rho_N}$	$B_{c2}^{0.5\rho_N}(0)$	(10^{-6} Ω m)
M450	Fritsch P6	Nb	8	14	450	5	2000	18	9.0	8.0	2.5				
M550	Fritsch P6	Nb	8	14	550	5	2000	20	9.3	12.4	7.2	5.6			
M600	Fritsch P6	Nb	8	14	600	1	2000	24	10.6	17.9	9.1	12.3			
M650	Fritsch P6	Nb	8	14	650	5	2000	46	14.4	27.9	13.4	24.1	15.1	29.8	2.9
M700	Fritsch P6	Nb	8	14	700	5	2000	67	16.5	29.5	15.7	29.1	16.4	31.7	2.0
M750	Fritsch P6	Nb	8	14	750	4.5	2000	118	17.3	28.2	16.9	28.0	17.4	28.2	1.6
M850	Fritsch P6	Nb	8	14	850	5	2000	280	17.9	25.2	17.7	24.5			
C650	unmilled commercial Nb_3Sn				650	5	2000	~1000	18.0	26.2	12.2	7.2			
CWire	commercial Nb_3Sn wire				-	-	-		17.6	27.6	17.2	24.6			

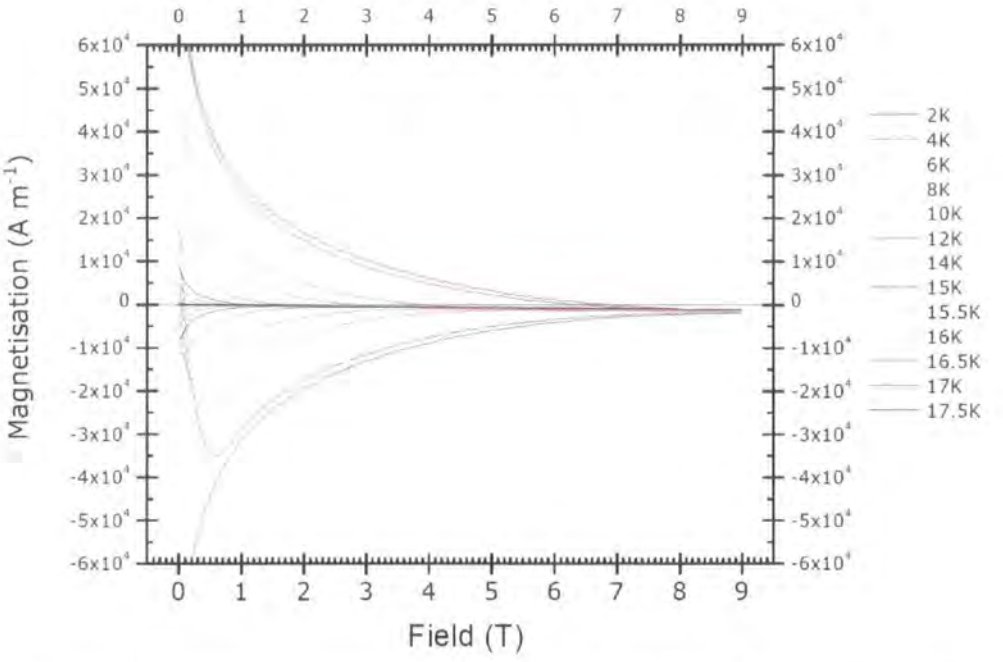

Figure 7.1 Typical hysteretic magnetisation versus applied field data at a range of temperatures. These data are for a commercial wire (CWire)

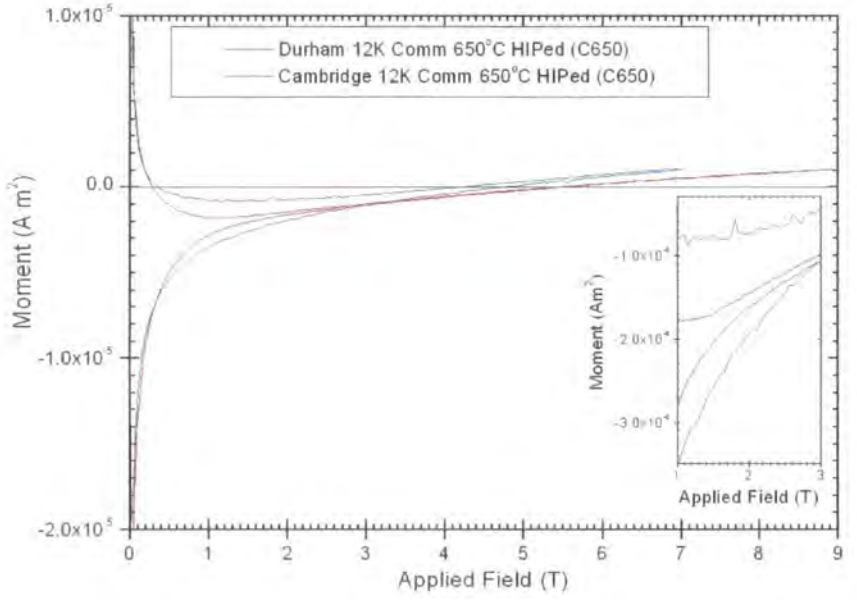

Figure 7.2 Plots of hysteretic magnetic moment, *m*, against applied field at 12 K taken using the PPMS system in Durham and the MPMS SQUID in Cambridge (measurement made by D Astill) for the same sample (C650). These plots all show a disparity in the magnitude of the magnetic moment, suggesting that the hysteretic difference in magnet moment for increasing and decreasing fields cannot be relied upon to calculate accurate values for J_c.

7.2 Hysteretic magnetic measurements

Measurement of the magnetic moment of bulk samples at fixed temperatures as magnetic field is ramped up and down results in a hysteretic effect due to flux pinning (Section 2.2.6). If demagnetisation and shape factors are taken into account, a value for J_c, the critical current density of a sample, can be extracted from these data (Section 2.3.1). These J_c values can give a good indication of the technologically important transport critical current density. In this work, d.c. hysteretic measurements were made of HIP'ed samples described in the previous chapter, using a Quantum Design Physical Property Measurement System (PPMS) with applied fields up to 9 T and temperatures down to 2 K. Nb_3Sn samples milled in niobium for 8 hours in the Fritsch miller and HIP'ed at 450, 550, 600, 650, 700, 750, and 850 °C will be referred to as M450 to M850 respectively (Table 7.1). Measurements were also made of commercial samples for comparison: unmilled Nb_3Sn HIP'ed at 650 °C (C650) and a commercial ternary Nb_3Sn wire, AS#1, from American Superconductor (CWire). Ternary additions (e.g Cu, Ti) boost the technologically important value $B_{C2}(0)$ in commercial wires. Figure 7.1 shows hysteresis data taken in Durham for CWire. Three samples (M450, C650 and CWire) were re-measured in a Quantum Design MPMS system in Cambridge by D Astill. Figure 7.2 shows a comparative plot of hysteretic data from C650 taken in Cambridge and Durham. Analysis shows that in all comparative data, the onset of superconductivity occurs at the same temperatures, but that the magnitudes of the magnetic moments are inconsistent. Bean model J_c values will therefore not be presented as they are dependent on the accuracy of these data. The aim of this work was to produce an increase in $B_{C2}(0)$ and, as described in the next section, these values have been provided by measuring magnetic moment and resistivity as a function of temperature (at stable field) instead.

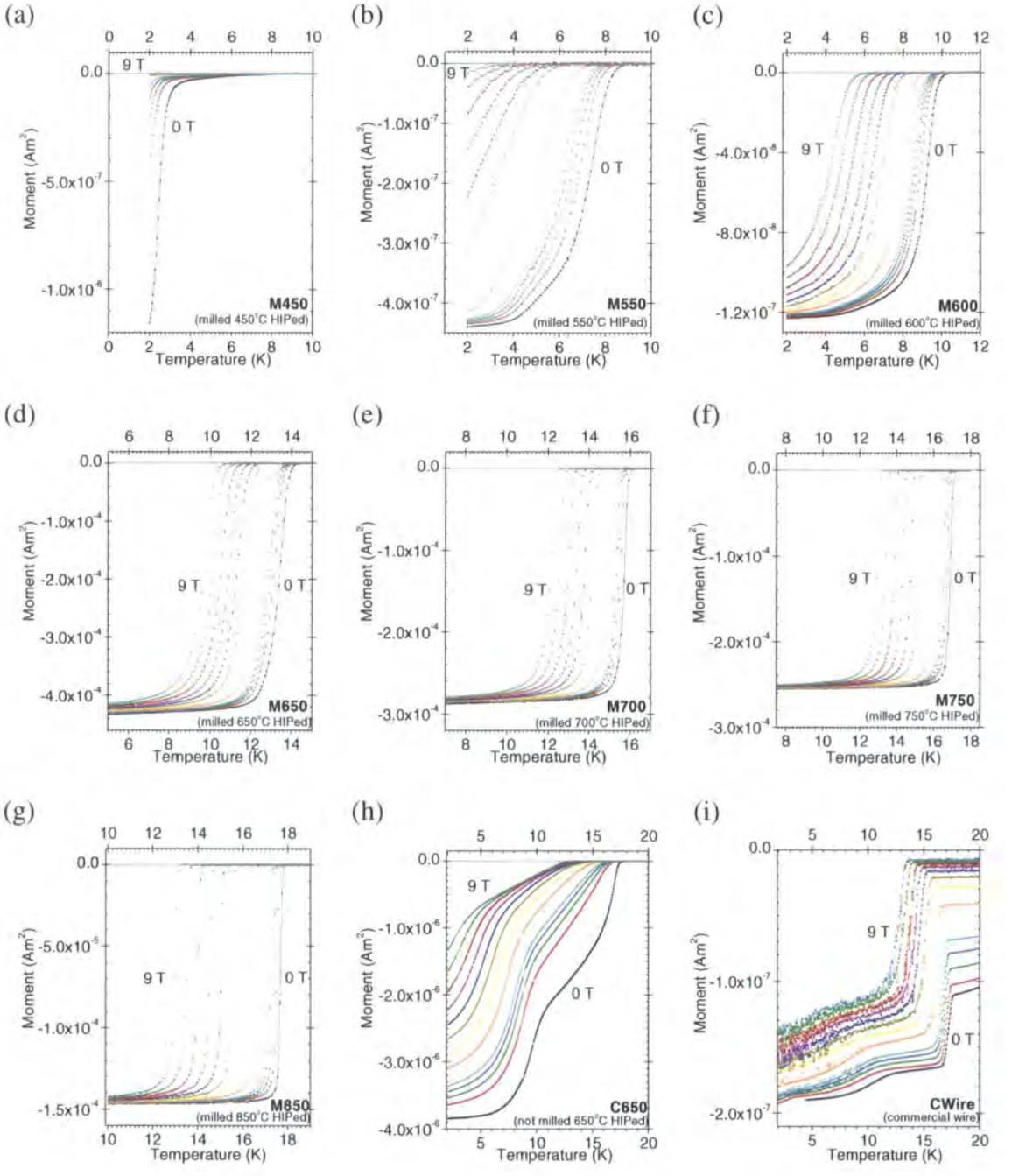

Figure 7.3 Plots of magnetic moment against temperature at 0, 0.25, 0.5, 1, 2, 3, 4, 5, 6, 7, 8 and 9 Tesla (0 T and 9 T labels indicate trend). Magnetic moments were measured using an applied field with an a.c. component indicated in brackets. Data are for milled Nb_3Sn HIP'ed at **(a)** 450 °C (10 x 10^{-4} T, 1000 Hz), **(b)** 550 °C (4 x 10^{-4} T, 777 Hz), **(c)** 600 °C (1 x 10^{-4} T, 777 Hz), **(d)** 650 °C (4 x 10^{-4} T, 777 Hz), **(e)** 700 °C (4 x 10^{-4} T, 777 Hz), **(f)** 750 °C (4 x 10^{-4} T, 777 Hz) and **(g)** 850 °C (4 x 10^{-4} T, 777 Hz). For comparison, **(h)** unmilled Nb_3Sn powder HIP'ed at 650 °C (10 x 10^{-4} T, 1000 Hz) and **(i)** a commercial Nb_3Sn wire (1 x 10^{-4} T, 777 Hz) are included.

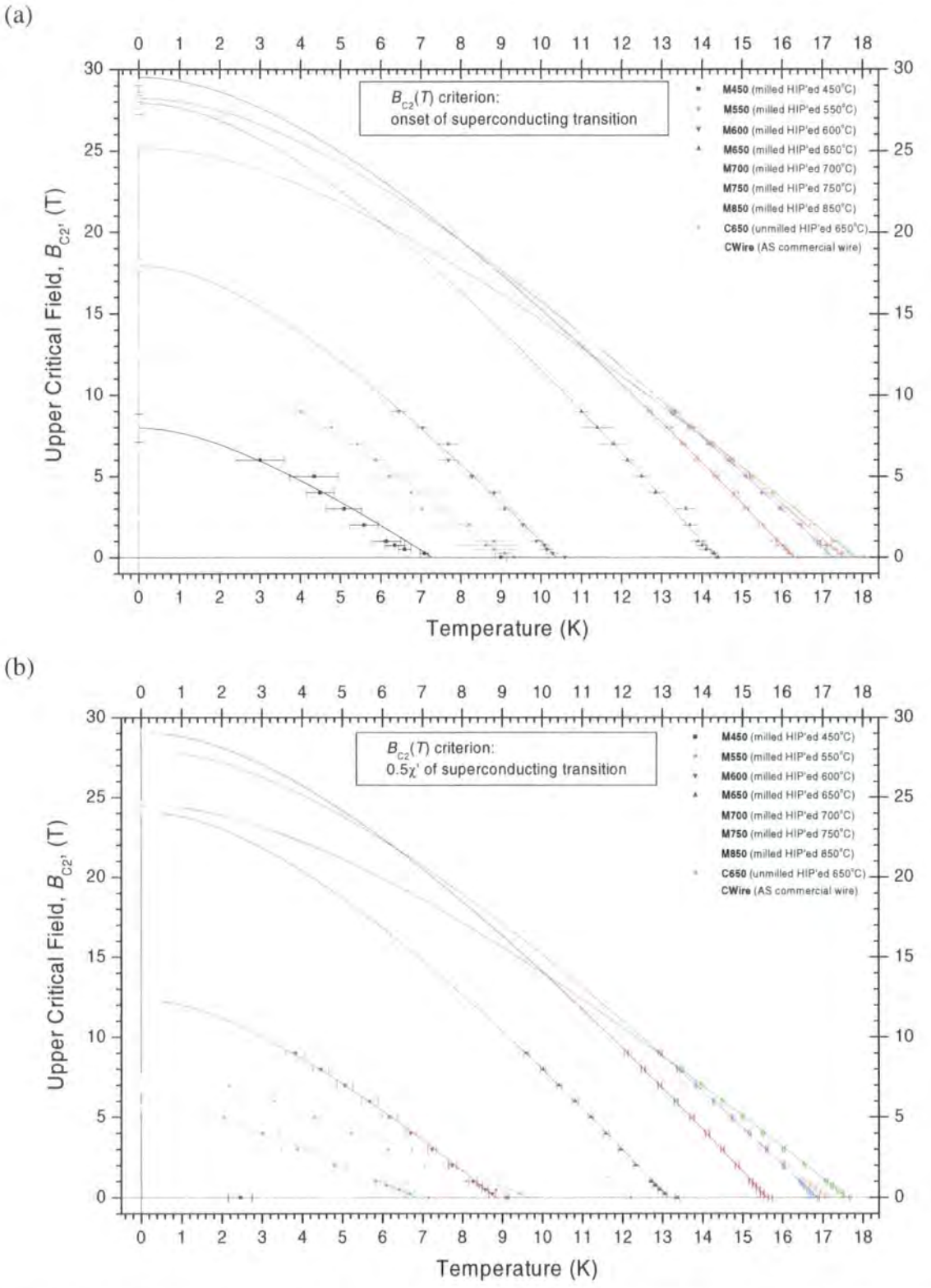

Figure 7.4 Upper critical field, B_{C2}, vs. temperature for Nb_3Sn samples milled in niobium and HIP'ed at a range of temperatures; as well as a commercial ternary Nb_3Sn wire and unmilled Nb_3Sn HIP'ed at 650°C. $B_{C2}(T)$ values are from magnetisation versus temperature data at a range of fields, using **(a)** onset and **(b)** 0.5χ' criteria. The fits are Maki-DeGennes extrapolations.

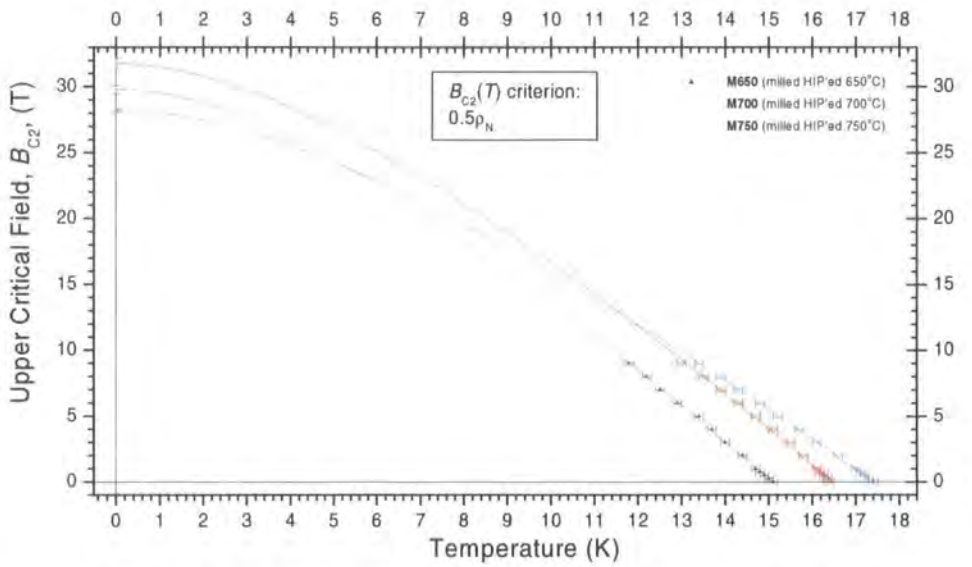

Figure 7.5 Upper critical field, B_{C2}, vs. temperature for M650, M700 and M750 (Nb_3Sn milled in niobium and HIP'ed at 650, 700 and 750 °C). $B_{C2}(T)$ values in this figure are from resistivity measurements (of bulk samples) made by J Y Xiang using the PPMS system in Durham, analysed using a transition criterion of $0.5\rho_N$. The fits are Maki-De Gennes extrapolations.

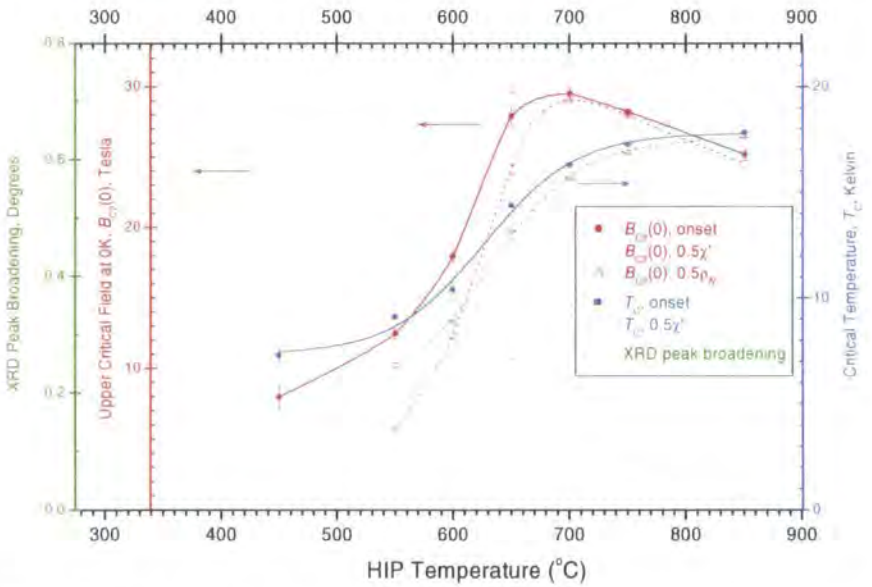

Figure 7.6 Plot of: XRD peak broadening in degrees (green axis, far left); upper critical field, $B_{C2}(0)$, in Tesla (left-hand red axis); and critical temperature, T_c, in Kelvin (right-hand blue axis) for Nb_3Sn milled samples, against the HIP temperature used for consolidation. Values of $B_{C2}(T=0)$ and T_c values are from Maki-De Gennes fits to magnetic moment (onset and $0.5\chi'$ criteria) and resistivity ($0.5\rho_N$ criterion) against temperature data at a range of magnetic fields. All lines have been included as a guide to the eye. Resistivity data were taken by J Y Xiang.

7.3 Variable temperature measurements

As described in Chapter 6, the relatively large quantity of milled powder produced during milling allowed 5-6 g of powder to be consolidated at each HIP temperature. This process produced samples of Nb_3Sn ~2 mm thick and ~4 cm long and ~2 cm wide. The brittle nature of Nb_3Sn resulted in some fracture during extraction from the HIP billet, but there still were a number of bulk samples from each HIP temperature. This allowed XRD, magnetic and resistive measurements to be made on relatively large bulk samples, particularly important for resistive measurements, where carrying out measurements on samples ~7 mm long reduced the error on the resistivity data considerably. Details of the magnetic and resistive measurements at variable temperature will be discussed in this section.

Figure 7.3 shows data from measurements of magnetic moment as a function of temperature, taken at applied fields of 0, 0.25, 0.5, 0.75, 1, 2, 3, 4, 5, 6, 7, 8 and 9 T, for each of the bulk samples detailed in Table 7.1. The measurements are of the samples' response to a small applied a.c. field (in addition to a much larger stable applied field), with a typical amplitude and frequency of 4×10^{-4} T and 777 Hz respectively (see Figure 7.3 caption for specific parameters used). Each moment plotted is the real component of the sample's response, and superconducting screening currents produce a clear transition with temperature as the sample passes into the superconducting state. There are different criteria for defining at what point during this transition the sample has become superconducting. In this work, two criteria have been used: the onset, when the magnetic moment first deviates from the normal-state response; and $0.5\chi'$, the temperature at which the magnetic moment is half-way between the minimum and maximum moment of the superconducting transition. In practice, the onset criterion is clear in all cases, but

determining 0.5χ' can be more ambiguous. For example, C650 and CWire have two noticeable stages in their transitions (Figure 7.3: h and i). In the case of CWire, the commercial wire, this transition shape is often found [99], and is due to the manufacturing process. The Nb_3Sn filaments in commercial wires are formed in-situ by a heat treatment of pre-cursor materials. Therefore, the first transition will be the main on-stoichiometric ternary filament, and then off-stoichiometric boundary regions with lower values of T_c will contribute at lower temperatures. In the case of C650, the unmilled Nb_3Sn powder HIP'ed at 650 °C, the shoulder on the transition is likely to be due to imperfect boundaries between consolidated Nb_3Sn particles in the bulk sample. Oxygen or nitrogen impurities on the surface of the as-supplied powder may have hindered greater connectivity. For CWire, the 0.5χ' criteria was applied only to the sharp region of the transition below the onset, as this is likely to be more representative of the technical properties of the wire. The shoulder in the C650 data was too indistinct to be analysed in the same way, and so data from the onset-criterion are more indicative of the properties of Nb_3Sn with low levels of disorder. In contrast, the milled, HIP'ed samples (in particular M600, M650, M700, M750, and M850) have smooth transitions (Figure 7.3: c, d, e, f, and g respectively). Consequently, there is good correspondence for these samples between the $B_{C2}(T)$ data determined using the onset and 0.5χ' criteria (Figure 7.4: a and b respectively). This suggests fabricated samples have a high degree of homogeneity and good connectivity between consolidated particles, even after HIP'ing at relatively low temperatures. These sharp transitions support the evidence in the previous chapter that precautions taken to avoid exposing milled powder particles to air were successful, as an oxide or nitride layer on milled powder particles might be expected to result in a two-stage transition such as that seen in C650. It is also important to note that the sharp transitions seen for M700, M750 and M850 indicate that any variations in stoichiometry within the sample are small. The transitions at lower temperature, in particular for M450

and M550 (450 °C and 550 °C HIP temperature respectively), are broader but this does not necessarily suggest variations in stoichiometry as the disordered microstructure is likely to contribute to variations in superconductivity within the material as well.

Resistivity measurements of the best samples (M650, M700, and M750) were made in the PPMS by J Y Xiang. A four-probe measurement was used, with silver-coated copper wire contacts attached using conductive epoxy. Resistivity measurements at different applied magnetic fields were taken as temperature was ramped down from 20 K to 5 K in 0.3 K steps. $B_{C2}(T)$ values determined from resistivity data, using a criterion of $0.5\rho_N$ (i.e. half the value of the normal state resistivity measured just above T_c), are presented in Figure 7.5. The normal state resistivities at 20 K, ρ_N(20 K), of these samples are included in Table 7.1. Typical literature values of ρ_N for binary Nb_3Sn are in the region 4×10^{-8} Ω m (25 at. % Sn) to 4×10^{-7} Ω m (24.5 at. % Sn) [100]. The values of $2.9 \pm 0.3 \times 10^{-6}$ Ω m (M650), $2.0 \pm 0.3 \times 10^{-6}$ Ω m (M700) and $1.6 \pm 1 \times 10^{-6}$ Ω m (M750) found for the samples fabricated in this work are therefore extremely high. From XRD spectra, it can be seen that disorder introduced during milling has not relaxed at these HIP temperatures (Figure 7.6), and as there is no evidence of contamination, these high resistivities must be primarily due to microstructural disorder. The high resistivities mean that, making the reasonable assumption that S^2/γ (where γ is the Sommerfeld constant and S is the Fermi surface area) has not been decreased by a factor ~5 in these samples, simplified "dirty limit" BCS relationships can be used [20]:

$$-\left.\frac{\partial B_{C2}}{\partial T}\right|_{T_c} \propto \rho_N \gamma \qquad (7.3.1)$$

$-(\partial B_{C2}/\partial T)|_{T_c}$ values for milled samples increase with HIP temperature up to a peak around 650-700 °C and then decrease at higher HIP temperature (Figure 7.4a and Figure 7.4b). As seen in the previous chapter (Figure 7.6), the disorder in the milled samples

consistently decreases with HIP temperature, and this would be expected to result in a decrease in resistivity with increasing HIP temperature (due to a reduction in electron scattering). The resistivity data for the samples measured so far would seem to confirm this trend. Electron scattering due to disorder can depress γ by smearing out the peak in the electron density of states at the Fermi surface [101]. It is therefore expected that γ values will have recovered (increased) with HIP temperature, but heat capacity data would be needed to confirm this. Equation (7.3.1) implies that the explanation for the initial increase in gradient with HIP temperature is that γ recovery outweighs ρ_N reduction at lower HIP temperatures, allowing an increase in gradient up to 650-700 °C. This behaviour has been seen in nanocrystalline microstructures, in which high γ values within grains would co-exist with high resistivity due to scattering at grain boundaries [3]. The reduction in $-(\partial B_{C2}/\partial T)|_{T_c}$ at higher HIP temperatures, to values comparable with that of C650 and CWire, suggest γ and ρ_N return to more normal levels after heat treatment at ~850 °C. This coincides with the reduction in disorder seen from XRD data. Therefore, the relationship between $-(\partial B_{C2}/\partial T)|_{T_c}$ and HIP temperature is explicable if the microstructural disorder present affects γ and ρ_N differently. In addition, the effect on γ and ρ_N is likely to vary depending on the spatial distribution and type of disorder present. Different kinds of disorder are likely to relax at different HIP temperatures. Heat capacity measurements in conjunction with TEM analysis would be needed to come to conclusions about the mechanisms in these samples.

An increase in $-(\partial B_{C2}/\partial T)|_{T_c}$ is a necessary, but not sufficient, condition for increasing $B_{C2}(0)$. In the dirty limit, Equation (2.4.1) reduces to the simpler relation:

$$B_{C2}(0) \propto \gamma T_C \rho_N \qquad (7.3.2)$$

The third important factor in determining $B_{C2}(0)$ is therefore T_c. In graphical terms, an increase in the gradient $-(\partial B_{C2}/\partial T)|_{T_c}$ will not translate into an increase in $B_{C2}(0)$ if T_c has been depressed too much by disorder. For the milled, HIP'ed samples, T_c consistently increases with HIP temperature up a value of $T_c^{\chi'=0}$ = 17.9 K for M850 (Table 7.1, Figure 7.6). This critical temperature is larger than that of the commercial wire (17.6 K), close to the value for C650 (18 K), and therefore comparable to values for binary Nb_3Sn wires in the literature (~17.8-18.0 K [99]). T_c for the as-supplied (unmilled) powder was found to be 17.9 K (using a Quantum Design MPMS courtesy of I Terry). T_c is therefore depressed by milling, but returns to its original value if it is HIP'ed at a high enough temperature, suggesting that the effect of milling is simply through the introduction of microstructural disorder, as it appears to be reversible by annealing.

We now turn to the aim of the work, which was to increase the technologically important upper critical field. $B_{C2}(0)$ values (Table 7.1) have been found by using the well established Maki-De Gennes relationship [101] to fit $B_{C2}(T)$ data (Figure 7.4 and Figure 7.5) determined from magnetic and resistive measurements. The Maki-DeGennes relationship is derived from microscopic theory and has been found to fit the form of $B_{C2}(T)$ for Nb_3Sn very closely [101]. The reliable, high-quality data from PPMS measurements ensure that the values of $B_{C2}(0)$ can be determined with relatively small uncertainties. With the exception of 0.5χ' data for C650 (discussed above), $B_{C2}(0)$ values for the "standard" samples measured; ternary CWire ($B_{C2}^{\chi'=0}(0)$ of 27.6 ± 0.3 T) and C650 ($B_{C2}^{\chi'=0}(0)$ of 26.2 ± 0.9 T); are comparable to values in the literature [103]. Of the fabricated samples: T_c, ρ_N and γ are sufficiently high to produce increases in $B_{C2}(0)$ for M650, M700 and M750 (milled samples HIP'ed at 650, 700 and 750 °C respectively). The highest $B_{C2}^{\chi'=0}(0)$ value is 29.5 ± 0.5 T for M700, a significant increase above 27.6 ± 0.3 T for CWire, the commercial ternary wire (ternary additions increase B_{C2}), and 26.2 ± 0.9 T for the unmilled sample HIP'ed at 650 °C (M650). If the 0.5χ' criterion is

used (Figure 7.4b), the improvement is larger: 29.1 ± 0.2 T for M700 in comparison to 24.6 ± 0.3 T for CWire). This difference between criteria is likely to be due to better sample homogeneity of the fabricated samples in comparison to the commercial samples, as discussed above. The upper critical fields found are even higher when $B_{C2}(T)$ data are determined resistively, using the criterion $0.5\rho_N$ (Figure 7.5). This is expected, due to transport current percolation through the "best bits" of the sample. Resistivity measurements are of considerable technological interest, as it is the current-carrying properties of Nb_3Sn which are critical for wires in high-field magnet applications, and most $B_{C2}(0)$ values for commercial wires in the literature are determined resistively. The $B_{C2}(0)^{0.5\rho_N}$ value of 31.7 ± 0.4 T for M700 is an extremely high value for binary Nb_3Sn, and is ~6 T higher than typical $B_{C2}(0)$ values for binary Nb_3Sn in the literature [99], although values of ~30 T have been quoted [36].

The peak in $B_{C2}(0)$ occurs at a HIP temperature of around 700 °C (Figure 7.6), when XRD broadening (average Scherrer grain size ~67 nm) and high resistivity (200 ± 27 μΩ cm) show that microstructural disorder introduced by milling is still present. In addition, it can be seen from this data (Figure 7.6 and Table 7.1) that when milled powder is HIP'ed at high temperature (850 °C), $B_{C2}(0)$ decreases to a value ~1 T below that of the unmilled sample, and XRD broadening by microstructural disorder indicates little disorder is retained (Scherrer grain size ~280 nm). The significant increase in $B_{C2}(0)$ therefore appears to be due to microstructural disorder. Large differences have also been seen between clean- (21.5 T) and dirty- (29 T) limit Nb_3Sn thin films due to differences in resistivity [20]. Lack of information about γ or the precise nature and density of microstructural faults present in the fabricated samples makes it difficult to come to firm conclusions about how accurate the simple picture of a nanocrystalline material with high γ and T_c within grains, co-existing with high resistivity from grain boundaries, is. The average Scherrer grain size for the optimum material fabricated in

this work is ~ 70 nm (Table 7.1), which is not particularly small in comparison to commercial wires (~100 nm [36]). However, Scherrer analysis is simplistic (Section 3.3), and cannot give information about the spread of grain sizes in a material, particularly as the average value will be biased towards the top end of the distribution. SEM could be used to give a better idea of grain sizes in M700. Alternatively, the high resistivity values could be due to other types of disorder, such as anti-site disorder, vacancies or partial dislocations, but these types of disorder might be expected to have a larger impact on T_c. There is also the possibility that the positive impact of small grains is off-set in commercial wires by deviations in stoichiometry and the presence of copper introduced during the wire manufacturing process [104].

Since the samples in this thesis were produced, in work awaiting publication, Cooley et al. have also reported improvements in $B_{C2}(0)$ to ~35 T using ball milling [105]. In their work, a SPEX miller with tungsten carbide pot was used to disorder Nb and Sn powders prior to heat treatment. There are disadvantages to this approach: annealed milled samples cannot be directly compared with the starting materials (to ensure changes are due to microstructure alone); milling in tungsten carbide is likely to result in (low levels of) contamination; heat treatment was not under pressure, so samples are porous; and no precautions were taken to control oxygen or nitrogen contamination. It is therefore not absolutely clear whether low levels of contamination or porosity may have contributed to increases in $B_{C2}(0)$, but it seems reasonable to assume that the unprecedented improvement seen is primarily due to microstructural disorder. In this work: the care taken in fabrication to avoid any ternary elements entering the sample; the high resistivity values found; the recovery of the $B_{C2}(0)$ and T_c of milled samples after heat treatment at high temperature; and the sharp transitions to superconductivity leave little doubt that increases in $B_{C2}(0)$ are due to microstructural disorder not doping.

In any case, doubts about contamination levels are only relevant for determination of the precise mechanism of the increase reported by Cooley et al., and are inconsequential to the important technological implications these increases could have. It is clear that, despite decades of work, the microstructure of Nb_3Sn in wires currently available is not yet optimised for maximum $B_{C2}(0)$, and that disorder introduced by ball milling provides a route for further improvements. The extensive work on ball milling in Chapter 5 indicates that the SPEX 8000D miller, in conjunction with a niobium pot, could allow the introduction of a greater range of microstructural disorder. It is not yet clear whether making Nb_3Sn amorphous before HIP'ing would create the optimum microstructure, or whether types of disorder (e.g. dislocations) present before amorphisation might survive better at higher compaction temperatures. Ball milling may also alter the stability of different stoichiometries. Investigation of these details will probably lead to $B_{C2}(0)$ optimisation beyond the significant increase seen in this work.

Chapter 8

Conclusions

8.1 HF process

As discussed in Chapter 4, Ti-6Al-4V springs are used by the Durham University Superconductivity Group to apply a range of strains to ITER-candidate Nb_3Sn superconducting wires, allowing accurate characterisation of the wires' superconductivity at high fields and a range of temperatures. Although Ti-6Al-4V has desirable engineering properties, it has a notoriously unreceptive oxidised surface, making it difficult to form a bond between the wire and the spring strong enough to transmit strain uniformly. A detailed procedure has been developed, adapted from a Rolls-Royce patented process, which allows Ti-6Al-4V springs to be nickel plated in the lab. Superconducting wires can then be copper-plated to the outside of the spring, as the nickel surface is much more receptive. An etch containing hydrofluoric acid (HF) is used, which not only removes the oxide layer from the spring, but also forms a protective film, preventing re-oxidation. Special materials and methods have had to be established due to the exceptionally corrosive nature of the hydrofluoric acid (HF). The step-by-step procedure set-up satisfies the stringent health and safety requirements surrounding HF's use, rendering risk of skin contact negligible. Bringing the process in-house has ensured the consistency and quality of the bond between wire and spring, and measurements using springs electroplated in this way have successfully been made on wires at strains from -1 % (tensile) to +0.3 % (compressive).

8.2 Milling conditions

In Chapter 5, work on optimising the ball milling process was presented, with the aim of producing high-purity disordered Nb_3Sn powder, which could subsequently be consolidated to form bulk samples. A large number of milling parameters have been investigated, primarily: milling machines (Fritsch Pulverisette 6, SPEX 8000D, Retsch MM301 and a Hosokawa 100AS jet miller), milling media (agate, niobium, copper, titanium, steel and tungsten carbide), speed (2-25 Hz), temperature (liquid nitrogen cooling, room temperature), milling time (15 minutes up to 240 hours) and scraping (every 30 minutes during milling). The effect of these milling parameters has been discussed in terms of the yield, contamination levels and microstructure of the milled powder. Contamination has been detected using ICP-MS. Following a series of standardisation experiments, it was found that contaminant levels (typically ~1 wt. %) could be measured with an error of ~5 % (i.e. 1.00 ± 0.05 wt. %). ICP-MS measurements were made by C J Ottley in the Earth Sciences department, although initial sample preparation and subsequent data analysis were my responsibility. Extensive powder XRD measurements have allowed identification of phases present in samples, and determination of the degree of microstructural change introduced by milling.

Yield is a potential barrier to fabricating enough milled powder for subsequent consolidation. The hardness and surface of milling media has been found to be an important factor in determining yield, particularly in the Fritsch miller. Yield from Fritsch milling in a hard, dissimilar material such as agate is consistently around 100 %, suggesting little agglomeration between powder and vial. Novel high-purity niobium, titanium and copper milling media have also been used in this work, to decrease the impact on superconductivity of contamination introduced from milling media wear. Use of these relatively soft milling media in the Fritsch miller resulted in low yields (indicating powder agglomeration) or yields in excess of 100 % (indicating high levels of

contamination). In particular, the highest yield achieved in copper, the softest material, was only 35 %. Low yields were particularly common during the initial stages of milling and at low speeds (yields at speeds below 300 rpm were never more than 40%). These observations have been explained in terms of the Fritsch's planetary action, in which milling balls spend a high proportion of time rolling around the sides of the milling vial rather than in energetic collisions. This makes the Fritsch prone to hard Nb_3Sn particles becoming embedded in the soft milling surfaces (initially), with further agglomeration on to this coated surface. At low speeds, milling balls pack down the caked powder, and allow powder to become trapped in volumes of the vial infrequently touched during milling. At higher speeds, the milling ball trajectories do not appear to change significantly, and the high proportion of rolling and grinding over collisions results in an increase in abrasive wear increasing yield, but at the expense of large increases in contamination. The effects were similar for niobium and titanium, but the initial coating stage took longer, during which yield was initially high. Retaining distinct boundaries between milling media and powder was shown to be important for maintaining yield. In contrast, the more chaotic collision-dominated motion of the milling balls in the SPEX and Retsch millers results in higher yields, even in copper milling media. The smaller vial size of the SPEX and Retsch millers enabled pots to be put in and out of the argon-glove box more quickly, allowing the effect of scraping the sides of the pot with a niobium rod every 30 minutes during milling to be investigated. There is clear evidence that regular scraping produces significant improvements in yield by breaking up caked powder: re-introducing agglomerated powder into the process and reducing the rate at which agglomeration re-occurs. In summary, using hard, dissimilar milling media in conjunction with chaotic collision-dominated milling machine such as the SPEX 8000D, and scraping the powder off the sides of the pot regularly, results in the most consistent yields.

Contamination could have a detrimental impact on superconducting properties. Three sources of contamination have been considered: Process Control Agents (PCAs), milling atmosphere and milling media wear. Examples in the literature indicate that although PCAs can help reduce powder agglomeration, they introduce significant contamination, and so were not used in this work. Contamination is known to be introduced by milling in air. The milling atmosphere was controlled by doing all fabrication work in a high purity argon environment, using milling pots with o-ring seals. In the case of Fritsch milling in niobium (used for the consolidated samples in this work) and agate, a secondary argon atmosphere enclosing the entire miller was used. XRD evidence and superconducting properties indicate that no oxide or nitride formation occurred during milling. Some milled samples were found to be pyrophoric, burning red-hot to produce a complex mixture of oxides and nitrides on exposure to air. Powder handling techniques have been used which deal with this problem. Milling media wear was the contamination source least easy to eliminate. The Hosokawa 100AS jet miller (courtesy of M Ghadiri, Leeds University) was trialled as an alternative approach to ball milling, as little contamination is introduced by this technique, but minimal microstructural disorder was introduced, and so this was not pursued. In conventional ball millers, contamination increases roughly linearly with milling time, as might be expected. Unconventional high purity niobium, titanium and copper milling media were specially manufactured to reduce the impact contamination would have on samples' superconductivity. These relatively soft media introduced contamination at a greater rate than more conventional media such as agate, tungsten carbide and steel. However, the difference between milling machines was a more significant factor. The Fritsch miller introduces contamination at such a large rate (~3 at. % per hour for niobium, titanium and copper and ~0.3 at % per hour for agate) that the only powder with acceptable levels of contamination was that milled in niobium, as the additional niobium introduced could

be corrected for with high purity tin prior to consolidation. Contamination appears to be introduced faster at higher milling speeds in the Fritsch miller. In contrast, the Retsch shaker miller introduced contamination at the lowest rate (~0.01 wt. % per hour), and the SPEX at a rate of between 0.25 and 0.5 at. % per hour. In the SPEX miller, regular scraping, which had a large beneficial impact on yield, did not increase the introduction of contamination. In similar conditions in the SPEX miller, milling in copper introduced contamination at the highest rate, almost twice that of harder tungsten carbide media. Steel introduced contamination at the lowest rate, but would have more serious effects on the superconducting properties than either copper or tungsten carbide. In conclusion, contamination can be minimised by milling in a purified argon environment using one of the shaker millers (SPEX or Retsch) in conjunction with a relatively hard milling medium. Scraping aids yield and does not appear to have a detrimental effect on contamination. Milling time should be minimised as far as possible.

The aim of milling was the introduction of microstructural disorder. As with yield and contamination, the milling machine was the most significant factor in determining the microstructure which could be produced. Grain size was found to decrease with milling time, reaching an equilibrium level after which no further reduction was achieved. Evidence from the literature suggests that grain boundary energy and anti-site disorder are likely to be the most energetically-significant types of disorder introduced into Nb_3Sn by milling, and if the minimum grain achievable is lower than a critical value, amorphisation can occur. Only samples milled in the SPEX miller became amorphous, although very low grain sizes were achieved in the Retsch (~8 nm) and Fritsch (~8 nm) millers. In directly comparable trials, the SPEX miller introduced significantly more microstructural disorder than the Retsch miller. The phase formed by milling is likely to be determined by the relative rate at which collisions introduce disorder to thermal relaxation. The low frequency of collisions in the Fritsch planetary miller (due to high

slip factors between pot and balls) in comparison to the SPEX miller is proposed as the reason for the Fritsch's ineffectiveness. The difference between the SPEX and Retsch shaker millers is assumed to be due to the SPEX's more chaotic figure-of-eight motion in comparison to the simpler linear motion of the Retsch. Cooling using liquid nitrogen was used in conjunction with the SPEX miller with the intention of increasing microstructural change by minimising thermal relaxation. The SPEX miller introduced enough disorder to allow amorphisation to occur whether-or-not cooling was used, and so no substantial differences were seen. It is suggested that cooling should be tried in cases when microstructural evolution is insufficient at ambient temperatures. Regularly scraping the sides of the pot produces a noticeable improvement in the average level of microstructural disorder introduced, and it is probably due to improved sample homogeneity. The smallest Fritsch grain size was gained in the initial stages of milling in niobium milling media, when the milling balls were relatively smooth. Smooth, distinct milling surfaces therefore appear to significant increase energy transfer to the powder during collisions, as well as improving yield. The impact of different milling media was difficult to separate into the relative effects of milling ball density and milling surface. As Ball to Powder weight Ratio (BPR) has been found to be a good way of parametrising the effect of milling in previous work, comparisons were made between tungsten carbide and steel media with the same BPR in the SPEX and Retsch millers. Tungsten carbide produced a slightly more disordered microstructure, but the difference was small in comparison with the effect of miller and regular scraping. An important comparison has been made between the contamination introduced and the microstructure induced, showing that the Fritsch miller introduces a large amount of contamination relative to the disorder it produces, even when using a hard milling media such as agate. In contrast, the SPEX and Retsch millers offer substantial improvements. The Retsch introduces contamination at the lowest rate for the disorder introduced, but in initial trials, it does

not appear to be able to achieve the sea-change in microstructure induced by the SPEX miller. In summary, milling in the SPEX miller with regular scraping and possible cooling is likely to produce the best microstructure. This is largely independent of the milling medium used, but smooth and distinct milling surfaces may aid energy transfer.

8.3 HIP'ed samples

Chapter 6 outlined the techniques used to produce a series of high-purity bulk nanocrystalline Nb_3Sn samples. Procedures and materials have been chosen to ensure sample purity at every stage. In summary, of the milled Nb_3Sn produced during this work, the powder chosen for consolidation was pre-alloyed Nb_3Sn powder (99.9 wt. % metals basis) milled using unique niobium (99.95 wt. %) milling tools under a dual argon (99.998 %) environment. The correct Nb_3Sn stoichiometry (for optimum superconductivity) was ensured by adding fine tin powder (99.8 wt. % metals basis), following determination of the Nb:Sn ratio using ICP-MS analysis. The ICP-MS work is new to the group, and standardisation experiments have been carried out which allow us to estimate the accuracy of determining the Nb:Sn mass ratio in this way to be ±2 %. The resulting powder was homogenised prior to being contained in a protective niobium foil packet (99.8 wt. % metals basis) and sealed in an evacuated stainless steel billet. Hot Isostatic Pressing (HIP'ing); at a pressure of 2000 Bar and temperatures of 450, 550, 600, 650, 700, 750 and 850 °C (likely accuracy ±10 °C); was then used to create a series of bulk samples. HIP temperatures were chosen on the basis of a temperature-dependent XRD measurement, as well as on values for Nb_3Sn formation in the literature. A novel procedure has been developed to ensure that the milled powder was not exposed to air until after consolidation to form a bulk sample. The importance of this has been highlighted by the pyrophoricity of some milled samples produced. X-Ray Diffraction

spectra show a systematic relaxation of microstructural disorder with HIP temperature, and spectra do not contain any peaks corresponding to the formation of contaminant phases. XRD data showing little change in the level of disorder at 450 °C and almost complete relaxation back to a level comparable with unmilled powder at 850 °C mean that the temperature range chosen was successful. As was seen with the temperature-dependent XRD data taken, 600 °C is a temperature at which significant microstructural change occurs.

At each HIP temperature, having 5-6 g of bulk sample has allowed a number of measurements to be taken. Variable temperature a.c. susceptibility measurements made using a Quantum Design PPMS of these disordered high-purity bulk Nb_3Sn samples at a range of applied fields (0 – 9 T) have been presented. Unmilled Nb_3Sn powder HIP'ed at 650 °C, and a commercial ternary Nb_3Sn wire from American Superconductor, have been measured along-side as standards. The critical properties of these standards are found to be in good agreement with literature values. The commercial wire has a $B_{C2}^{\chi'=0}(0)$ value of 27.6 ± 0.3 T and a $T_c^{\chi'=0}$ of 17.6 K, and the unmilled powder HIP'ed at 650 °C has a $B_{C2}^{\chi'=0}(0)$ value of 26.2 ± 0.9 T and a $T_c^{\chi'=0}$ of 18.0 K. The superconducting transitions of the fabricated samples are smooth and sharp, indicating a high degree of homogeneity and good connectivity. These data show a systematic increase of T_c with HIP temperature, from ~7 K (HIP'ed at 450 °C) up to 17.9 K (HIP'ed at 850 °C), which is the value of the as-supplied (unmilled) Nb_3Sn powder. This systematic increase coincides with the systematic decrease in disorder with HIP temperature seen in XRD data. It appears that the effect of milling is a reversible introduction of disorder only. Resistivity measurements (J Y Xiang) of the milled samples HIP'ed at 650, 700 and 750 °C show fabricated samples have extremely high ρ_N values: 294 ± 28 μΩ cm (650 °C), 200 ± 27 μΩ cm (700 °C) and 159 ± 14 μΩ cm (750 °C). The care taken in fabrication, the reduction in ρ_N with HIP temperature and the restoration of T_c at high HIP

temperature leads to the conclusion that the high resistivity values are due to the microstructural disorder present in the system and not to doping. $B_{C2}(T)$ data have been determined from a.c. magnetic measurements (onset and 0.5χ' criteria) and the resistivity data. The gradients of the $B_{C2}(T)$ data from 0 - 9 T for milled powder consolidated at 600 °C, 650 °C, 700 °C and 750 °C are steeper than those of the commercial wire and HIP'ed unmilled powder. Maki-De Gennes fits show that this increase in gradient translates into a $B_{C2}^{\chi'=0}(0)$ value of 29.5 ± 0.5 T for the best sample (HIP'ed at 700 °C), a substantial increase over ternary commercial wire (27.6 ± 0.3 T) and HIP'ed unmilled powder (26.2 ± 0.9 T). The improvement is larger for the 0.5χ' criterion: 29.1 ± 0.2 T for in comparison to 24.6 ± 0.3 T for the ternary wire. The difference between criteria is due to fabricated samples having better sample homogeneity than the commercial samples. Resistivity measurements (using 0.5ρ_N criterion) of the best three samples confirm unusually high $B_{C2}(0)$ values, up to 31.7 ± 0.4 T for 700 °C sample: ~6 T higher than typical values in the literature. Although the mechanism for the improvement is not fully understood, it seems certain that as seen in previously in nanocrystalline $PbMo_6S_8$, it is related to the huge increase in resistivity introduced by microstructural disorder (Scherrer grain size 67 nm). The upper critical field value is a very high value for bulk binary Nb_3Sn, and demonstrates that this technologically important quantity has not yet been optimised in commercial wires.

Chapter 9

Future work

In this work, a method for electroplating titanium has been developed, parameters affecting the introduction of disorder into the superconductor Nb_3Sn by ball milling have been investigated, and data showing an increased upper critical field in fabricated nanocrystalline Nb_3Sn have been presented. In this chapter, future directions of this work will be suggested.

The need to characterise the effects of strain, field and temperature on the engineering critical current densities of ITER-candidate wires will ensure that the group's work using the Walters-spring technique will continue. Although the spring design may be tweaked, the material used for the spring is unlikely to change, and so the work in this thesis on developing a method of electroplating titanium will remain relevant. Significant amendments to the process set-up should not be necessary.

The wide-ranging work on ball milling in this thesis has already informed future choice of milling parameters, most significantly through the purchase of a SPEX 8000D miller following a successful trial. The literature on ball milling is of limited use, in part due to the number of parameters which determine the outcome, but also because there is no well-developed theory which reliably predicts milling products. In short, there is often no substitute for a trial-and-error approach, and in this respect the work in this thesis will be valuable in informing future work in the group. The trends in the effect of milling parameters noted are a useful basis for choosing milling conditions. The purchase of a SPEX 8000D miller, which has been shown to be able to reduce grain size below that of

the Fritsch miller, should allow the introduction of more disorder in a shorter time with less contamination. In the short-term, impurities will continue to be measured using the ICP-MS technique introduced to the group in this work. Attempts were made to use Proton Induced X-ray Emission (PIXE) as a non-destructive alternative to ICP-MS for determining atomic ratios, and this may be worth pursuing. Although all possible care has been taken to avoid oxygen contamination, the accurate determination of oxygen and nitrogen levels in milled samples would make changes due to microstructure clear and unambiguous. Gas-fusion would provide this facility, and is available on an inexpensive commercial basis. It would be worthwhile gaining a working knowledge of Rietveld refinement for the XRD spectra, as this would yield more detailed information about the microstructure with relatively little effort. The microstructure produced by milling, and which aspects of disorder introduced are essential for increasing upper critical field remain unclear. Heat capacity measurements, available in-house, would provide more information about the Nb_3Sn samples produced. In terms of more detailed information, collaboration with a group with TEM expertise may be an option, but how representative thin sample sections would be of the bulk could be a concern.

There is no suggestion that the significant improvement in $B_{C2}(0)$ produced in this work represents any kind of fundamental limit, nor that the procedure used is by any means the optimum. Larger increases should be achievable using the SPEX miller, particularly given that high yields are possible in soft milling media by a combination of regular scraping and the SPEX's milling action. Milling in niobium followed by consolidating the powder in the rigorous way outlined should lead to samples with smaller grain size, whilst retaining exceptional purity. The increases in $B_{C2}(0)$ in samples fabricated in this work, and by Cooley et al., are potentially significant for the use of Nb_3Sn in high-field magnet applications. The Powder-In-Tube (PIT) techniques currently used for wire production would need modification to incorporate pre-alloyed Nb_3Sn, but

proving that upper critical field can be boosted by increasing resistivity should spawn work by manufacturers into different methods of achieving this. It may also encourage similar work on high temperature superconductors which, in the long-run, are expected to replace low-temperature magnets. The Durham University Superconductivity Group is likely to be involved in this, due to the facilities and expertise here. The market for superconducting magnets is huge, particularly with the ITER fusion reactor seemingly back-on-track. Increasing the upper critical field of superconducting wires allows the production of more compact, more powerful and wider-bore magnets for applications such as in motors for transport applications, ITER and MRI scanners. In addition, the theoretical aspects of the scale of increases possible are still not fully understood. Nanocrystalline superconductors should therefore remain of interest for both academia and industry.

References

[1] H. K. Onnes, Communications from the Physical Laboratory of the University of Leiden **124C**, 21 (1911).

[2] J. G. Bednorz and K. A. Müller, Z. Phys. B **64**, 189 (1986).

[3] H. J. Niu and D. P. Hampshire, Phys. Rev. Lett. **91**, 027002 (2003).

[4] J. S. Benjamin, Met. Trans. **1**, 2943 (1970).

[5] V. L. Ginzburg and L. D. Landau, Zh. Eksp. Teor. Fiz. **20**, 1064 (1950).

[6] C. P. Poole, H. A. Farach, and R. J. Creswick, *Superconductivity* (Academic Press Inc, San Diego, California, 1995).

[7] D. M. J. Taylor, Durham University internal report, 2001.

[8] D. R. Tilley and J. Tilley, *Superfluidity and Superconductivity* (IOP publishing Ltd., Bristol, 1990).

[9] M. Tinkham, *Introduction to Superconductivity* (McGraw-Hill Book Co., Singapore, 1996).

[10] G. Carty, Durham University internal report, 2001.

[11] I. J. Daniel, Ph.D. thesis, Durham University, 1999.

[12] J. B. Ketterson and S. N. Song, *Superconductivity* (Cambridge University Press, 1999).

[13] J. F. Annett, *Superconductivity, Superfluids and Condensates* (OUP, 2003).

[14] P. G. De Gennes, *Superconductivity in Metals and Alloys* (Addison Wesley Publishing Company, Redwood City, California, 1989).

[15] H. F. Hess, R. B. Robinson, R. C. Dynes, J. M. Valles Jr, and J. V. Waszczak, Phys. Rev. Lett. **62**, 214 (1989).

[16] A. A. Abrikosov, Sov. Phys. JETP **5**, 1174 (1957).

[17] W. H. Kleiner, L. M. Roth, and S. H. Autler, Phys. Rev. **133**, A1226 (1964).

[18] C. P. Bean, Rev. Mod. Phys. **36**, 31 (1964).

[19] N. A. Morley, Thesis: Durham University (2003).

[20] T. P. Orlando, E. J. McNiff, S. Foner, and M. R. Beasley, Phys. Rev. B **19**, 4545 (1979).

[21] T. Orlando, J. Alexander, S. Bending, J. Kwo, S. Poon, R. Hammond, M. Beasley, J. McNiff, EJ, and S.]Foner, IEEE Trans. Magn. **17**, 368 (1981).

[22] N. R. Werthamer, E. Helfand, and P. C. Hohenberg, Phys. Rev. **147**, 295 (1966).

[23] B. S. Murty and S. Ranganathan, Int. Mater. Rev. **43**, 101 (1998).

[24] C. Suryanarayana, Prog. Mater. Sci. **46**, 1 (2001).

[25] R. B. Schwarz, Script. Mat. **34**, 1 (1996).

[26] M. A. Menary, M. Sci. thesis, Durham, 2005.

[27] Y. S. Cho and C. C. Koch, Mat Sci and Eng **A141**, 139 (1991).

[28] M. S. Kim and C. C. Koch, J. Appl. Phys. **62**, 3450 (1987).

[29] S. N. Patankar and F. H. Froes, Solid State Sciences **6**, 887 (2004).

[30] P. Scherrer, Nachr. Ges. Wiss. Gottingen **2**, 98 (1918).

[31] G. K. Williamson and W. H. Hall, Acta Metall. **1**, 22 (1953).

[32] H. M. Rietveld, Journal of Applied Crystallography **2**, 65 (1969).

[33] A. L. Ortiz and L. Shaw, Acta Mater. **52**, 2185 (2004).

[34] P. Scardi, M. Leoni, and R. Delhez, Journal of Applied Crystallography **37**, 381 (2004).

[35] A. Guinier, *Radiocristallographie. English* (W. H. Freeman, San Francisco; London, 1963).

[36] R. Flukiger, in *Handbook of Superconducting Materials*, edited by D. Cardwell and D. Ginley (IOP Publishing, Bristol, 2003), Vol. 1, p. 391.

[37] F. Folkmann, C. Gaarde, T. Huus, and K. Kemp, **116**, 487 (1974).

[38] D. M. J. Taylor and D. P. Hampshire, Supercond. Sci. Tech. **18**, 356 (2005).

[39] R. Aymar, Fusion Eng. Des. **55**, 107 (2001).

[40] D. M. J. Taylor and D. P. Hampshire, Supercond. Sci. Tech. **18**, 297 (2005).

[41] C. R. Walters, I. M. Davidson, and G. E. Tuck, Cryogenics **26**, 406 (1986).

[42] W. Turner, Patent No. 4,416,739 (22 November 1983).

[43] C. C. f. O. H. a. S. CCOHS, http://www.intox.org/databank/documents/chemical/hyfluric/cie47.htm,

[44] L. Muriale, E. Lee, J. Genovese, and S. Trend, Ann. Occup. Hyg. **40**, 705 (1996).

[45] D. M. J. Taylor and D. P. Hampshire, University of Durham Report No. EFDA-03-1126, 2005.

[46] W. Martienssen and H. Warlimont, (Springer Berlin Heidelberg, Berlin, 2005), p. 1120.

[47] I. H. C. ASM, 1990, Vol. 2.

[48] R. C. Weast, M. J. Astle, and W. H. Beyet, *Handbook of Chemistry and Physics* (CRC Press, Boca Raton, FL, 1989).

[49] I. H. C. ASM, 1990), Vol. 1.

[50] M. N. Wilson, *Superconducing Magnets* (Oxford University Press, 1986).

[51] H. Devantay, J. L. Jorda, M. Decroux, J. Muller, and R. Flukiger, J. Mater. Sci. **16**, 2145 (1981).

[52] D. Cardwell, in *Chevrel phase superconductors*, edited by D. P. Hampshire (IOP Publishing, Bristol, 2002).

[53] C. Suryanarayana, E. Ivanov, R. Noufi, M. A. Contreras, and J. J. Moore, J. Mater. Res. **14**, 377 (1998).

[54] B. L. Chu, C. C. Chen, and T. P. Perng, Metallurgical Transactions A - Physical Metallurgy and Materials Science **23**, 2105 (1992).

[55] J. Larson, T. Luhman, and H. Merrick, in *Manufacture of superconducting materials*, edited by R. W. Meyerhoff (American Society for Metals, Port Chester, New York, 1976), p. 155.

[56] P. Bhattacharya, P. Bellon, R. S. Averback, and S. J. Hales, J. Alloy. Compd. **368**, 187 (2004).

[57] M. C. Denis, P. Gouerec, D. Guay, J. P. Dodelet, G. Lalande, and R. Schulz, Journal of Applied Electrochemistry **30**, 1243 (2000).

[58] L. Lu, M. O. Lai, and S. Zhang, J. Mater. Process. Technol. **48**, 683 (1995).

[59] P. G. McCormick, H. Huang, M. P. Dallmore, J. Ding, and J. Pan, in *Mechanical Alloying for Structural Applications*, 1993), p. 45.

[60] Fritsch, 2005.

[61] N. Burgio, A. Iasonna, M. Magini, S. Martelli, and F. Padella, Nuovo Cimento Soc. Ital. Fis. D-Condens. Matter At. Mol. Chem. Phys. Fluids Plasmas Biophys. **13**, 459 (1991).

[62] H. Mio, J. Kano, F. Saito, and K. Kaneko, Mater. Sci. Eng. A-Struct. Mater. Prop. Microstruct. Process. **332**, 75 (2002).

[63] T. H. Courtney and D. Maurice, Script. Mat. **34**, 5 (1996).

[64] C. C. Koch, chapter, 1991, p. 193.

[65] T. S. Ward, W. L. Chen, M. Schoenitz, R. N. Dave, and E. L. Dreizin, Acta Mater. **53**, 2909 (2005).

[66] D. Gavrilov, O. Vinogradov, and W. J. D. Shaw, in *Proceedings of the Tenth International Conference on Composite Materials*, edited by A. Poursartip and K. Street (Cambridge, England : Woodhead Pub. Ltd., Whistler, British Columbia, Canada, 1995), Vol. 3, p. p11.

[67] L. Takacs and M. Pardavihorvath, J. Appl. Phys. **75**, 5864 (1994).

[68] R. J. Perez, H. G. Jiang, C. P. Dogan, and E. J. Lavernia, Metall. Mater. Trans. A **29**, 2469 (1998).

[69] C. C. Koch, O. B. Cavin, C. G. McKamey, and J. O. Scarbrough, Appl. Phys. Lett. **43**, 1017 (1983).

[70] R. L. White, Ph.D. thesis, Stanford University, 1980.

[71] M. Karppinen, A. Fukuoka, L. Niinisto, and H. Yamauchi, Superconductor Science & Technology **9**, 121 (1996).

[72] Eltra GmbH, 2006.

[73] Leco Corporation, 2006.

[74] W. A. Kaczmarek and B. W. Ninham, Mater. Chem. Phys. **40**, 21 (1995).

[75] Y. F. Zhang, L. Lu, and S. M. Yap, J. Mater. Process. Technol. **90**, 260 (1999).

[76] S. F. Lomayeva, E. P. Yelsukov, G. N. Konygin, G. A. Dorofeev, V. I. Povstugar, S. S. Mikhailova, A. V. Zagainov, and A. N. Maratkanova, Colloid Surf. A-Physicochem. Eng. Asp. **162**, 279 (2000).

[77] Z. Caamano, G. Perez, L. E. Zamora, S. Surinach, J. S. Munoz, and M. D. Baro, J. Non-Cryst. Solids **287**, 15 (2001).

[78] J. S. Byun, J. H. Shim, and Y. W. Cho, J. Alloy. Compd. **365**, 149 (2004).

[79] J. Keskinen, A. Pogany, J. Rubin, and P. Ruuskanen, Mater. Sci. Eng. A-Struct. Mater. Prop. Microstruct. Process. **196**, 205 (1995).

[80] C. C. Koch, Nanostruct. Mater. **2**, 109 (1993).

[81] H. J. Niu and D. P. Hampshire, Physica C **372**, 1145 (2002).

[82] G. X. Liu and Z. M. Guan, Defect and Diffusion Forum **150**, 95 (1997).

[83] L. M. Di, P. I. Loeff, and H. Bakker, Journal of the Less-Common Metals **168**, 183 (1991).

[84] H. Bakker, G. F. Zhou, and H. Yang, Prog. Mater. Sci. **39**, 159 (1995).

[85] A. van Winkel, A. W. Weeber, and H. Bakker, J. Phys. F - Met. Phys. **14**, 2631 (1984).

[86] T. Miyazaki, T. Hase, and T. Miyatake, in *Handbook of Superconducting Materials*, edited by D. Cardwell and D. Ginley (IOP Publishing, Bristol, 2003), Vol. 2, p. 639.

[87] P. Bellon and G. Martin, Phys. Rev. B **39**, 2403 (1989).

[88] Y. S. Cho and C. C. Koch, J. Alloy. Compd. **194**, 287 (1993).

[89] J. Joardar, S. K. Pabi, and B. S. Murti, Script. Mat. **50**, 1199 (2004).

[90] M. Oehring and R. Bormann, Mater. Sci. Eng. A-Struct. Mater. Prop. Microstruct. Process. **51**, C4169 (1990).

[91] L. M. Di and H. Bakker, J. Appl. Phys. **71**, 5650 (1992).

[92] C. C. Koch, Script. Mat. **34**, 21 (1996).

[93] X. K. Zhu, X. Zhang, H. Wang, A. V. Sergueeva, A. K. Mukherjee, R. O. Scattergood, J. Narayan, and C. C. Koch, Script. Mat. **49**, 429 (2003).

[94] X. Zhang, H. Wang, R. O. Scattergood, J. Narayan, and C. C. Koch, Acta Mater. **50**, 3995 (2002).

[95] D. C. Larbalestier, Cryogenics **35**, S15 (1995).

[96] J. L. H. Lindenhovius, E. M. Hornsveld, A. den Ouden, W. A. J. Wessel, and H. H. J. ten Kate, IEEE Trans. Appl. Supercond. **10**, 975 (2000).

[97] C. D. Hawes, P. J. Lee, and D. C. Larbalestier, IEEE Trans. Appl. Supercond. **10**, 988 (2000).

[98] F. Ye and K. Lu, Phys. Rev. B **60**, 7018 (1999).

[99] A. Godeke, M. C. Jewell, C. M. Fischer, A. A. Squitieri, P. J. Lee, and D. C. Larbalestier, J. Appl. Phys. **97**, 093909 (2005).

[100] J. Evetts, in *Advances in Materials Science and Engineering* (Pergamon, 1992).

[101] L. R. Testardi and L. F. Mattheiss, Phys. Rev. Lett. **41**, 1612 (1978).

[102] A. Godeke, M. C. Jewell, A. A. Golubov, B. Ten Haken, and D. C. Larbalestier, Supercond. Sci. Tech. **16**, 1019 (2003).

[103] A. Godeke, Ph.D. thesis, University of Twente, 2005.

[104] M. C. Jewell, A. Godeke, P. J. Lee, and D. C. Larbalestier, in *Advances in Cryogenic Engineering, Vols 50a and B*, 2004), Vol. 711, p. 474.

[105] L. Cooley, Y. F. Hu, and A. R. Moodenbaugh, preprint (2006)